2017

Polarization Observables T and F in the yp -> pi p Reaction

Hao Jiang
University of South Carolina

Polarization Observables T and F in the $\gamma p \to \pi^0 p$ Reaction

by

Hao Jiang

Bachelor of Science
Shanghai Jiaotong University 2010

Submitted in Partial Fulfillment of the Requirements

for the Degree of Doctor of Philosophy in

Physics

College of Arts and Sciences

University of South Carolina

2017

Accepted by:

Steffen Strauch, Major Professor

Chaden Djalali, Committee Member

Ralf Gothe, Committee Member

Matthias Schindler, Committee Member

Cheryl L. Addy, Vice Provost and Dean of the Graduate School

Acknowledgments

This analysis has been done with the support from many people. I would like first to thank my advisor Professor Steffen Strauch for the instruction and help in these years. I also appreciate the support from Professor Chaden Djalali, Professor Ralf Gothe, Professor Matthias Schindler in my doctoral committee and other people in the Department of Physics and Astronomy at University of South Carolina. I would also like to thank Dr. M. Dugger, Dr. N. Walford and others in the FROST group at Jefferson Lab for their useful work. The funding support from the National Science Foundation and other funding agencies are also appreciated. This work is supported in parts by NSF PHY-1505615.

Abstract

The theory that describes the interaction of quarks is Quantum Chromodynamics (QCD), but how quarks are bound inside a nucleon is not yet well understood. Pion photoproduction experiments reveal important information about the nucleon excited states and the dynamics of the quarks within it and thus provide a useful tool to study QCD. Detailed information about this reaction can be obtained in experiments that utilize polarized photon beams and polarized targets.

Pion photoproduction in the $\gamma p \to \pi^0 p$ reaction has been measured in the FROST experiment at the Thomas Jefferson National Accelerator Facility. In this experiment circularly polarized photons with electron-beam energies up to 3.082 GeV impinged on a transversely polarized frozen-spin target. Final-state protons were detected in the CEBAF Large Acceptance Spectrometer. Results of the polarization observables T and F have been extracted. The data generally agree with predictions of present partial wave analyses, but also show marked differences. The data will constrain further partial wave analyses and improve the extraction of proton resonance properties.

Table of Contents

List of Tables

List of Figures

Chapter 1

Introduction

1.1 Baryon Spectroscopy

As baryons are the major components of the real world, the interests in baryons by nuclear physicists never stop growing. Baryons are composed of three valence quarks and any number of quark-antiquark pairs and gluons. The baryon number of a baryon is one. Baryons are fermions with 3-quark (qqq) configurations for all established baryons [1]. The wave function of the three-quark system is antisymmetric under interchange of any two equal-mass quarks. It has color, space, spin, and flavor degrees of freedom. The wave function containing the color degrees of freedom is antisymmetric and separates out from the rest,

$$|qqq\rangle_A = |\text{color}\rangle_A \times |\text{space, spin, flavor}\rangle_S, \tag{1.1}$$

where the subscripts S indicates symmetry and the subscripts A indicates antisymmetry under quark interchange. All baryons can be sorted in two groups: spin-1/2 baryons and spin-3/2 baryons. For the nonstrange baryons, there are two kinds of resonances, N^* and Δ^*. In the $SU(6)\otimes O(3)$ symmetry, the group $SU(6)$ contains the intrinsic spin group $SU(2)$ and the internal symmetry group $SU(3)$, containing the light quarks flavors u, d, and s. When combined with the group of rotations in the three-dimensional space, $O(3)$, the result $SU(6)\otimes O(3)$ symmetry is used to describe the structure of strongly interacting particles [2]. In the $SU(3)$ flavor group, the spin-1/2 baryons are categorized into a octet and the spin-3/2 baryons are categorized into a decuplet. The octet and the decuplet are shown in Fig. 1.1 and Fig. 1.2.

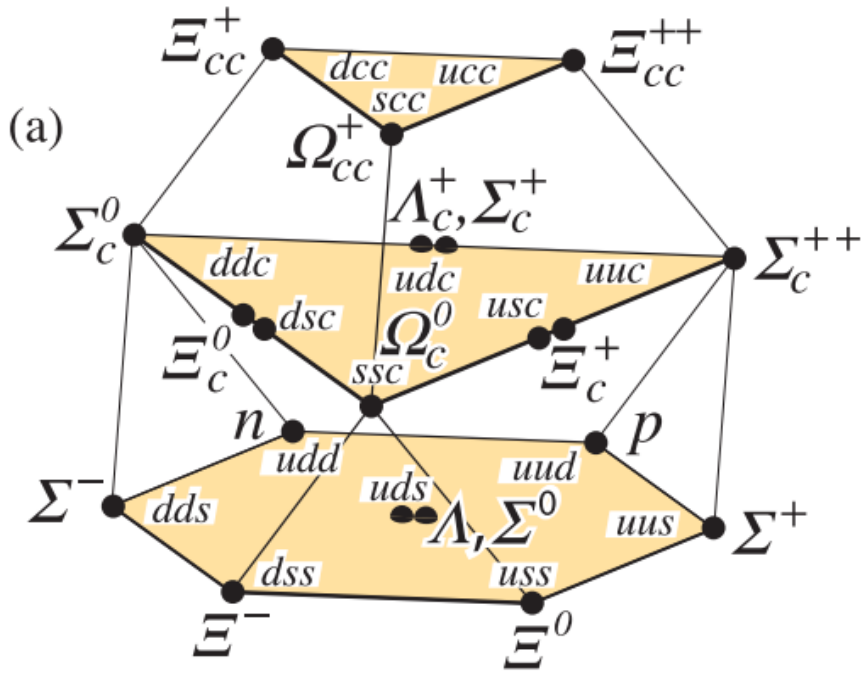

Figure 1.1 The 20-plet with an $SU(3)$ octet. This figure is from [1].

Quantum Chromodynamics (QCD) describes the strong interactions of quarks and gluons. QCD is a gauge field theory with the color $SU(3)$ symmetry. Perturbative QCD at high energies is successful. In the low-energy regime, the perturbative QCD is not successful. The non-perturbative QCD works in the low energy regime. The baryons at low energies are the major components of the real world. This makes it important to study the baryons. Additionally, the study of baryons is ideal to understand the strong interaction in the low energy regime.

The study of the excited baryon resonances reveals the strong interaction in the quark confinement and provides complementary information on the structure of the nucleon. The determination of the excited states, the identification of new symmetries, and the microscopic-level structure of states have been the objective of recent baryon-spectroscopy experiments [3]. Baryon spectroscopy is a useful tool in the study of QCD as resonances reflect the dynamics and degrees-of-freedom within hadrons.

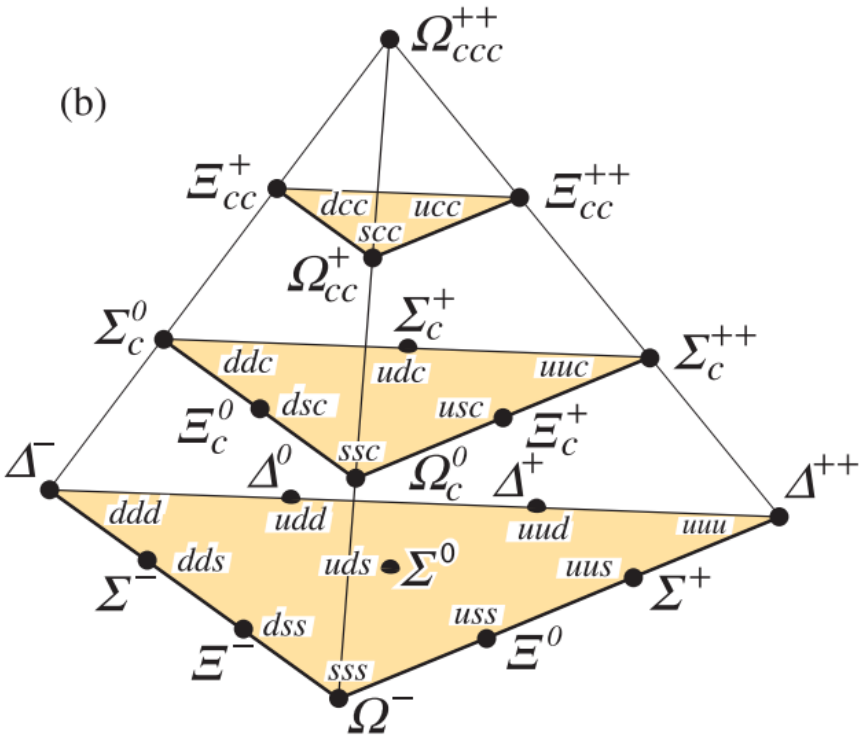

Figure 1.2 The 20-plet with an $SU(3)$ decuplet. This figure is from [1].

There are several challenges of baryon spectroscopy. Most baryon states are short-lived and have a large decay widths. This makes it difficult to identify resonances as peak in the excitation spectrum as they are broad and overlapping.

So far, by analyzing the observables from existing measurements of pion scattering, meson-electroproduction, and meson-photoproduction, a large number of baryon resonances and their properties, like mass, width, quantum numbers, and coupling constants, are known. The relation between experimental observables, baryon properties, and QCD is shown in Fig. 1.3. The connection between experimental observables and baryon resonances is the partial-wave analysis. Table 1.1 gives a list of known $N*$ and $\Delta*$ resonances, including the corresponding total angular momentums and parity in the format of J^P. However, the number of baryon resonances detected by using existing experimental data is less than that predicted by $SU(6)\otimes O(3)$ symmetry of the constituent quark model.

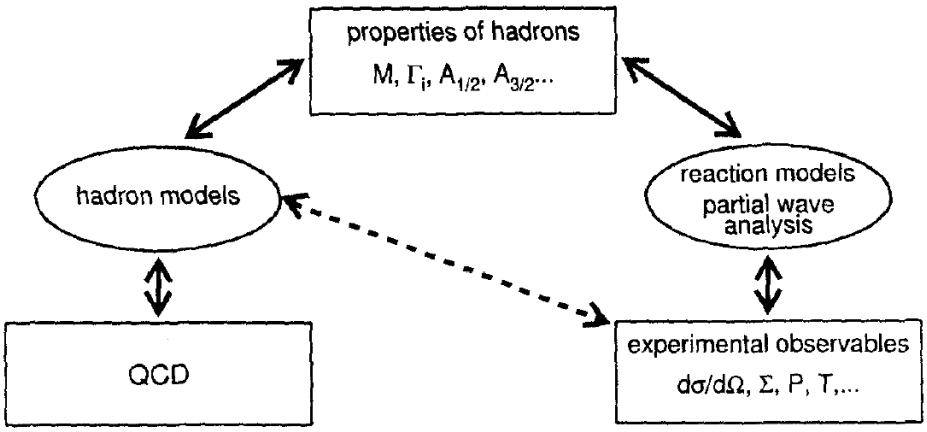

Figure 1.3 Relation between experimental observables, baryon properties, and QCD [4].

There are several quark models with different degrees-of-freedom. Three examples of degrees-of-freedom in quark models are shown in Fig. 1.4 [4]. From left to right there are: three equivalent constituent quarks, quark-diquark model structure, and quark and flux-tube. The effective degrees of freedom of baryons determine the number of excited states.

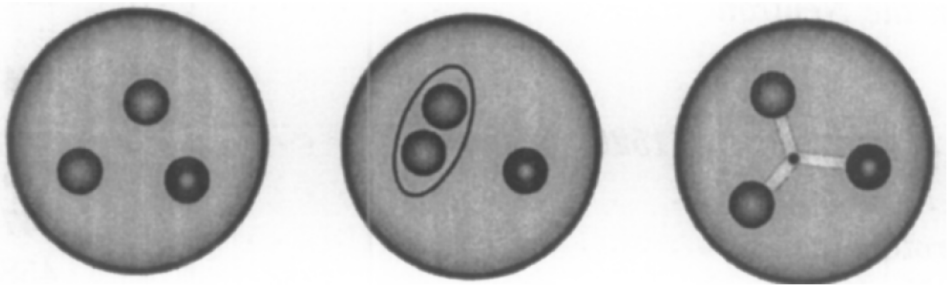

Figure 1.4 Three examples of effective degrees-of-freedom in quark models [4]. From left to right: three equivalent constituent quarks, quark-diquark structure, and quarks and flux-tubes.

Among all the quark models, the constituent quark model [5] is the most basic one. In this model, there are three equivalent constituent quarks that determine the effective degrees of freedom of the baryon. The constituent quark is a quark

Table 1.1 Baryon Table for N^* and Δ^* from PDG 2016 [1]. Four stars indicate the existence is certain, and properties are at least fairly well explored. Three stars indicate the existence ranges from very likely to certain, but further conformation is desirable and/or quantum numbers, branching fractions, etc. are not well determined. Two stars indicate the evidence of existence is only fair. One star indicates the evidence of existence is poor.

N^*	J^P	2016	Δ^*	J^P	2016
p	$1/2^+$	****	$\Delta(1232)$	$3/2^+$	****
n	$1/2^+$	****	$\Delta(1600)$	$3/2^+$	***
$N(1440)$	$1/2^+$	****	$\Delta(1620)$	$1/2^-$	****
$N(1520)$	$3/2^-$	****	$\Delta(1700)$	$3/2^-$	****
$N(1535)$	$1/2^-$	****	$\Delta(1750)$	$1/2^+$	*
$N(1650)$	$1/2^-$	****	$\Delta(1900)$	$1/2^-$	**
$N(1675)$	$5/2^-$	****	$\Delta(1905)$	$5/2^+$	****
$N(1680)$	$5/2^+$	****	$\Delta(1910)$	$1/2^+$	****
$N(1700)$	$3/2^-$	***	$\Delta(1920)$	$3/2^+$	***
$N(1710)$	$1/2^+$	****	$\Delta(1930)$	$5/2^-$	***
$N(1720)$	$3/2^+$	****	$\Delta(1940)$	$3/2^-$	**
$N(1860)$	$5/2^+$	**	$\Delta(1950)$	$7/2^+$	****
$N(1875)$	$3/2^-$	***	$\Delta(2000)$	$5/2^+$	**
$N(1880)$	$1/2^+$	**	$\Delta(2150)$	$1/2^-$	*
$N(1895)$	$1/2^-$	**	$\Delta(2200)$	$7/2^-$	*
$N(1900)$	$3/2^+$	***	$\Delta(2300)$	$9/2^+$	**
$N(1990)$	$7/2^+$	**	$\Delta(2350)$	$5/2^-$	*
$N(2000)$	$5/2^+$	**	$\Delta(2390)$	$7/2^+$	*
$N(2040)$	$3/2^+$	*	$\Delta(2400)$	$9/2^-$	**
$N(2060)$	$5/2^-$	**	$\Delta(2420)$	$11/2^+$	****
$N(2100)$	$1/2^+$	*	$\Delta(2750)$	$13/2^-$	**
$N(2120)$	$3/2^-$	**	$\Delta(2950)$	$15/2^+$	**
$N(2190)$	$7/2^-$	****			
$N(2220)$	$9/2^+$	****			
$N(2250)$	$9/2^-$	****			
$N(2300)$	$9/2^+$	**			
$N(2570)$	$9/2^-$	**			
$N(2600)$	$11/2^-$	***			
$N(2700)$	$13/2^+$	**			

surrounded by quarks and gluons. The effective quark masses in a nucleon are the constituent quark masses. The constituent quarks in the constituent quark model by Isgur and Karl are confined by a harmonic oscillator potential [6]. In the early years,

this model was proven to be successful as the discovered resonances were correctly described by using this model, but the number of states predicted by this model is more than the number observed in experiments.

Some variants were proposed afterwards and derived from three equivalent quarks in a collective potential. For example, the flux tube model [7] was extracted from the strong-coupling Hamiltonian lattice formulation of QCD. The interaction among quarks was a short range residual interaction instead. In this model, the flux tubes are considered as degrees of freedom besides the quark degrees of freedom. Because of the additional degrees of freedom, this model predicts even more states [8].

Later, models based on other degrees-of-freedom were proposed. An example is the quark-diquark model [9]. In this model, the diquark is bound strongly and suppresses its excitations in the low lying excitations of the nucleon because an attractive hyperfine interaction between a u and d-quark in the isospin-zero channel [8]. Fewer states are predicted in this model as there are fewer degrees of freedom at low energies, but the number of states predicted by this model is still more than the number observed in experiments. Missing resonances are expected in symmetric but not in diquark models.

Recently, another approach rather than quark models is developing. Lattice QCD (LQCD), which describes the four-dimensional space as lattice of points as regularization. The hardon spectrum is one of the most basic predictions of LQCD. After 30 years of development of LQCD, the algorithms and analysis techniques for light quarks became feasible but it was still a challenging task to reach the same level of precision for excited states [10]. An example are the computational results [11] which observed the first excited states of the N^* resonance from LQCD are similar to the results from quark models. Recent comparisons of results from LQCD and experiment are shown in Fig. 1.5. The excited states have also been calculated by LQCD as shown in Fig. 1.6.

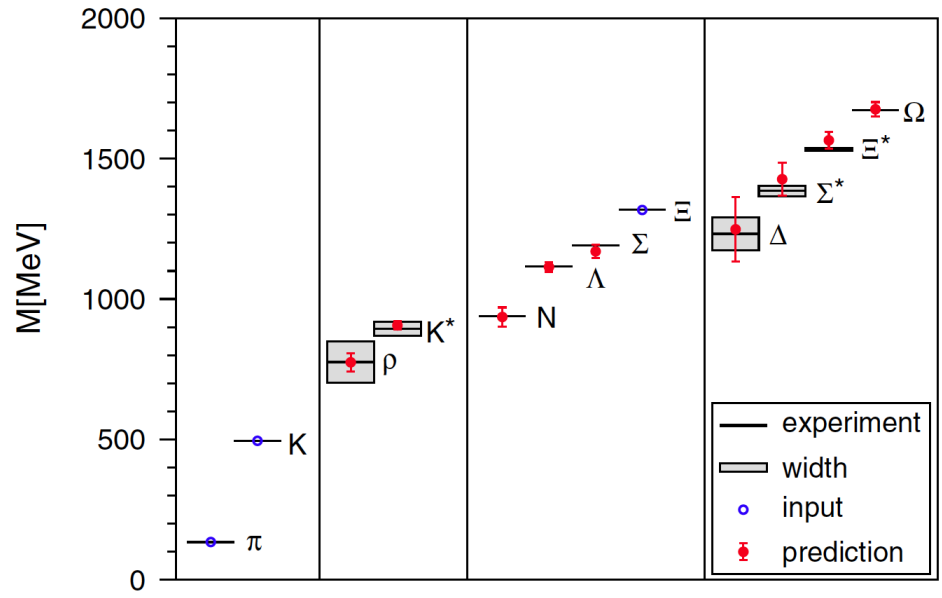

Figure 1.5 Comparisons of results from LQCD and experiment. The figure is from [12].

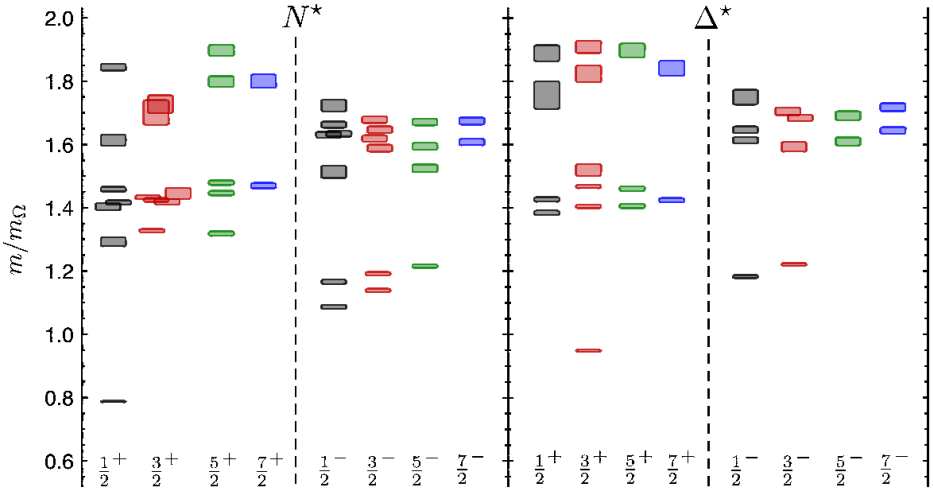

Figure 1.6 Spin-identified spectrum of Nucleons and Deltas. The figure is from [13].

Although the list of known resonances, Table 1.1, has been updated by the PDG group frequently, there are still many resonances missing from the $SU(6)\otimes O(3)$ predictions of the constituent quark model, especially in the mass range higher than 1.7 GeV. This phenomenon is known as the 'missing' resonance problem. A summary of

predicted and discovered N resonances is displayed in Fig. 1.7.

The 'missing' resonance problem originates from the difference between the number of states predicted by the quark model and the number observed. Resonances may not have been observed due to a weak coupling of the missing states to the reaction channel of the experiment or may not exist because the degrees of freedom used in the quark model is incorrect. For example, fewer states are predicted in the quark-diquark model as there are fewer degrees of freedom at low energies, but the number of states predicted by this model is still more than the number observed in experiments although less than the number of states predicted by the constituent quark model. This means more studies are needed to determine the degrees of freedom in quark models. A more completed knowledge of resonances will improve our understanding of the underlying symmetries and quark-quark interactions as resonances reflect the dynamics and relevant degrees-of-freedom within hadrons.

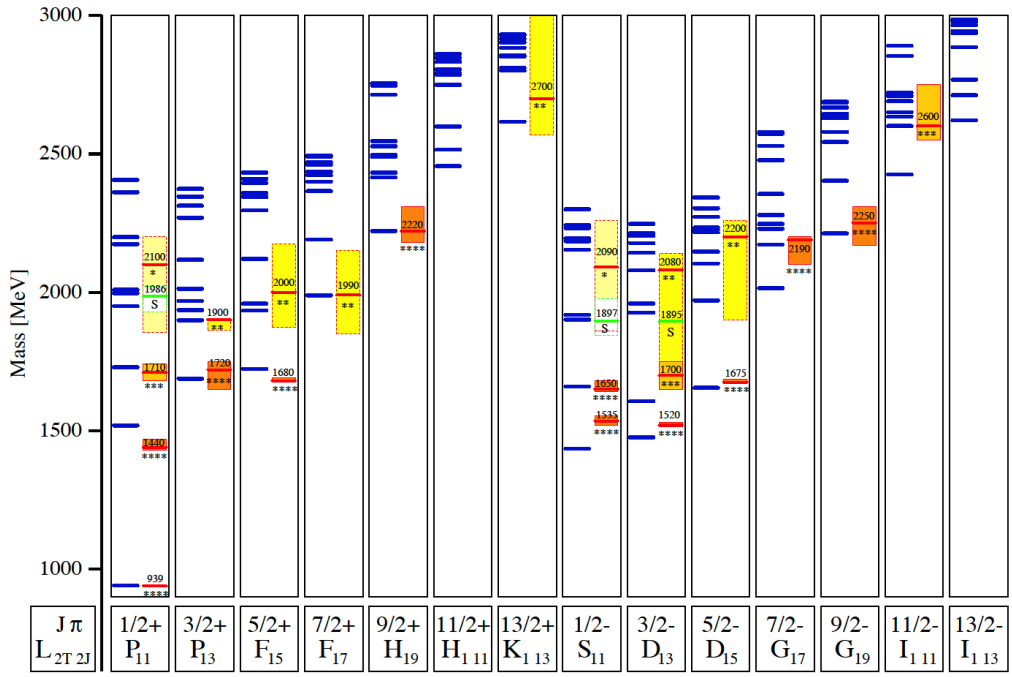

Figure 1.7 The predicted N resonances and the spectrum discovered in experiments. The blue lines are for the predicted N resonances and the experimental spectrum is on the right side. This figure is from [14].

1.2 Single-Pion Photoproduction

There are several ways to probe the baryon excited states. To improve the interpretation of the resonance spectrum confused by the missing resonances, the single-pion photoproduction has its advantage; e.g. supporting evidence for a previously poorly known $\Delta(2200)7/2^-$ state was found in an analysis [15] that included results of a recent measurement of the polarized $\gamma p \to \pi^+ n$ reaction [16]. In addition to the mass and width values provided by the elastic pion-nucleon scattering, the single-pion photoproduction process provides confirmations to the baryon excited states and determines the amplitudes. The information about baryon resonances can be obtained from the complex amplitudes of the single-pion photoproduction process, which can be extracted from the observables. The measurement of double-polarization observables with a polarized target are needed in addition of the unpolarized cross section and single-polarization observables, as they carry additional information about the complex amplitudes which does not exist in the unpolarized cross section and single-polarization observables. The diagram of this reaction is shown in Fig. 1.8.

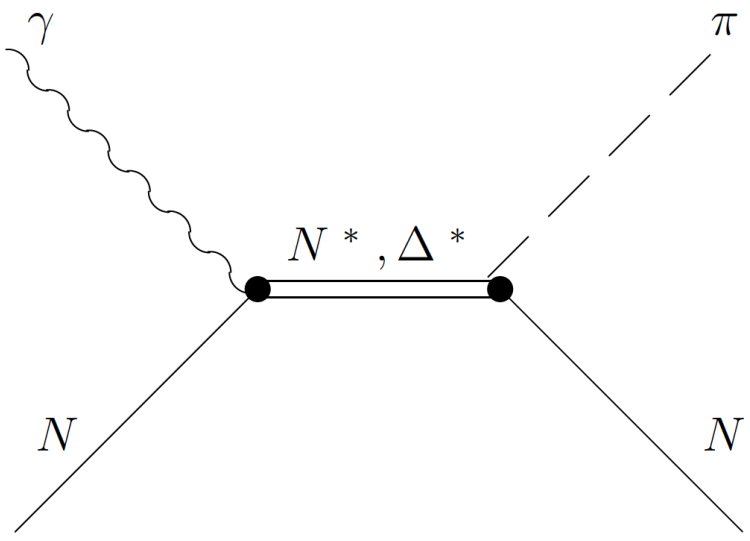

Figure 1.8 The s-channel diagram of the single-pion photoproduction process with baryon excited states as the intermediate product. This figure is from [17].

It can be described in terms of four complex amplitudes since the product of the number of spin states for each particle halfed by the parity conservation is four. In the s-channel helicity representation, they are the no-flip, N, single-flip, S_1 and S_2, as well as double-flip, D, amplitudes [18]. The unpolarized differential cross section,

$$\frac{d\sigma_0}{d\Omega} = |N|^2 + |S_1|^2 + |S_2|^2 + |D|^2, \tag{1.2}$$

cannot reveal the full information of the complex amplitudes.

Additional information, including phase relations, can be provided by polarization observables. For example, in the helicity representation, the polarization observables T and F are defined as

$$T\frac{d\sigma_0}{d\Omega} = 2\mathrm{I}m(S_1N^* - S_2D^*), \tag{1.3}$$

and

$$F\frac{d\sigma_0}{d\Omega} = 2\mathrm{R}e(S_2D^* + S_1N^*). \tag{1.4}$$

As polarization observables are sensitive to small amplitudes and phase differences, they provide important constraints to reveal the dynamics and relevant degrees-of-freedom within hadrons. In addition to the single-polarization observables (S), the double-polarization observables are categorized into three types: beam-target (BT), target-recoil (TR), and beam-recoil (BR) asymmetries. Since the recoil polarization is difficult to measure for the pion-proton finalstate, the most common observables in experiments are the single-polarization observables and the beam-target double-polarization observables. A complete list of all pseudoscalar photoproduction observables is shown in Table 1.2.

1.3 Formalism

For the single-pion photoproduction reaction, with a polarized photon beam and a polarized target, the available observables are listed in Table 1.3 and the polarized

Table 1.2 A complete list of all pseudoscalar photoproduction observables [18]

Symbol	Helicity Representation	Type
$\frac{d\sigma_0}{d\Omega}$	$\|N\|^2+\|S_1\|^2+\|S_2\|^2+\|D\|^2$	S
$\Sigma\frac{d\sigma_0}{d\Omega}$	$2\mathrm{R}e(S_1^*S_2-ND^*)$	S
$T\frac{d\sigma_0}{d\Omega}$	$2\mathrm{I}m(S_1N^*-S_2D^*)$	S
$P\frac{d\sigma_0}{d\Omega}$	$2\mathrm{I}m(S_2N^*-S_1D^*)$	S
$G\frac{d\sigma_0}{d\Omega}$	$-2\mathrm{I}m(S_1S_2^*+ND^*)$	BT
$H\frac{d\sigma_0}{d\Omega}$	$-2\mathrm{I}m(S_1D^*-S_2N^*)$	BT
$E\frac{d\sigma_0}{d\Omega}$	$\|N\|^2-\|S_1\|^2+\|S_2\|^2-\|D\|^2$	BT
$F\frac{d\sigma_0}{d\Omega}$	$2\mathrm{R}e(S_2D^*+S_1N^*)$	BT
$O_x\frac{d\sigma_0}{d\Omega}$	$-2\mathrm{I}m(S_1N^*+S_2D^*)$	BR
$O_z\frac{d\sigma_0}{d\Omega}$	$-2\mathrm{I}m(S_2S_1^*+ND^*)$	BR
$C_x\frac{d\sigma_0}{d\Omega}$	$-2\mathrm{R}e(S_2N^*+S_1D^*)$	BR
$C_z\frac{d\sigma_0}{d\Omega}$	$-\|N\|^2-\|S_1\|^2+\|S_2\|^2+\|D\|^2$	BR
$T_x\frac{d\sigma_0}{d\Omega}$	$2\mathrm{R}e(S_1S_2^*+ND^*)$	TR
$T_z\frac{d\sigma_0}{d\Omega}$	$2\mathrm{R}e(S_1N^*-S_2D^*)$	TR
$L_x\frac{d\sigma_0}{d\Omega}$	$2\mathrm{R}e(S_2N^*-S_1D^*)$	TR
$L_z\frac{d\sigma_0}{d\Omega}$	$-\|N\|^2+\|S_1\|^2+\|S_2\|^2-\|D\|^2$	TR

Table 1.3 Beam-target observables in single-pion photoproduction

	Photon		
	unpolarized	circularly polarized	linearly polarized
Target			
unpolarized	$d\sigma/d\Omega$	-	Σ
longitudinally	-	E	G
transversely	T	F	H,P

cross section is given as [18]

$$\begin{aligned}\frac{d\sigma}{d\Omega} = \frac{d\sigma_0}{d\Omega}\,(1 &- P_\ell\Sigma\cos(2\alpha)\\ &+ P_X\left[-P_\ell H\sin(2\alpha)+P_\odot F\right]\\ &- P_Y\left[-T+P_\ell P\cos(2\alpha)\right]\\ &- P_Z\left[-P_\ell G\sin(2\alpha)+P_\odot E\right])\ ,\end{aligned} \tag{1.5}$$

where $P_\odot$ is the right-circular beam polarization, P_ℓ is the linear beam polarization (at an angle α with respect to the reaction plane), and $P_{X,Y,Z}$ are the components of

the target polarization in the x, y, and z directions, respectively.

For experiments with circularly polarized beam and transversally polarized target, $P_\ell = 0$ and, because the z-axis is perpendicular to the target polarization, $P_X = P_T \cos(\varphi)$, $P_Y = P_T \sin(\varphi)$, and $P_Z = 0$, Eq. (1.5) can be simplified to

$$\frac{d\sigma}{d\Omega} = \frac{d\sigma_0}{d\Omega} \left(1 + P_T T \sin(\varphi) + P_T P_\odot F \cos(\varphi)\right) \ , \tag{1.6}$$

where P_T is the target polarization and φ the angle from the reaction plane to the target polarization direction. The reaction is shown in Fig. 1.9.

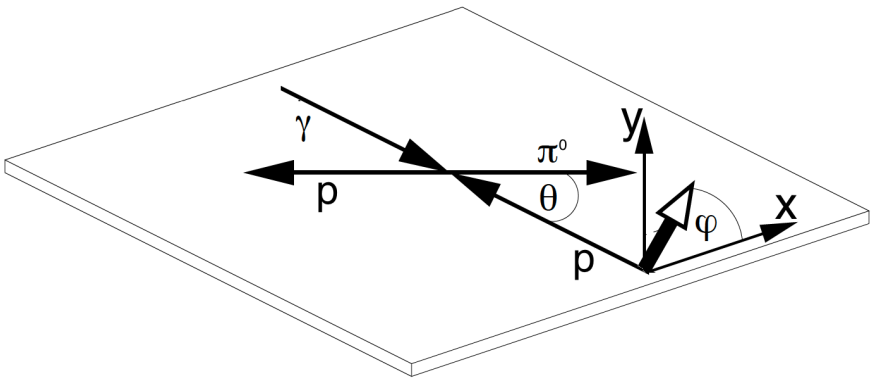

Figure 1.9 Schematic of the $\gamma p \to \pi^0 p$ reaction in the center-of-mass frame with circularly polarized photon beam and transversally polarized target.

1.4 Previous Measurements and Theoretical Predictions

The research of pion photoproduction reactions started in 1970s. By the end of 1979, the first experimental data were taken and analyzed in several research facilities, by M. Fukushima [19], P. Feller [20], P.J. Bussey [21], and P.S.L. Booth [22]. As the spearhead in this area, although the precision of the data analysis was limited by immature experimental equipment and computing technology, the research in that era already constrained further partial-wave analyses and improved the extraction of

proton resonance properties. Moreover, the pioneers of that era have built a solid foundation for the following research. For example, I. S. Barker, A. Donnachie, and J. K. Storrow [18] established the formalism for the research of pion photoproduction reactions. Another important publication was made by D. Besset in 1979 [23]. It explaines the procedure and the necessary estimators in the data analysis of polarization measurements, which solved some technical problems with the data from real-world detectors such as the nonuniform acceptance of detectors.

In 1990s, as some reasearch facilities of the new generation became operational, the study of pion photoproduction reactions continued developing. Besides the CLAS detector at Jefferson Lab, the Bonn Electron Stretcher Accelerator (ELSA) and the Mainz Microtron (MAMI) are among the most advanced reasearch facilities for photoproduction reactions.

In the year of 2014, J. Hartmann et al. [24] published their experimental results of observable T on the photoproduction of neutral pions at ELSA. Their results cover the center-of-mass energy W range from 1.460 GeV to 1.622 GeV and are shown in Fig. 1.10. The result from J. Hartmann et al. found no evidence for additional structures beyond established resonances and the $N(1520)3/2^-$ helicity amplitudes are deduced.

Experimental data of T and F from MAMI were published by J. R. M. Annand et al. [25] in 2016. The photon energies of their results are from 425 MeV to 1445 MeV as shown in Fig. 1.11 and Fig. 1.12. The result from J. R. M. Annand et al. shows the presence of the resonances $N(1520)3/2^-$ and $N(1680)5/2^+$ and their interference with $\Delta(1232)3/2^+$, $\Delta(1700)3/2^-$, and $\Delta(1950)7/2^+$ and nonresonant background.

So far, the results of observables T and F in this analysis agree with previous measurements in the overlapped range of energies. The major difference between the results in this analysis and the results from previous measurements is the difference of the coverage of the energy. In this analysis, the upper limit of the photon energy

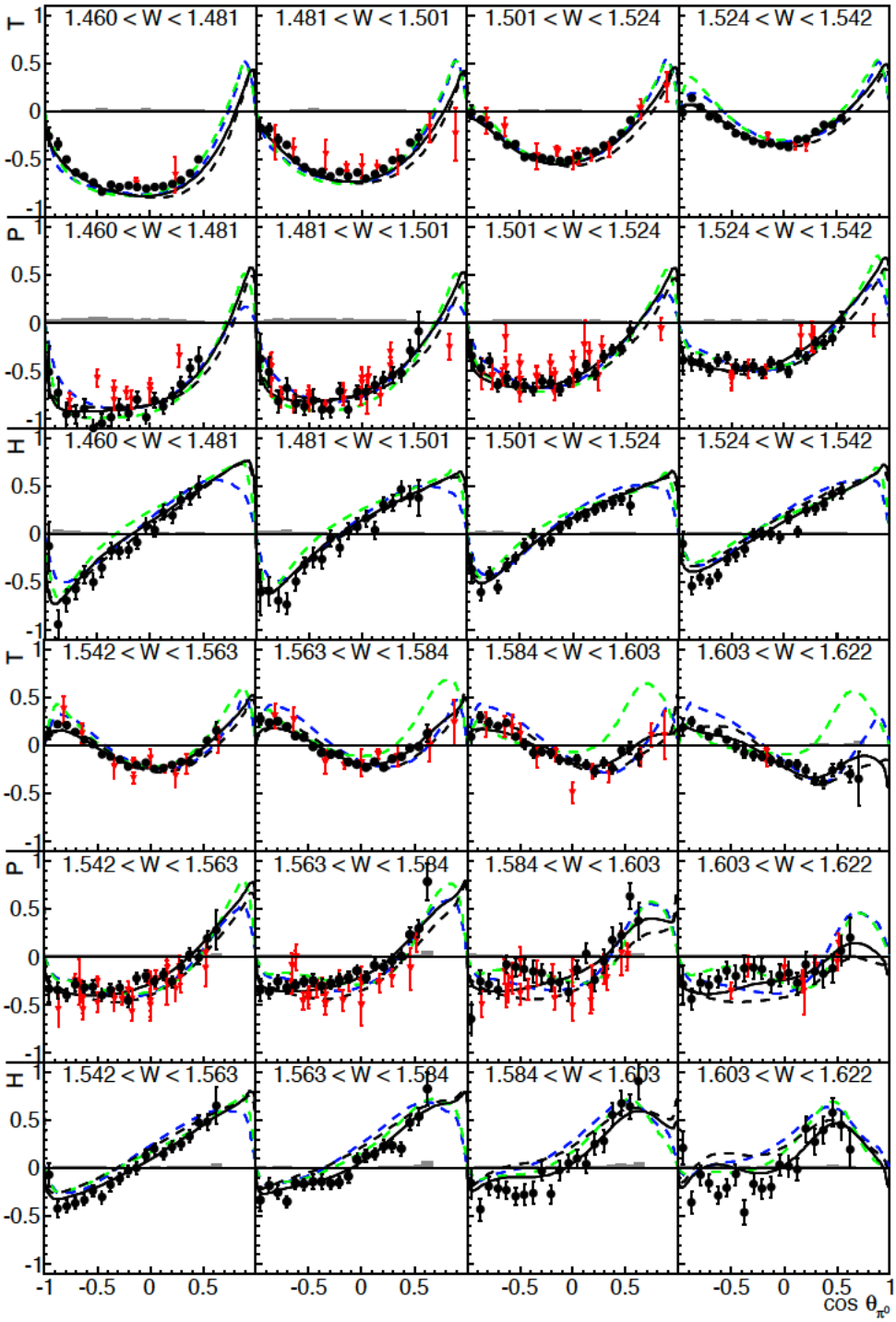

Figure 1.10 The observables T, P, and H from J. Hartmann et al. [24]. The data are compared to earlier data (red) and predictions from BnGa2011 (black), MAID (green), and SAID CM12 (blue).

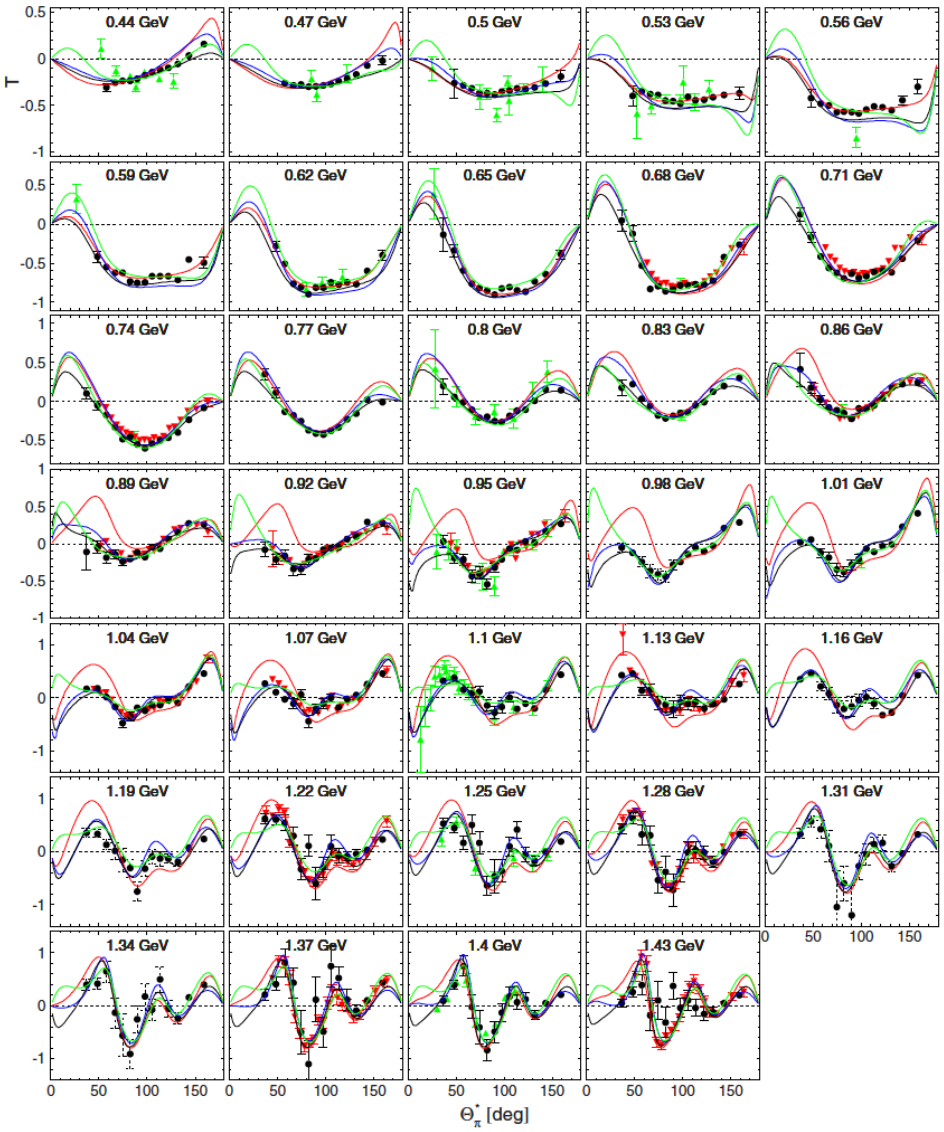

Figure 1.11 The T observable from J. R. M. Annand et al. [25]. The data (filled circles) are compared to experimental data (triangle) and predictions from MAID (red), SAID PR15 (blue), BG2014-2 (black), and JuBo2015-B (green).

is much larger, up to 2850 MeV, compare to the photon energy of 1445 MeV from the most recent measurement. This will make it possible for the theoretical researchers to study the pion photoproduction of this reaction channel in a much larger energy range.

While the experimental research of pion-photoproduction reactions keeps its paces

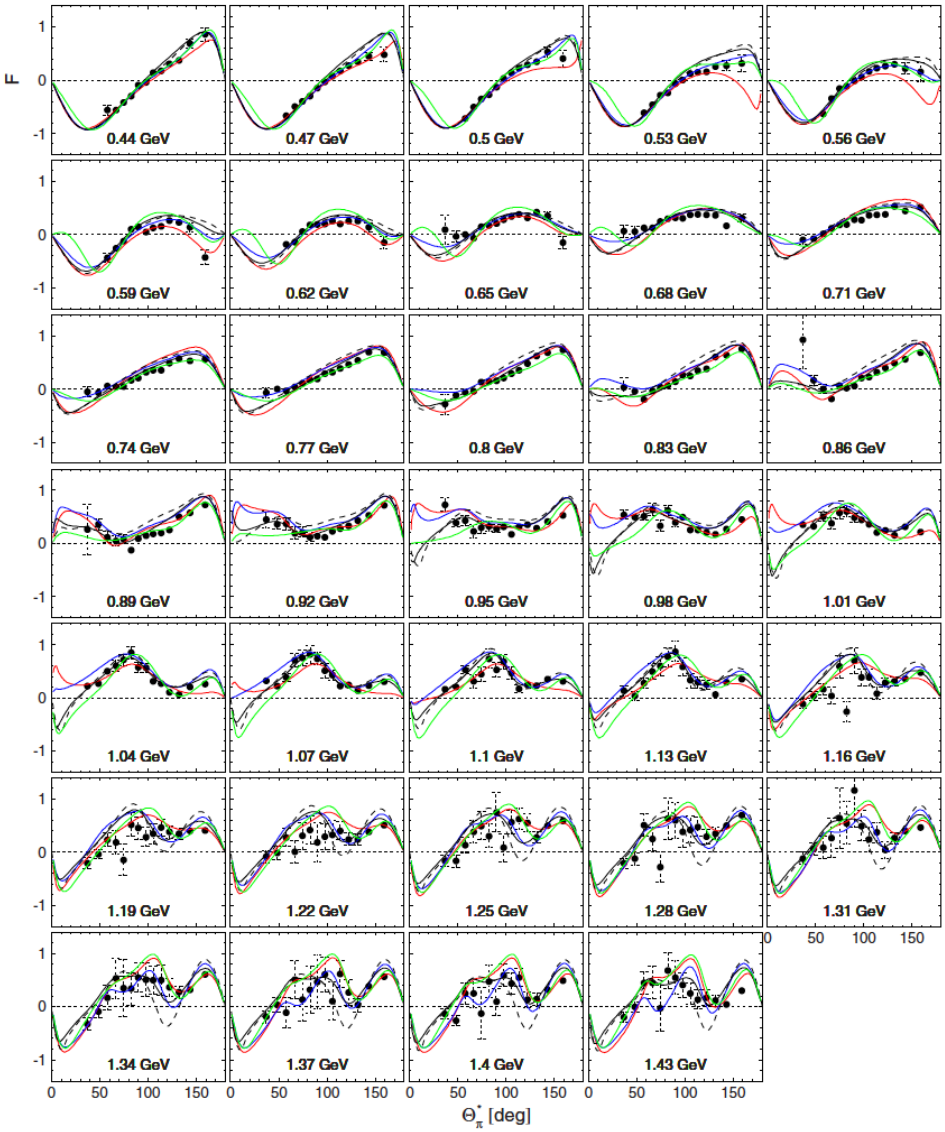

Figure 1.12 The F observable from J. R. M. Annand et al. [25]. The data (filled circles) are compared to experimental data (triangle) and predictions from MAID (red), SAID PR15 (blue), BG2014-2 (black), and JuBo2015-B (green).

of development in recent years, the theoretical researchers in this area are also updating their fits to newer data. There are several leading groups focusing on the development of their models through partial-wave analyses of experimental data, such as the SAID partial-wave analysis [26], Bonn-Gatchina partial-wave analysis [27], and MAID partial-wave analysis [28], or the dynamical coupled-channel approach by the

Jülich-Bonn group [29]. Currently, the SAID MA27 is the latest prediction for the polarization observables T and F. The SAID predictions were frequently updated since the SM95 solution.

The complex amplitudes that determine the pion-photoproduction reaction require eight observables to make a complete partial-wave analysis. However, the existing data consist mainly of unpolarized cross sections and single-polarization observables. Thus, data of double-polarization observables, especially in the energy range that was not included in previous measurement, become useful for the partial-wave analysis to fulfill the completeness in the determination of the pion-photoproduction reaction.

The purpose of this work is to extract polarization observables T and F for the single-pion photoproduction reaction in order to be used for the partial-wave analysis to fulfill the completeness in the determination of the pion-photoproduction reaction and study the pion photoproduction of this reaction channel in a much larger energy range. The data will partially solve the problem of the incomplete set of required observables that determine the pion-photoproduction for further partial-wave analyses and the extraction of proton resonance properties. The details of the methods in this analysis are described in Chapter 3.

Chapter 2

Experiment

This experiment, E03-015 "Pion Photoproduction from a Polarized Target" [30], was conducted at the Thomas Jefferson National Accelerator Facility (Jefferson Lab) [31]. As one of 17 national laboratories funded by the U.S. Department of Energy, the primary mission of the laboratory is to conduct basic research of the atom's nucleus and its fundamental constituents [32]. Jefferson Lab is located in Newport News, VA. An aerial view of the Continuous Electron Beam Accelerator Facility (CEBAF) accelerator complex and domed, partly underground experimental Halls A, B, and C in the foreground, is shown in Fig. 2.1.

Figure 2.2 shows a schematic overview of the CEBAF accelerator and experimental halls. Longitudinally polarized electrons from the electron source were accelerated to 67 MeV and injected into the accelerator. The electrons were accelerated up to 6 GeV after five accelerating passes through pairs of antiparallel 600 MeV linear accelerators (linacs) connected by recirculation arcs and delivered to the experimental halls. The maximum capacity of this system was to deliver highly polarized continuous-wave beams to three experimental halls with a current of up to 200 μA. The beam had a 2.004 ns bunch structure. The facility has now been upgraded to accelerate electrons up to 12 GeV and includes a new Hall D.

The data of the experiment for this analysis were taken as part of the g9 run group from March 18 to August 12, 2010 using the CEBAF large acceptance spectrometer (CLAS) in Hall B at Jefferson Lab. An overview of experimental parameters of the experiment are given in Table 3.2.

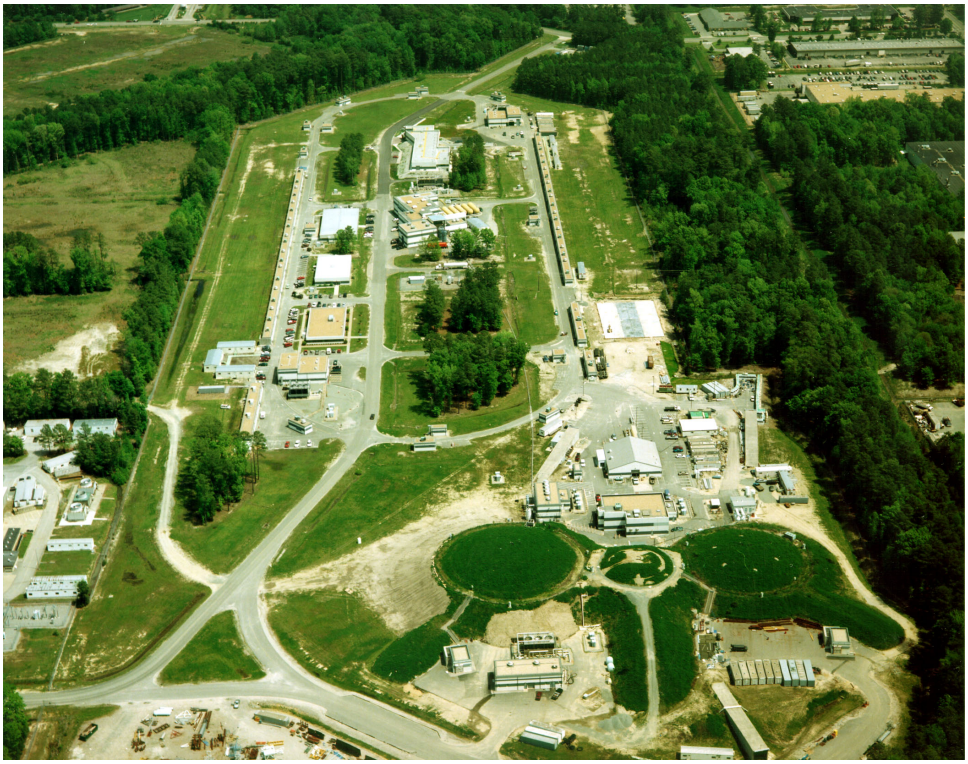

Figure 2.1 Areal view of Jefferson Lab with the Continuous Electron Beam Accelerator Facility (CEBAF) and experimental halls before the 12 GeV energy upgrade. This figure is from [32].

2.1 Photon Beam

After receiving the accelerated electrons from the CEBAF accelerator, a polarized photon beam was produced by using the bremsstrahlung technique. Figure 2.3 shows an overview of the Hall B photon tagger [34]. Longitudinally polarized electrons were incident on the radiator and produced circularly polarized tagged photons as the bremsstrahlung radiation of the incoming electrons. The energy of the outgoing photon E_γ was determined from the energy of the incident electron E_0 and the energy of the electron after the bremsstrahlung reaction E_e. Neglecting the small energy transfer to the nucleus,

$$E_\gamma = E_0 - E_e. \tag{2.1}$$

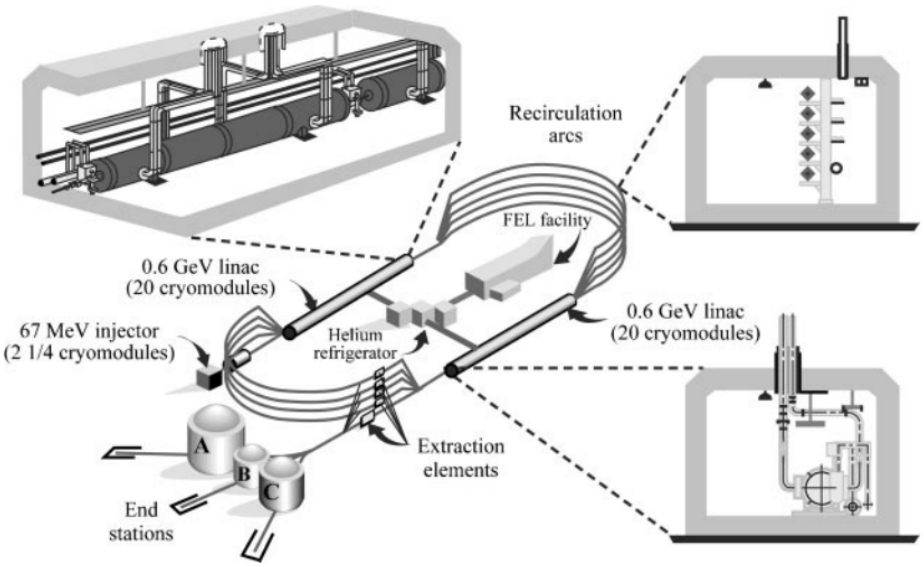

Figure 2.2 Overview of the CEBAF accelerator and experimental halls. The electrons were injected and accelerated up to 6 GeV then delivered to experimental halls. This figure is from [33].

The energy of the outgoing electron was determined by a magnetic spectrometer. Electron hits in any of 384 narrow scintillators (E-counters) determined the electron path through the tagger magnet. The scintillators in the E-plane were partially overlapped to increase segmentation and a photon-energy resolution of $0.001E_0$ were achieved. The time of the hits were also determined in a similar way by 61 T-counters and allowed for the determination of the start time of the events of interest. The maximum range of the tagged photon energy was 20% to 95% of the energy of the incoming electron beam. The size of the scintillators in the E-plane had a thickness of 4 mm, a length of 20 cm, and a width that ranged from 6 to 18 mm. The scintillators in the T-plane were 20 mm thick and the scintillators in the E-plane were 4 mm thick. The T-plane provided a time resolution of 300 ps.

For the circularly polarized photon beam, the polarization was determined by the polarization of the electron beam, the energy of the electron beam, and the energy of the photons. Detailed calculations are shown in Sec. 3.1.

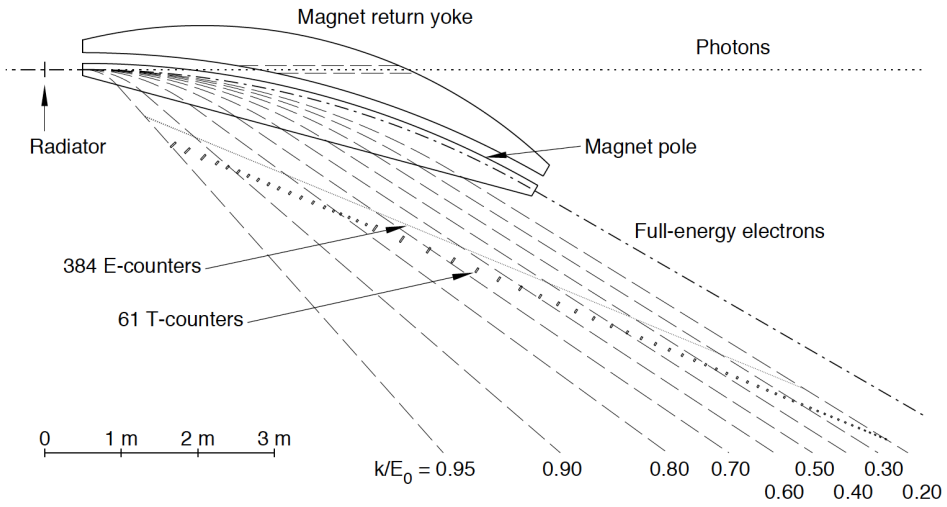

Figure 2.3 Overview of the Hall B photon tagger. Longitudinally polarized electrons were incident on the radiator and produced circularly polarized tagged photons as bremsstrahlung radiation of the incoming electrons. This figure is from [34].

2.2 FROST Target

The FROzen Spin Target (FROST) [35] was used in the g9 experiment. It was particularly designed for the experimental study of baryon resonances with the large acceptance CLAS detector. Particle detection over a large polar angle up to 135° was permitted by the FROST target. The major components of FROST include the polarizing magnet, the dilution refrigerator, target material, and the holding coils.

The material of the FROST target is butanol and centered at $z = 0$ and covered a range of 52.7 mm along the beamline. Additional 1.5-mm thick carbon and 3.5-mm thick polyethylene disks were mounted approximately 9 cm and 16 cm downstream of the butanol sample. The target material (butanol) was polarized with microwaves via Dynamic Nuclear Polarization (DNP) in the field generated by the polarizing magnet with a maximum field of 5.1 T. The target was then cooled to a temperature less than 50 mK without the microwaves and the polarization was maintained with the holding field generated by the holding coils. The schematic view of the target is

shown in Fig. 2.4.

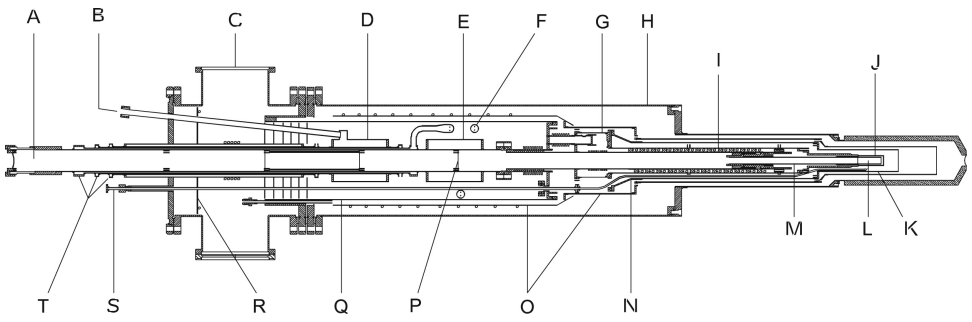

Figure 2.4 Sectional view of the frozen spin target [35]. A, beam pipe; B, LHe inlet; C, ^{3}He pump port; D, 4 K pot; E, 1 K pot; F, 1 K heat exchanger; G, still; H, vacuum chamber; I, sintered heat exchanger; J, mixing chamber; K, holding coil; L, target cup; M, target insert; N, 1 K heat shield; O, 20 K heat shield; P, beam pipe heat shield (one of three); Q, ^{3}He pump tube; R, copper cold plate; S, waveguide; T, precool heat exchanger.

The target polarization was measured by the Nuclear Magnetic Resonance (NMR) measurements [35]. There were two NMR systems in the g9 experiments. The first system was utilized during the DNP process and was tuned to 212.2 MHz. The second system was utilized when the spin was frozen and was tuned to 21.9 MHz. The result of the NMR measurements is discussed in Chapter 3.

When operated, the system could run continuously for a typical period of 6 months. During the full length of the running period, there were several cycles separated by the flip of the polarization direction of the target. The flips of the polarization direction are useful in the analysis and are explained in Sec. 3.8. A typical cycle of operation started with the dynamic nuclear polarization process with a maximum field of 5.1 T. After the target was polarized to approximately 90%, it was cooled by with a ^{3}He–^{4}He dilution refrigerator to below 50 mK and the field of the holding coils held the polarization of the target for several weeks until the polarization reached approximately 70% in the g9b experiment. The cycles of the operation of the frozen-spin target are shown in Fig. 2.5.

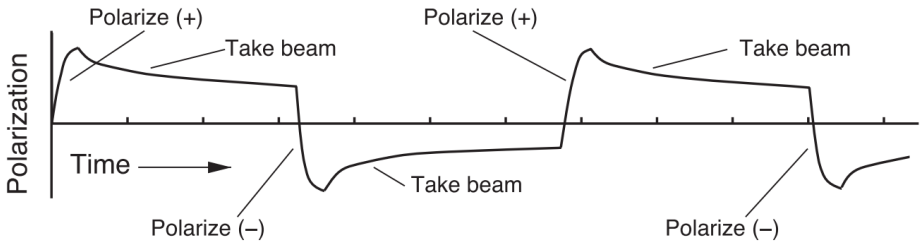

Figure 2.5 Cycles of the operation of the frozen spin target [35]. Three full operation cycles are shown. The polarization direction of the target is flipped between two adjacent cycles.

A carbon target was placed down stream to provide bound protons to measure the bound nucleon background of the butanol data since the butanol-target events contain both free-proton and bound-proton events. In the g9b experiment, the carbon target was placed approximately 9 cm downstream of the butanol target.

2.3 CLAS Detector

The CEBAF Large Acceptance Spectrometer (CLAS) [36] was based on a multigap magnet with six super-conducting coils, symmetrically arranged to generate an approximately toroidal field distribution. The CLAS detector has been used for various experiments including the present pion photoproduction experiment. One distinct aspect of the CLAS detector was the large-acceptance detection with a polar-angle range from 8° to 142°. It is particularly suited in the study of reactions with low luminosity (e.g., experiments using a tagged-bremsstrahlung photon beam) or reactions with multi-particle final states. The CLAS detector had several major parts including the torus magnet, the time-of-flight counters, the Cherenkov counters, and the drift chambers. The schematic view of the CLAS detector can be found in Fig. 2.6. This design made it possible to detect final-states particles in a wide angular range. Another schematic view of the CLAS detector cut perpendicular to the beam is shown in Fig. 2.7 [36] and demonstrates the azimuthal coverage of the detector.

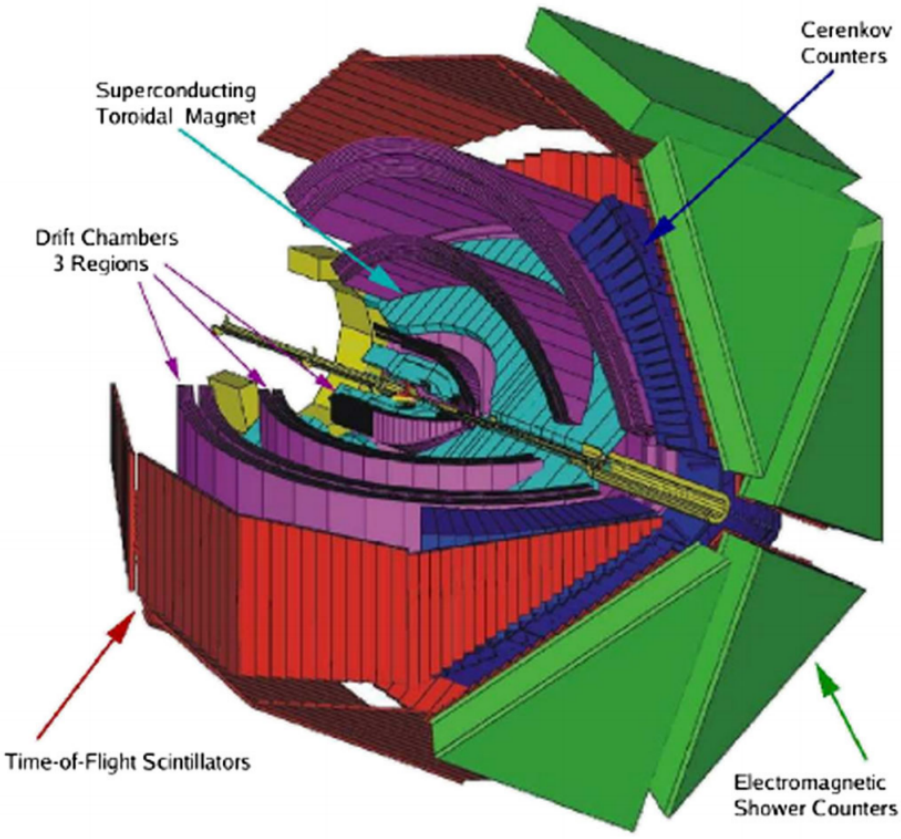

Figure 2.6 Schematic view of the CLAS detector, including drift chambers, Cherenkov counters, electromagnetic calorimeter, and the time-of-flight counters. These detectors cover almost the entire sphere except the very forward and backward angles along the beamline. This figure is from [37].

The purpose of the torus magnet [38] in the CLAS detector was to analyze the momentum of the final-states particles with the tracking assistance of the drift chambers. The magnetic field was generated by six coils installed around the beam line. Each coil consisted of four layers of 54 turns of aluminum-stabilized NbTi/Cu superconductor and was cooled to 4.5 K by liquid helium through cooling tubes located at the edge of the windings. The maximum current was 3860 A with a maximum integral magnetic field of 2.5 Tm.

The contours of constant magnetic field in the midplane between two coils are shown in Fig. 2.8. The field orientation is shown in Fig. 2.9. When the current

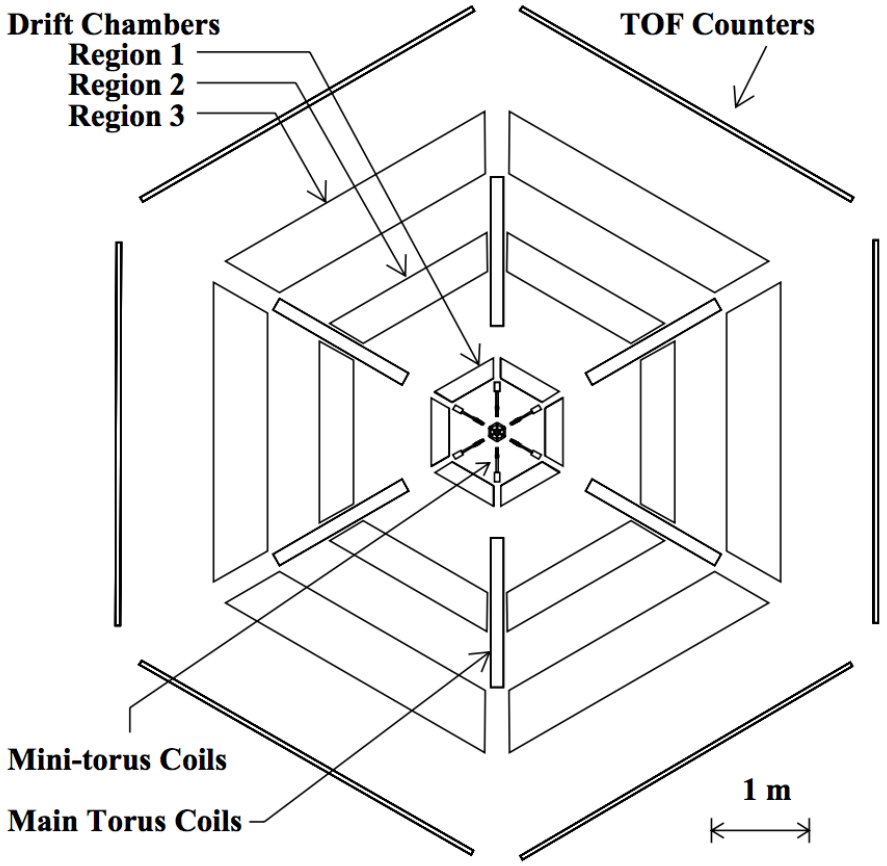

Figure 2.7 Schematic view of the CLAS detector perpendicular to beam [36]. These detectors have a large azimuthal coverage.

was set to positive, the positively charged particles were bent toward the beam axis and the negatively charged particles were bent away from the beam axis. When the current was set to negative, the positively charged particles were bent away from the beam axis and the negatively charged particles were bent toward the beam axis. In the g9 experiment, the system was running at +1920 A to moderately bend the positively charged particles and negatively charged particles toward and away from the beam axis, respectively, and make both positively and negatively charged particles have large acceptances over the θ^{lab} angle.

The drift chambers [39] were used to track the final-state charged particles. In the detector, there were 18 drift chambers creating 35148 hexagonal drift cells. When a

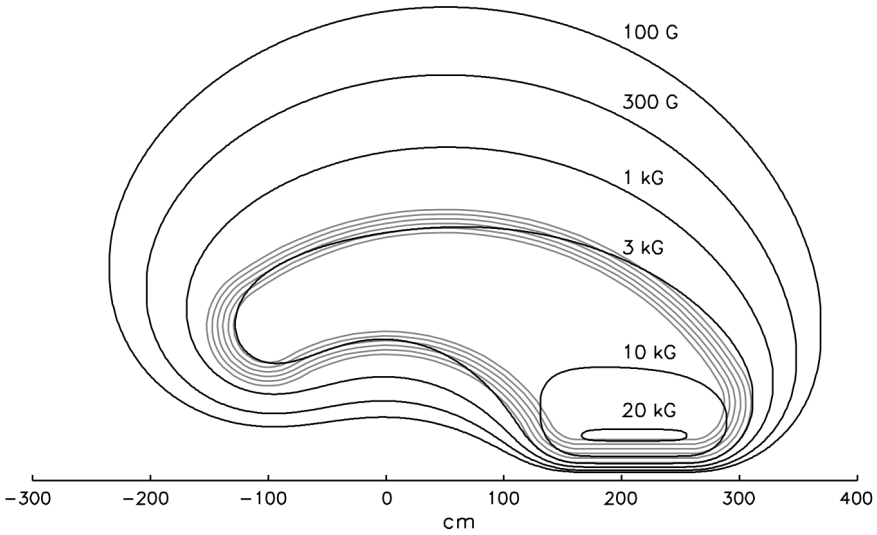

Figure 2.8 The magnetic field for the CLAS toroid in the midplane between two coils [36].

charged particle traveled through a drift chamber, the drift cells along its trajectory were triggered. By aligning the triggered drift cells, the trajectory of the particle was known. The three momentum and the charge of the particles were calculated from the trajectory of the particle and the magnetic field. The track length and the reaction vertex were also reconstructed by using information of particles from the drift chambers. This process is illustrated in Fig. 2.10 [39].

The CLAS time-of-flight system [40] consisted of 57 scintillator paddles in each of the six sectors. Each scintillator paddle was 5.08 cm thick and 15 or 22 cm wide, with lengths from 32 cm at the most forward angle to 450 cm at larger angles. For each scintillator paddle, two photomultiplier tubes were placed at both ends of the scintillator paddle. The whole area of coverage was 206 m^2. The view of TOF counters in one sector is shown in Fig. 2.11 [40]. The performance of the system allowed for particle separation by using the time-of-flight information measured for momenta up to 2 GeV due to a time resolution of typically 150 ns.

The hexagonal-shaped plastic scintillation counter system (start counter) [41] was

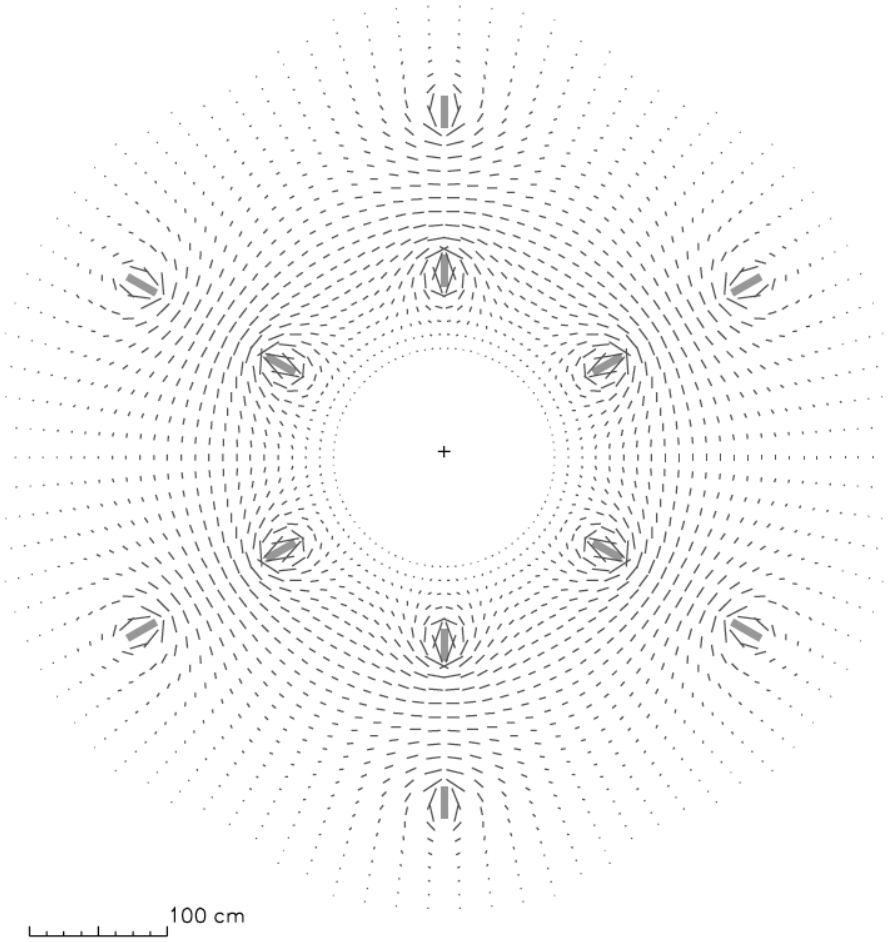

Figure 2.9 The magnetic field orientation. Magnetic field vectors transverse to the beam in a plane centered on the target [36].

placed right outside the target. It was used to measure the start time of events. A sketch of the start counter is shown in Fig. 2.12. Outgoing particles produced light in the 2.2-mm thick scintillators and triggered signals in the PMTs that were coupled to the scintillators with a light guide. The time resolution of the start counter was 350 ps. It is less than the 2.004 ns bunch structure of the beam.

2.4 Beamline Devices

To measure the electron beam position, three beam-position monitors were installed 36.0, 24.6, and 8.2 m upstream of the target. Due to low beam currents, the beam

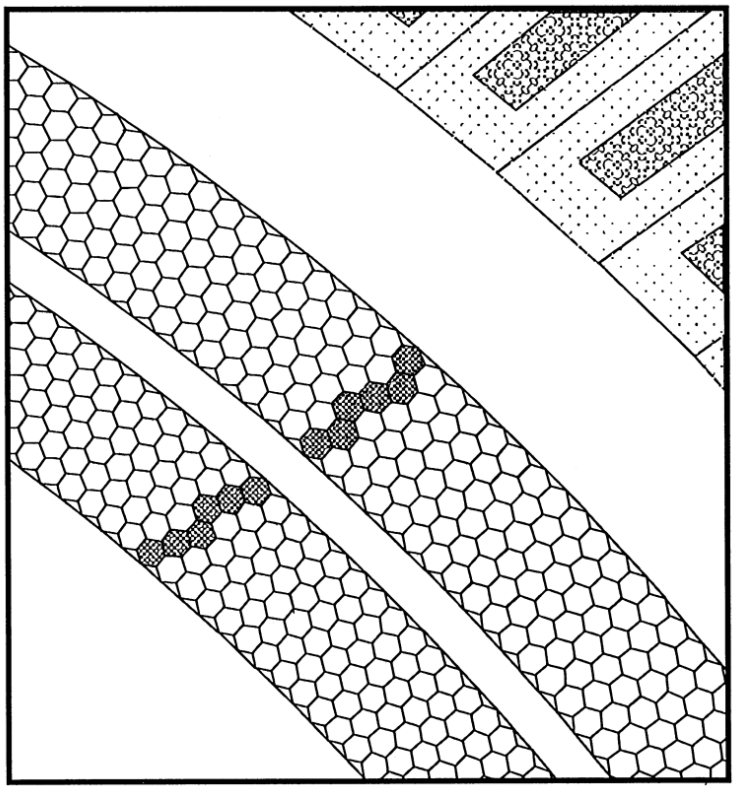

Figure 2.10 The drift process measured by the drift chambers [39]. The drift cells of region 3 along its trajectory that triggered are drawn in dark.

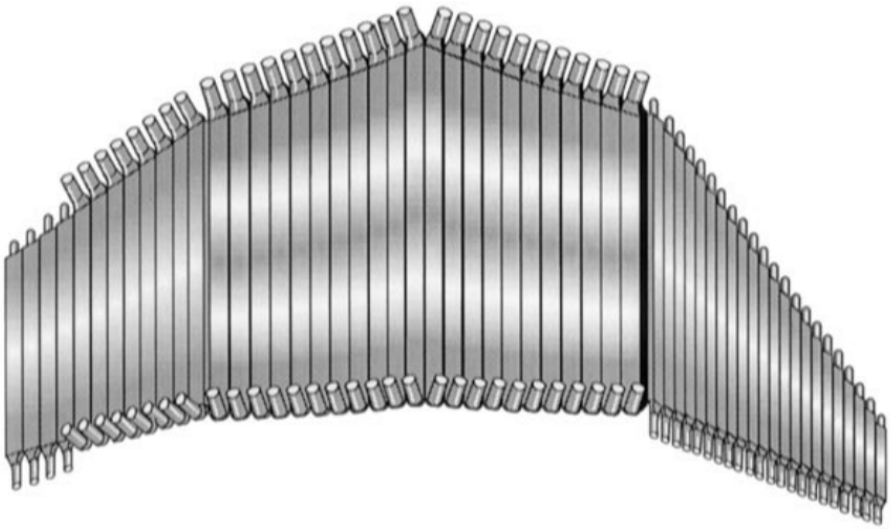

Figure 2.11 View of TOF counters in one sector of the time-of-flight system [40].

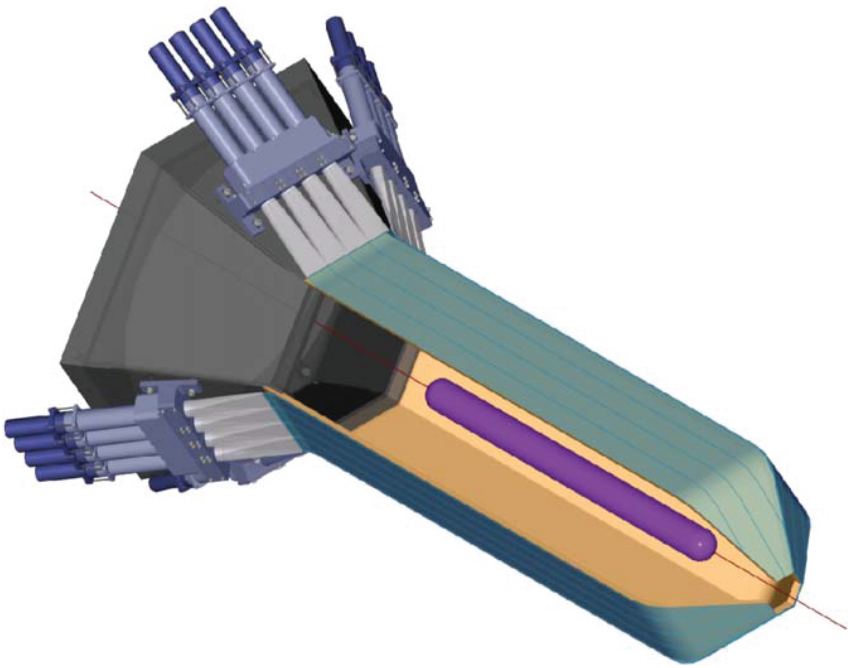

Figure 2.12 Sketch of the start counter [41].

position and intensity were measured with a measurement rate of about 1 Hz. The profile of the electron beam was also measured. Thin wires were moved through the beam and scattered electrons were detected to reconstruct the electron beam profile. The wires were oriented along the horizontal and vertical axes with the moving device (harp). There were three harps installed at 36.7, 22.1, and 15.5 m upstream of the target.

The Møller measurements [36] was used to measure the electron-beam polarization. It was installed upstream of the tagging system. To make a high-precision measurement of the beam polarization, the asymmetry in elastic electron-electron scattering has been measured. The scattering target was a 25-μm thick permendur foil, magnetized with a Helmholtz-coil system. Additionally, there are two quadrupole magnets and two detectors on both sides. The scattered electrons were detected in coincidence to determine the reaction kinematics. The Møller measurements were conducted every two days and cost 30 minutes for each measurement.

Chapter 3

Data Analysis

For the $\gamma p \to \pi^0 p$ reaction in the FROST g9b experiment with CLAS, the circularly polarized tagged photons in the energy range from 0.62 GeV to 2.93 GeV of the electron beam were produced by the radiator of the Hall-B Photon Tagger from incident longitudinally-polarized electrons with energies of 3.082 GeV. The photon-beam helicity was flipped pseudo randomly at a rate of 240 Hz or 30 Hz. The collimated photon beam irradiated the FROST target. The nuclear spin of free protons in the target was polarized and the target polarization direction was changed periodically. A carbon target and a polyethylene target were used downstream of the butanol target for background subtraction and comparison use. The final-state protons from those targets were detected by the CLAS detector.

3.1 Beam and Target Polarizations

The circularly polarized tagged photons were produced by the Bremsstrahlung process from incident longitudinally polarized electrons. The polarization of the photon beam depends on the ratio between the photon energy E_γ and the electron energy E_0. Specifically, the degree of the circular polarization is expressed as [42]

$$P_\odot = P_e \frac{4x - x^2}{4 - 4x + 3x^2}, \tag{3.1}$$

where $x = E_\gamma / E_0$.

The electron-beam polarization was measured by Møller measurements [43]. The electron-beam polarization as a function of the run number is shown in Fig. 3.1

and was found to be consistent with a constant polarization throughout the experiment. The average electron-beam polarization and statistical uncertainty are $P_e = 0.873 \pm 0.006$, while the systematic uncertainty of Møller measurements in Hall B were 3% [43]. The electron-beam helicity was pseudo-randomly flipping at a rate of 240 Hz (30 Hz for the Møller measurements). The g9b experiment ran concurrently with the Qweak experiment [44]. The helicity reporting was delayed. This is common for parity-violation experiments, like Qweak, with special demanding requirements on helicity-correlated beam properties. The beam helicity of a given event was determined during initial data analysis and stored event-by-event in the event's header bank (HEAD): bit 29 contains the helicity bit of the event and bit 30 indicates whether or not the helicity was correctly reconstructed [43].

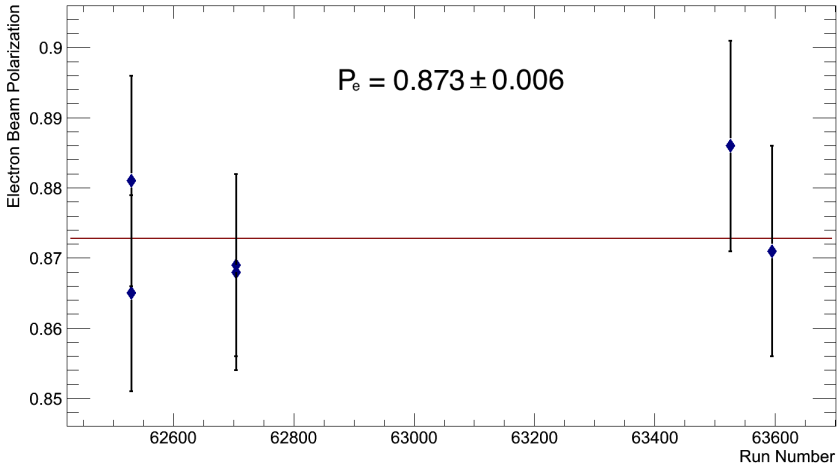

Figure 3.1 The electron-beam polarization measured by the Møller measurements. The horizontal line indicates the mean value of the six measurements.

The free protons in the butanol target were transversally polarized by dynamic nuclear polarization and kept at low temperature [35]. The target-polarization direction was oriented at an angle φ_0 with respect to the horizontal direction in the lab frame (x^{lab}) for the nominally positive polarization direction. The angle φ between the reaction plane and the target-polarization orientation was determined event by

event from the measured azimuthal angle of the detected proton, $\varphi_p^{\rm lab}$,

$$\varphi = -\varphi_\pi^{\rm lab} + \varphi_0 = \pi - \varphi_p^{\rm lab} + \varphi_0. \tag{3.2}$$

All relevant angles are illustrated in Fig. 3.2. In this analysis a value of $\varphi_0 = 116.3^\circ \pm 1.4^\circ$ was used that was determined in a moment-method analysis, see Sec. 3.8.

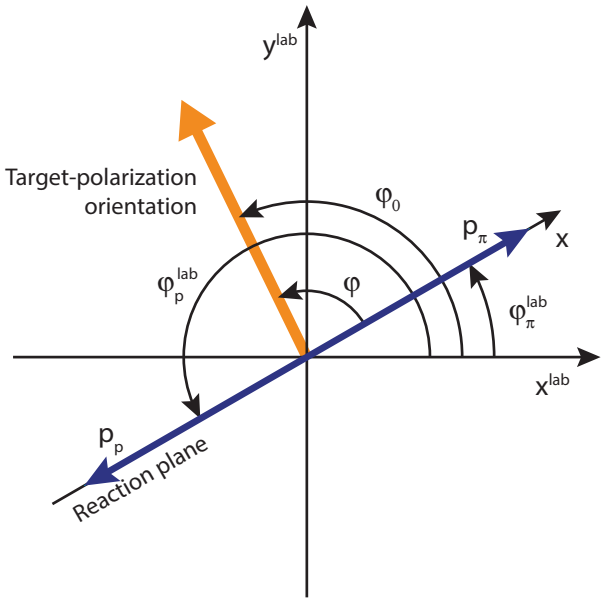

Figure 3.2 Target polarization orientation in the lab- and reaction frames.

The Nuclear Magnetic Resonance (NMR) measurements provide the degree of target polarization. The target polarization values were determined by Y. Mao in [45]. The target polarization as a function of the run number is shown in Fig. 3.3. Spin alignments along the $\varphi_0 = 116.3^\circ$ direction are marked with blue symbols; alignments in the opposite direction are marked with red symbols. The target polarization decreased with time and the target was routinely repolarized to the opposite direction after a number of runs. The relaxation time during g9b was about 3400 h for positive polarization with beam and 4000 h without [35]. In this analysis it was assumed that the magnitude of the target polarization is constant within a given run.

An experimental asymmetry signal from the butanol target was analyzed for each run to verify the correct assignment of the target-polarization orientation and to

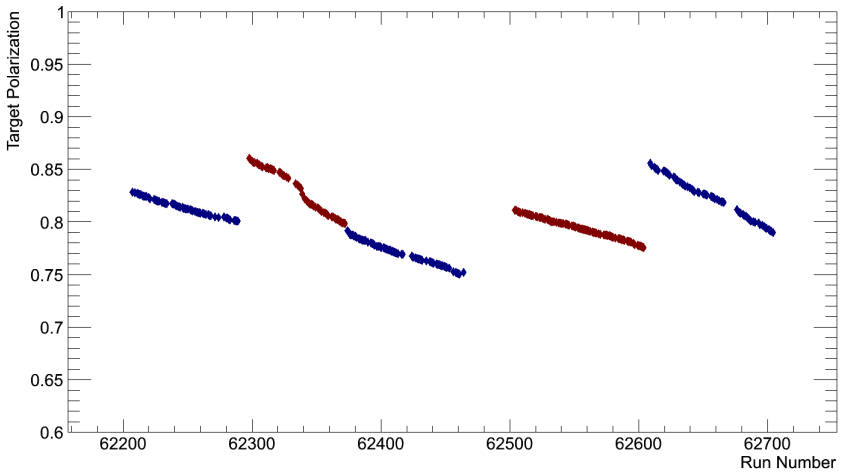

Figure 3.3 The target polarization of the run groups used measured by NMR. Spin alignments along the nominally positive direction ($\varphi_0 = 116.3°$) are marked with blue symbols; alignments in the opposite direction are marked with red symbols. The change of color indicates the target was repolarized to the opposite direction.

investigate systematic uncertainties in the target polarization. The raw asymmetry of observable F served for that purpose, Eq. (3.27) with $h = 1$, as detector acceptances cancel for this observable but not for observable T. The raw asymmetry is inversely proportional to the product of electron beam and target polarizations $P_e P_T$, Eq. (3.1) and Eq. (3.27). For the center-of-mass energy range from $W = 1.5$ GeV to 1.9 GeV and the $\cos\theta$ range from -0.4 to 0.8, the average raw asymmetry is shown in Fig. 3.4 as a function of run number for the runs used in this analysis. The figure also shows the mean values for each of the five run groups (red horizontal lines) and the mean value over all runs (black horizontal line).

Table 3.1 gives the values for those mean values with their statistical uncertainties. The result indicates that the raw asymmetries of all run groups are consistent with each other within their relative uncertainties of 3% to 4%. Within that range, there is no indication of run-group-dependent systematic uncertainties of the product $P_e P_T$. This is consistent with the systematic uncertainty of the beam polarization of 3% [43]

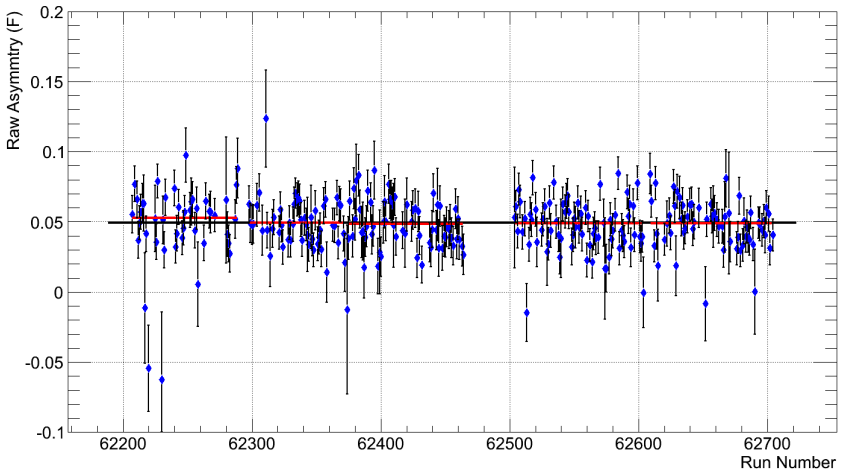

Figure 3.4 The raw asymmetry, Eq. (3.27) with $h = 1$, of the butanol-target events for the run groups 1 through 5 used in the analysis. The horizontal red lines indicate the mean values for the five run groups and the black line indicates the average raw asymmetry over all runs.

Table 3.1 Raw asymmetry of the butanol-target events for the first 5 run groups.

Run group	Raw Asymmetry (F)
1	0.0526 ± 0.0021
2	0.0494 ± 0.0018
3	0.0485 ± 0.0019
4	0.0489 ± 0.0015
5	0.0491 ± 0.0016
Avg.	0.0495 ± 0.0008

and the 4% difference of measured FROST target polarizations with two separate NMR coils reported in [35].

The run information for all run groups is summarized and listed in Table 3.2. The group number, the run-number range, incident electron-beam energy, the number of events, the frequency of the helicity flip, the target polarization, and the orientation of the target holding field [46] are given. The target magnet quenched from a power surge at the end of run group 5. Compared to run groups 1 through 5, run groups 6 though

10 contain only 22% of the statistics and were run with an average target polarization that was about a factor of 0.75 smaller. Assuming everything else being equal, that would result in statistical uncertainties of results from run groups 6 through 10 that are about a factor 3 larger than for results of the first five run groups. On the one hand, including the final five run groups in a combined result could improve the statistical uncertainty by merely 6%. On the other hand, additional systematic uncertainties could affect the final result, given that the replacement target had a different geometry than the original one. In this analysis only the first five run groups were used.

Table 3.2 The g9b run information for circularly polarized beam runs. Given are the group number, the run number, incident electron-beam energy, the number of primary events, the frequency of the helicity flip f, the target polarization and the sign of the target polarization, and the orientation of the target holding field [46].

Group	Run range	E_e (GeV)	Events	f (Hz)	Target pol.	Field
1	62207 - 62289	3.082	723.1 M	240	.83 - .80 (+)	(+)
2	62298 - 62372	3.082	894.9 M	240	.86 - .80 (−)	(+)
3	62374 - 62464	3.082	1129.7 M	240 or 30	.79 - .75 (+)	(+)
4	62504 - 62604	3.082	1307.1 M	240	.81 - .76 (−)	(−)
5	62609 - 62704	3.082	972.6 M	240 or 30	.85 - .79 (+)	(−)
runs not used in this analysis						
6	63508 - 63525	2.266	138.2 M	943	.77 - .58 (+)	(+)
7	63529 - 63542	2.266	166.8 M	240 or 943	.56 - .57 (−)	(−)
8	63543 - 63564	2.266	321.7 M	943	.74 - .61 (+)	(+)
9	63566 - 63581	2.266	249.6 M	943	.70 - .64 (−)	(−)
10	63582 - 63598	2.266	242.3 M	240	.48 - .46 (+)	(+)

3.2 Reaction Vertex

The reconstructed reaction vertex were utilized to categorize events from the butanol, carbon, and polyethylene targets in the beamline. Two distributions of the z coordinate of the reconstructed reaction vertex are shown in Fig. 3.5 for different W and $\cos\theta$. The figure illustrates the categorized targets in three colors based on the z

coordinate of the reconstructed reaction vertex. The z-range of the butanol target was chosen to align with the highest average raw asymmetry from $z = -3$ cm to $z = 2$ cm. The raw asymmetry of observable F starts to decrease beyond $z = 2.0$ cm as shown in Fig. 3.6 because the fraction of events from polarized protons starts to decrease as the reconstructed reaction vertex is approaching the end of actual target at $z = 2.5$ cm. This cut helps to maintain a high average dilution factor. A wider cut would have increased the overall statistics of the data but at the expense of a more diluted asymmetry signal. The ranges of the applied z-vertex cuts for the three targets are listed in Table 3.3.

Table 3.3 Selection criteria for the three targets based on the reconstructed z coordinate of the reaction vertex.

Target	Reaction Vertex (z)
Butanol	-3 cm to 2 cm
Carbon	8 cm to 11 cm
Polyethylene	14 cm to 17 cm

Following Ref. [48] additional cuts have been applied on the transverse vertex coordinates to suppress the fraction of poorly reconstructed proton tracks. The x coordinate and y coordinate of the reconstructed reaction vertex are shown in Fig. 3.7. The distribution peaks at $(x, y) = (-0.31 \text{ cm}, -0.28 \text{ cm})$ and only events with a transverse distance of less than 2 cm from that point were kept in the analysis.

3.3 Particle Identification and Coincidence Time

To identify final-state protons in coincidence with the initial-state photons, events with one positively charged particle and zero negatively charged particles were considered.

The time-of-flight difference of the positively charged particle in each event Δt_p is taken between the measured flight time, t_{exp}, and the flight time t_{calc}, which is

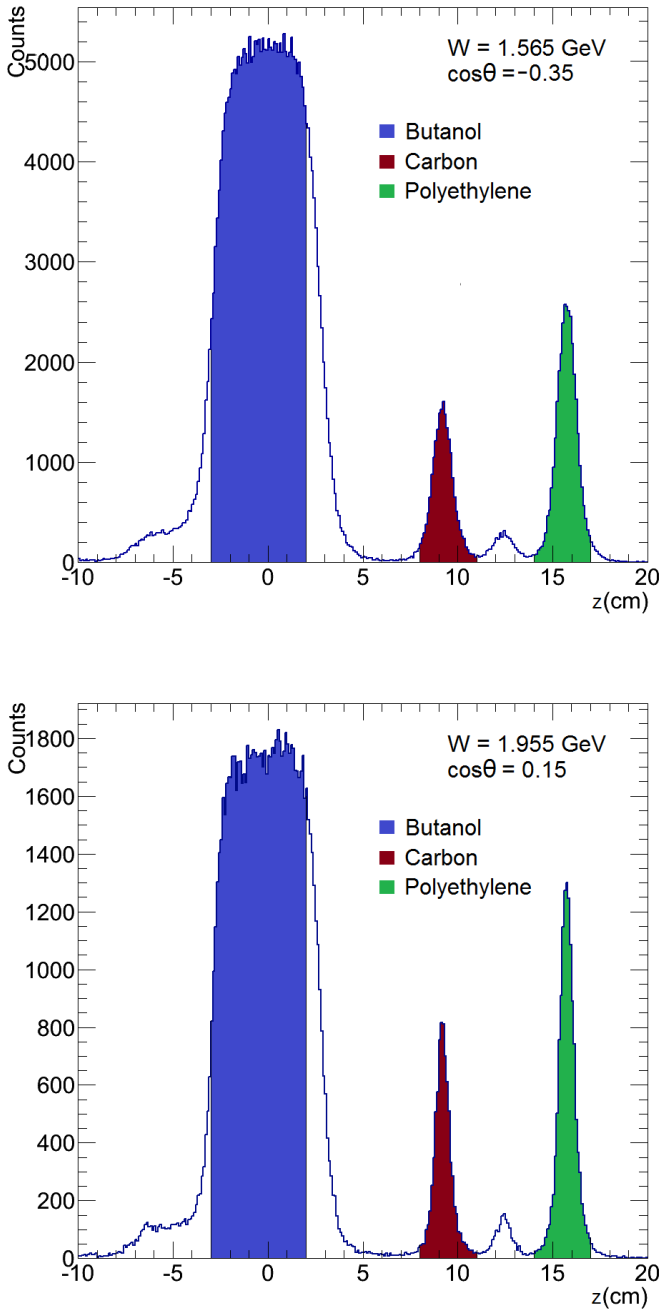

Figure 3.5 Examples of the reconstructed z-vertex distributions of protons. The main structures in the distribution are from the butanol ($z \approx 0$), carbon ($z \approx 9$ cm), and polyethylene ($z \approx 16$ cm) targets. According to the implementation of the target geometry in Ref. [47], the structure at $z \approx 12.5$ cm comes from the 1 K end cap. Three cut ranges are marked with different colors for the various targets.

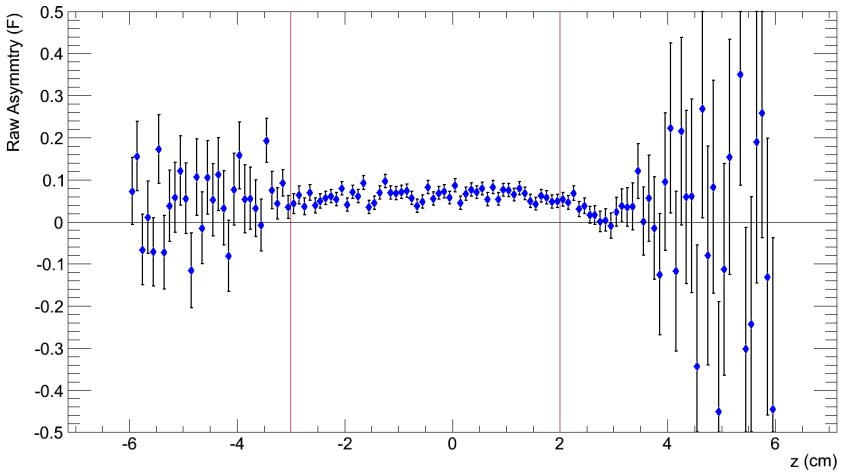

Figure 3.6 The raw asymmetry of observable F as a function of the reconstructed z vertex. Events within the z-range from $z = -3$ cm to 2 cm were chosen for the analysis as indicated between the red lines. The raw asymmetry is increasingly diluted for $z > 2$ cm.

calculated from the momentum p and speed β of the particle under the assumption that the particle was a proton with rest mass m_p:

$$\Delta t_p = t_{exp} - t_{calc} = \frac{\ell_{SC}}{c}\left(\frac{1}{\beta} - \sqrt{\frac{m_p^2 c^2}{p^2} + 1}\right), \tag{3.3}$$

where ℓ_{SC} is the path length from the reaction vertex to the TOF paddles and β is determined from the time of flight and ℓ_{SC}. Δt_p is used to distinguish a proton from other positively charged particles; for protons $\Delta t_p \approx 0$.

The performance of all TOF paddles has been examined by checking Δt_p of each paddle for each run group to reduce the probability of particle misidentification. Examples are shown in Fig. 3.8. Problematic paddles were removed from the analysis as listed in Table 3.4.

The distribution of Δt_p for positively charged particles as function of momentum is shown in the left panel of Fig. 3.9. The central maximum with $\Delta t_p \approx 0$ corresponds to protons and the band at high momentum and negative values of Δt_p

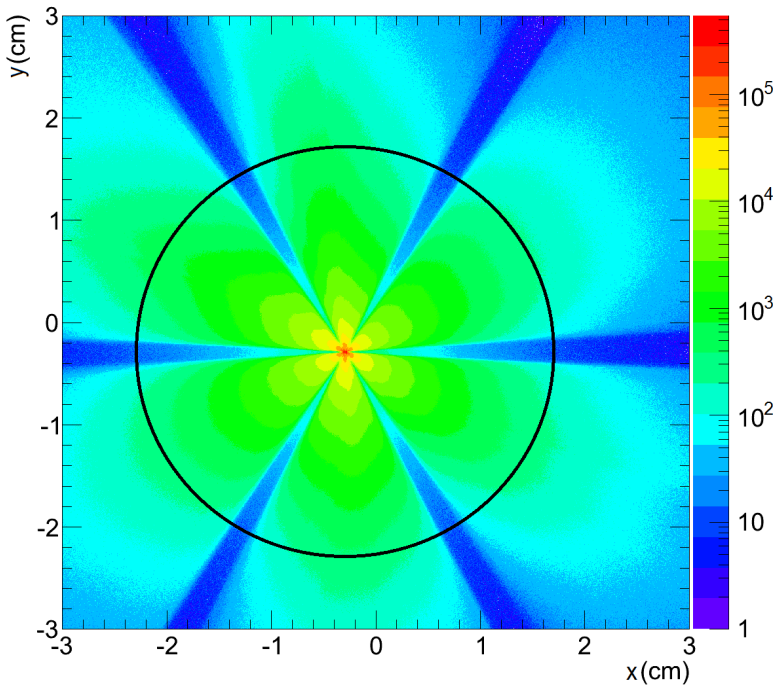

Figure 3.7 The reconstructed (x, y)-vertex distribution of protons. The maximum of the distribution is at $(-0.31$ cm,-0.28 cm). Events within the black circle have been selected for further analysis.

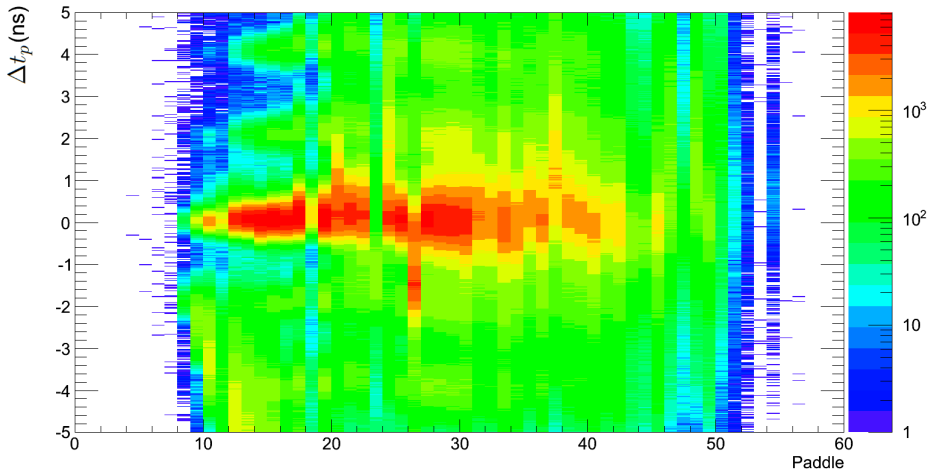

Figure 3.8 The Δt_p distributions of each paddle in sector 3 for run group 2. Paddle 26 was identified as a problematic paddle as Δt_p of this paddle behaved anomalous.

Table 3.4 Paddles that were removed from the analysis for the full run range from run 62207 to 62704.

Sector	Paddles
1	24, 40, 42, 43, 44
2	29, 36, 37, 39
3	23, 26, 37
4	33, 39, 40
5	23
6	—

corresponds to pions. Although most problematic TOF paddles have been removed, timing-related issues remain visible in the distribution as narrow, almost vertical bands at low momenta; most pronounced at about 0.5 GeV/c. These events have signals from paddle readouts that are far smaller than the typical energy deposition E_{dep} in TOF paddles. The right panel of Fig. 3.9 shows the E_{dep} distribution as a function of particle momentum together with a momentum-dependent cut that helps discriminating proton-candidate events with high energy deposition in the paddles from mostly background events with a low signal in the detectors.

To select from all recorded photons the photon that led to the reaction, we also need the CLAS-tagger coincidence time, Δt_c, which is defined as

$$\Delta t_c = t_{v,\gamma} - t_{v,p} = \left(t_\gamma + \frac{z}{c}\right) - \left(t_{p,ST} - \frac{\ell_{ST}}{\beta c}\right), \tag{3.4}$$

where t_γ is the time measured by the tagger and reported at the center of the CLAS detector, z is the reaction vertex z coordinate, $t_{p,ST}$ is the proton time of the Start Counter (ST) subsystem, and ℓ_{ST} is the path length of the proton from the reaction vertex to the ST subsystem hit position. The distribution of Δt_c is shown as function of momentum in the left panel of Fig. 3.10. The central maximum at $\Delta t_c \approx 0$ includes true coincidences between the tagged photon and the event in the CLAS detector. Side peaks are random coincidences. As previously in Fig. 3.9, the distribution of Δt_p is shown in the right panel of Fig. 3.10. This time, however, after applying

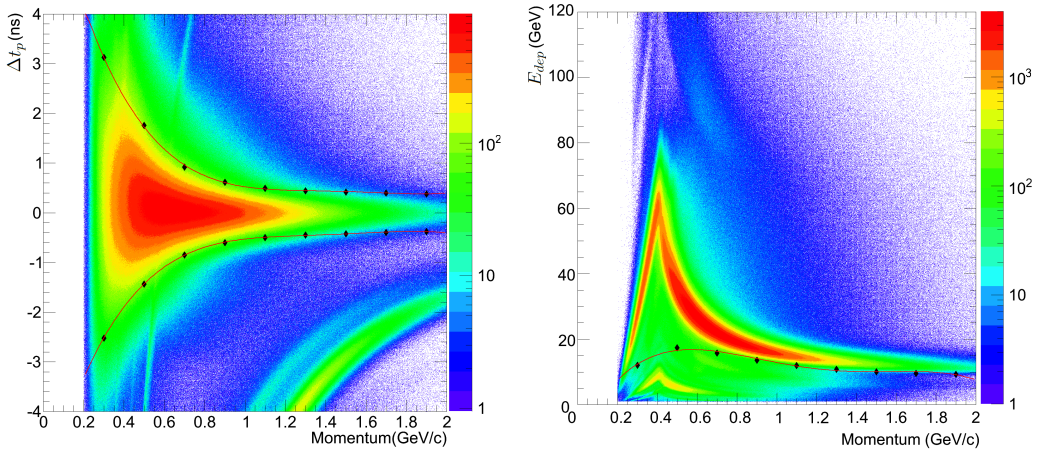

Figure 3.9 Δt_p distribution for positively charged particles in CLAS after removing the TOF paddels of Table 3.4 (left panel). Remaining timing issues are visible in the almost vertical stripes at low momenta. The right panel shows the measured energy deposition E_{dep} in the TOF paddles as a function of particle momentum along with a momentum-dependent cut on that helps suppressing background events with small signals in the detectors.

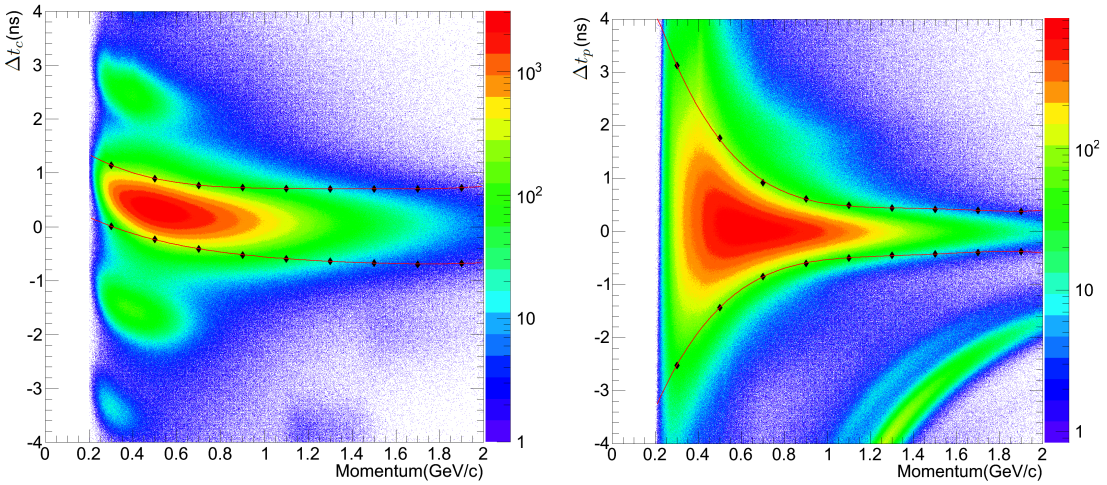

Figure 3.10 The left panel shows the CLAS-tagger coincidence time Δt_c with a shift at low momentum due to large energy loss of low-energy protons. The selection of coincident events is shown in red. The right panel shows the Δt_p distribution for positively charged particles in CLAS after applying the momentum dependent cut on E_{dep}. Events between the red curves were selected as protons in the subsequent analysis.

the momentum-dependent E_{dep} cut that effectively suppresses the background from misidentified particles. The Δt_c and Δt_p distributions are slightly asymmetric at low momenta due to the large energy loss of low-momentum protons. Event selections were made in either case with complex momentum-dependent cuts. The Δt_c and Δt_p distributions were sliced in 0.2-GeV/c wide momentum bins and fitted with gaussian distributions. The cut limits in the center of each momentum bin were chosen as $\pm 2\sigma$ off the distribution's maximum. An example of a gaussian fit to Δt_c data for one slice in momentum between 1.4 GeV/c and 1.6 GeV/c is shown in Figure 3.11.

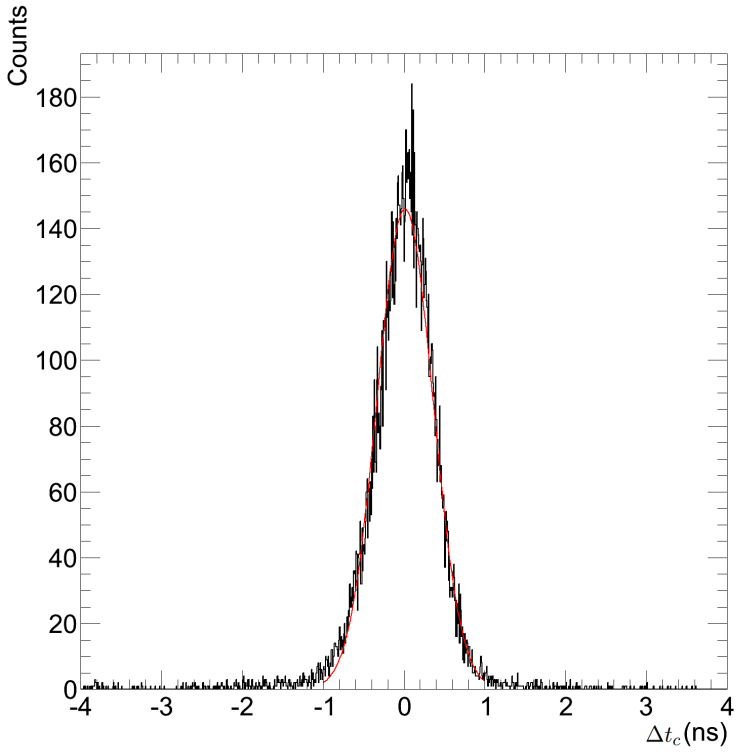

Figure 3.11 An example of the fitting in one momentum slice for the complex Δt_c selection cut. It shows the gaussian fit of the Δt_c distribution in the momentum range from 1.4 GeV/c to 1.6 GeV/c.

Figure 3.12 shows the integrated Δt_c and Δt_p distributions for various selection criteria: for the raw data, after applying the momentum dependent Δt_p and Δt_c cuts, respectively, and after selecting events with missing-mass-squares in the $\gamma p \to pX$

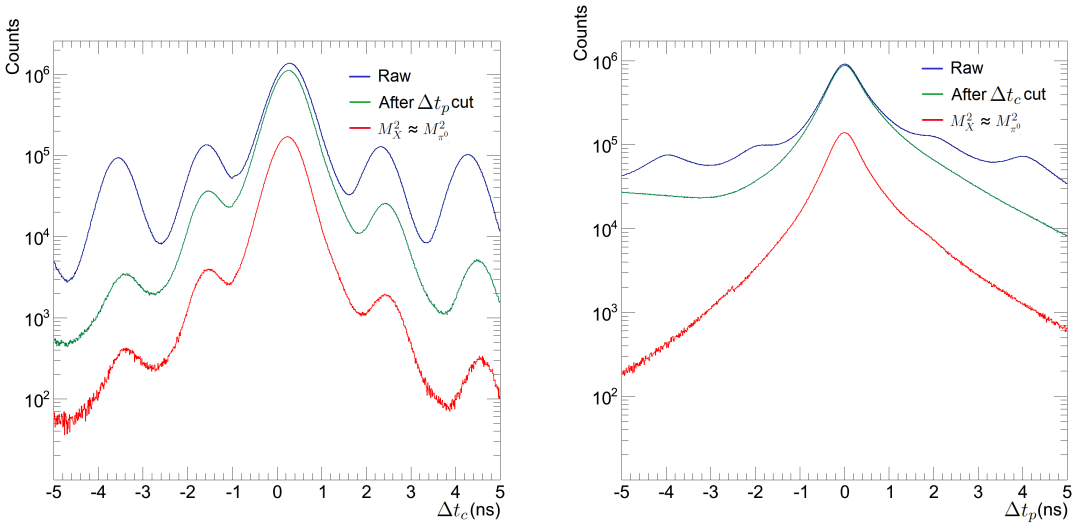

Figure 3.12 The left panel shows the CLAS-tagger coincidence time distribution for various selection criteria. The right panel shows the time distribution of proton candidates for various selection criteria.

reaction close to $M_{\pi^0}^2$. After the reaction-channel selection with a missing mass cut, the background from random coincidences appears to be less than 2% based on the yields in the true and random coincidence peaks. Proton misidentification appears to be negligible.

3.4 Corrections

The standard eloss package [47] was utilized to determine from the measured momentum the momentum of the protons at the reaction vertex in the target. The correction accounts for energy losses in the target material, target wall, carbon cylinder, and start counter. Additionally, momentum corrections were applied to the detected protons following the procedure of CLAS Note 2013-011, "Momentum corrections for π^+ and protons in g9b data" [49]. These momentum corrections make an attempt to correct errors in the momentum determination that may be caused by drift-chamber misalignments and uncertainties in the magnetic field-map.

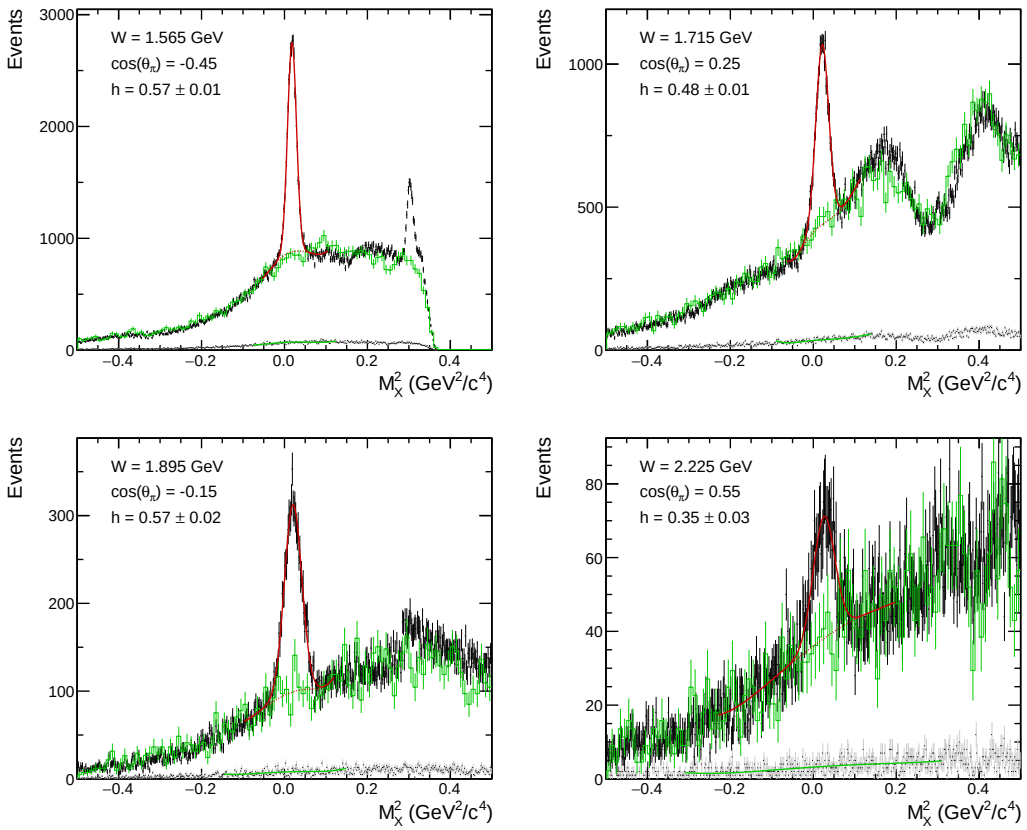

Figure 3.13 Examples of missing-mass-squared distributions from butanol-target (black histograms) and carbon-target data (gray histograms). The solid red and green curves are fits to the butanol and carbon data, respectively. The scaled carbon-data fit is shown as red dashed curve and the scaled carbon distribution as green histogram. Also indicated are the dilution factors h.

3.5 Channel Identification

The channel identification process was based on individual kinematic bins. The data were binned in W from 1.49 GeV to 2.51 GeV with a bin size of 0.03 GeV and in cosine of the center-of-mass angle, $\cos\theta_\pi^{cm}$, from -1 to 1 with a bin size of 0.1. The missing-mass-squared distributions in the $\gamma p \to pX$ reaction from both butanol and carbon targets were accumulated for each bin. Figure 3.13 shows four examples of missing-mass distributions for various energy and angular bins.

The black histograms show data from the butanol target and the gray histograms, with much smaller statistics, show data from the carbon target. The central peaks

at $M_X^2 = m_{\pi^0}^2 \approx 0.018$ GeV$^2/c^4$ above a broad background correspond to events from the $\gamma p \to \pi^0 p$ reaction off free protons in the butanol target. To determine the bound-nucleon background in the missing-mass-squared distributions from the butanol target, a composite fit was applied to each distribution. For each bin, the carbon-target distribution was described with a cubic spline $p_3(x)$ with four nodes and the butanol-target distribution was described by the same spline function multiplied by a scale factor for the bound-nucleon background and a gaussian function for the free-proton events of the expected reaction channel. The fit functions that described the signal, $S(x)$, the carbon-target, $C(x)$, and the butanol-target, $B(x)$, distributions are

$$S(x) = Y_0 \exp\left(-\frac{(x - M_0^2)^2}{2\sigma^2}\right), \tag{3.5}$$

$$C(x) = p_3(x; x_1, y_1, x_2, y_2, x_3, y_3, x_4, y_4, b_2, e_2), \quad \text{and} \tag{3.6}$$

$$B(x) = \kappa C(x) + S(x). \tag{3.7}$$

The signal parameters Y_0, M_0^2, and σ, the parameters of the spline function x_i, y_i, and the second derivative at the first and last nodes, b_2 and e_2, respectively, as well as the scale factor κ were determined by simultaneous fits to the carbon and butanol distributions. The quantity

$$\chi^2_{\text{MLE}} = 2\Big[\sum_i [B(M_i^2) - N_i^B \cdot \log B(M_i^2)] + \sum_j [C(M_i^2) - N_j^C \cdot \log C(M_j^2)]\Big] \tag{3.8}$$

was minimized in the fits. It is the sum of the negative logarithm of the likelihood function for Poisson-distributed butanol and carbon data. Those functions introduce the least bias in the estimation of the parameters [50]. The first sum in Eq. (3.8) runs over all bins in the butanol missing-mass-squared distribution within a specified fit range, listed in Table 3.5, and the second sum runs similarly over bins in the carbon-data histograms. N_k^B and N_k^C are the number of events in the bins of the butanol and carbon histogram at a missing-mass-squared M_k^2. The minimization of Eq. (3.8) was coded with the Minuit2 [51] package from CERN.

Table 3.5 Missing-mass-squared ranges used for fits to the distributions from butanol and carbon targets at the given energies. The ranges for other values of W are interpolated or taken as the range of the lowest (for $W < 1.5$ GeV) or highest (for $W > 2.4$ GeV) of the ranges given in the table.

W (GeV)	Butanol range (GeV^2/c^4)	Carbon range (GeV^2/c^4)
1.5	-0.05 to 0.10	-0.07 to 0.12
1.8	-0.07 to 0.12	-0.10 to 0.15
1.9	-0.10 to 0.12	-0.15 to 0.15
2.0	-0.10 to 0.15	-0.15 to 0.20
2.2	-0.15 to 0.20	-0.30 to 0.30
2.4	-0.25 to 0.20	-0.40 to 0.40

The respective fit ranges were chosen to ensure the coverage of the whole π_0 peak in the missing-mass-squared distribution and to keep away from structures of other reaction channels. The carbon-target distribution is more featureless and a wider fit range was chosen to better constrain the fit with these low-statistics data. As the width of the π_0 peak increases with W, the fit ranges are also increasing. Examples of fit results are shown in Fig. 3.13. The gross fit functions are shown as solid red curves and the scaled spline background functions are shown as dashed red curves.

After obtaining the butanol missing-mass-squared distribution and the polynomial background for each kinematic bin butanol-target events were selected that satisfy the $\gamma p \to \pi^0 p$ kinematics for further analysis. The selection was based on the condition

$$|M_X^2 - M_0^2| < n\sigma_H, \tag{3.9}$$

where M_0^2 and σ_H were taken from the fit parameter in Eq. (3.5). For those events, normalized polarized yields and dilution factors were calculated. The dilution factor is the ratio between the number of free proton events and the total number of events. Experimentally, the dilution factor was obtained as

$$h = \frac{N^B - \kappa \int C(M^2) dM^2}{N^B}, \tag{3.10}$$

where N^B is the number of selected butanol-target events and the integral is of the spline background, Eq. (3.6), over the missing-mass-squared range that satisfies the $\gamma p \to \pi^0 p$ kinematics in the specific kinematic bin. The dilution factor varies as the missing-mass-squared resolution and background contributions change with energy and angle. Dilution factors are given in Figure 3.13. For the determination of n in Eq. (3.9), a balance needs to be found between the statistical uncertainty from the number of events and the magnitude of the dilution factor. In this analysis $n = 2$ has been used for the calculation of the results as this value brings most (95%) events into the calculation and retains a large fraction of the dilution factor relative to the largest possible dilution factor of the same bin.

Figure 3.14 shows the distribution of dilution factors for various data-range selections, $|M_X^2 - M_0^2| < n\sigma_H$. The selections of $n = 1$, 2, and 3 are shown with three different colors. The dilution factor distribution for each width of selection is generally smooth. As expected, tighter cuts on the free-proton signal lead to increased dilution factors. Systematic uncertainties related to the background correction with dilution factors have been estimated from consistency tests of the extracted polarization for various choices of data range; see Sec. 3.7.

3.6 Moments of Yields

The polarization observables T and F for a specific center-of-mass energy, W, and a specific cosine of the center-of-mass angle, $\cos\theta_\pi^{cm}$, can be extracted from normalized moments of the measured events in the associated W and $\cos\theta_\pi^{cm}$ bin. From the expression of the polarized cross section, Eq. (1.6), the integrated normalized polarized yield of a specific bin can be expressed as

$$Y = \frac{1}{2\pi}\int_0^{2\pi} Y_{unpol} A(\varphi)(1 + P_T T \sin\varphi + P_T P_\odot F \cos\varphi) d\varphi, \tag{3.11}$$

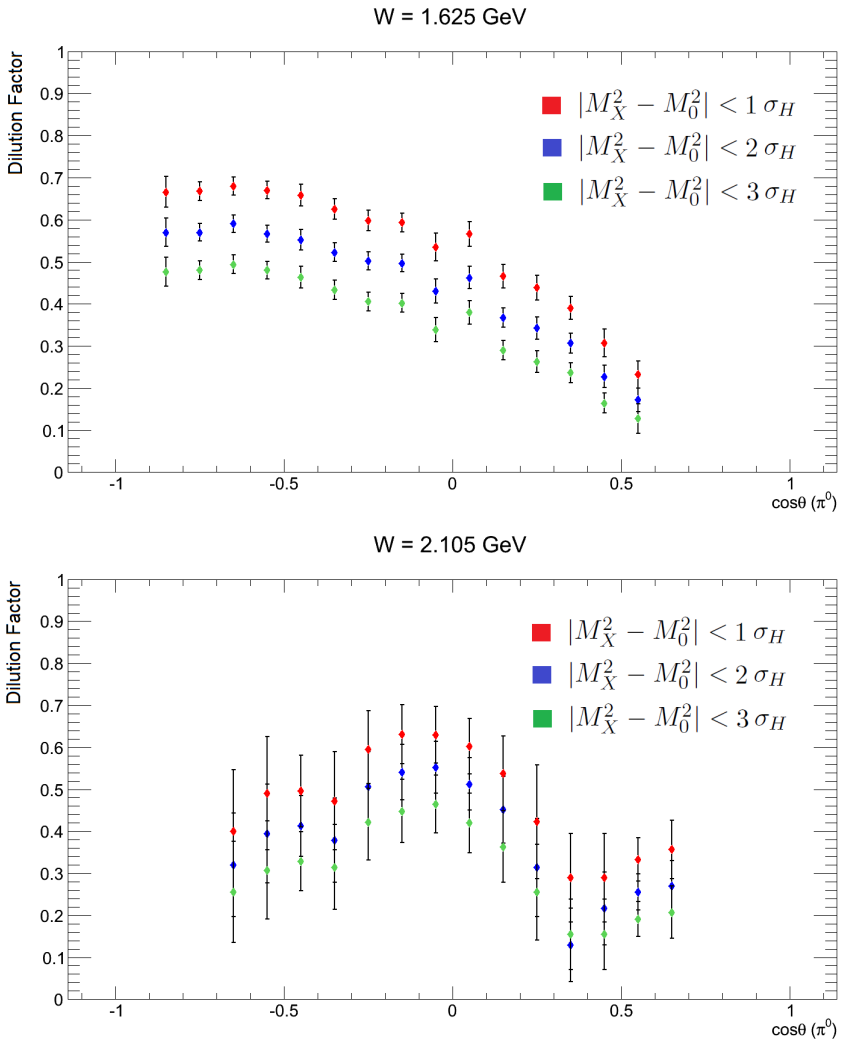

Figure 3.14 Examples of the dilution distribution for various data-range selections. The selections of $n = 1$ are shown in red. The selections of $n = 2$ are shown in blue. The selections of $n = 3$ are shown in green. The dilution distribution for each width of selection is generally smooth. In this analysis $n = 2$ has been used for the calculation of the results.

where Y_{unpol} is proportional to the unpolarized cross section and $A(\varphi)$ is the average acceptance of the detector in the bin of interest. Additionally, the $\sin m\varphi$ and the $\cos m\varphi$ moments are defined as

$$Y_{\sin m\varphi} = \frac{1}{2\pi}\int_0^{2\pi} Y_{unpol} A(\varphi)(1 + P_T T \sin\varphi + P_T P_\odot F \cos\varphi)\sin m\varphi d\varphi \quad \text{and} \quad (3.12)$$

$$Y_{\cos m\varphi} = \frac{1}{2\pi}\int_0^{2\pi} Y_{unpol} A(\varphi)(1 + P_T T \sin\varphi + P_T P_\odot F \cos\varphi)\cos m\varphi d\varphi. \quad (3.13)$$

Since there are four combinations of two target-polarization directions and two photon-beam helicities, each of the normalized yields or moments can be categorized into four groups. In this analysis $+/-$ stands for the photon beam helicity and $\leftarrow/\rightarrow$ for the target polarization direction. Experimentally, the normalized moments are obtained for each kinematic bin as

$$Y = \frac{\sum_i(1)}{N}, \tag{3.14}$$

$$Y_{\sin m\varphi} = \frac{\sum_i(\sin m\varphi_i)}{N}, \quad \text{and} \tag{3.15}$$

$$Y_{\cos m\varphi} = \frac{\sum_i(\cos m\varphi_i)}{N}, \tag{3.16}$$

where the sums are taken over the butanol-target events that satisfy the $\gamma p \to \pi^0 p$ kinematics. A relative normalization of the sums is given by the number of carbon-target events N from the respective setting, which is proportional to the luminosity. An overall absolute normalization cancels in the final expressions for the observables and can be safely neglected.

With the dilution factor, the normalized yields or moments of the free-proton can be obtained from those of butanol:

$$Y^p = hY, \tag{3.17}$$

$$Y^{p\rightarrow}_{\cos 2\varphi} + Y^{p\leftarrow}_{\cos 2\varphi} = h(Y^{\rightarrow}_{\cos 2\varphi} + Y^{\leftarrow}_{\cos 2\varphi}). \tag{3.18}$$

However, the differences of the $\sin\varphi$ and the $\cos\varphi$ moments between different combinations of target or beam polarizations come only from the free-proton events and are not diluted:

$$Y^{p\rightarrow+}_{\sin\varphi} + Y^{p\rightarrow-}_{\sin\varphi} - Y^{p\leftarrow+}_{\sin\varphi} - Y^{p\leftarrow-}_{\sin\varphi} = Y^{\rightarrow+}_{\sin\varphi} + Y^{\rightarrow-}_{\sin\varphi} - Y^{\leftarrow+}_{\sin\varphi} - Y^{\leftarrow-}_{\sin\varphi}, \tag{3.19}$$

$$Y^{p\rightarrow+}_{\cos\varphi} - Y^{p\rightarrow-}_{\cos\varphi} - Y^{p\leftarrow+}_{\cos\varphi} + Y^{p\leftarrow-}_{\cos\varphi} = Y^{\rightarrow+}_{\cos\varphi} - Y^{\rightarrow-}_{\cos\varphi} - Y^{\leftarrow+}_{\cos\varphi} + Y^{\leftarrow-}_{\cos\varphi}. \tag{3.20}$$

3.7 Acceptance and Observable Extraction

Limited detector acceptances can lead to instrumental asymmetries. Instrumental asymmetries are measured and corrected for with the moments method if the acceptance is constant over the run time. The acceptance $A(\varphi)$ was assumed to remain constant during the experiment and can be expanded in a Fourier series,

$$A(\varphi) = a_0 + \sum_{n=1}^{+\infty}(a_n \cos n\varphi + b_n \sin n\varphi). \tag{3.21}$$

The differences of the normalized moments between different combinations of target or beam polarizations can be expressed as

$$Y^{\rightarrow}_{\sin\varphi} - Y^{\leftarrow}_{\sin\varphi} = \frac{1}{2} Y_{unpol}(P^{\rightarrow}_T + P^{\leftarrow}_T)(a_0 - a_2)T \tag{3.22}$$

and

$$Y^{\rightarrow +}_{\cos\varphi} - Y^{\rightarrow -}_{\cos\varphi} - Y^{\leftarrow +}_{\cos\varphi} + Y^{\leftarrow -}_{\cos\varphi} = \frac{1}{2} Y_{unpol} P_{\odot}(P^{\rightarrow}_T + P^{\leftarrow}_T)(a_0 + a_2)F. \tag{3.23}$$

The terms with Fourier coefficients $Y_{unpol}a_0$ and $Y_{unpol}a_2$ can be obtained from

$$P^{\leftarrow}_T Y^{\rightarrow} + P^{\rightarrow}_T Y^{\leftarrow} = Y_{unpol}(P^{\rightarrow}_T + P^{\leftarrow}_T)a_0 \tag{3.24}$$

and

$$P^{\leftarrow}_T Y^{\rightarrow}_{\cos 2\varphi} + P^{\rightarrow}_T Y^{\leftarrow}_{\cos 2\varphi} = Y_{unpol}(P^{\rightarrow}_T + P^{\leftarrow}_T)a_2. \tag{3.25}$$

By utilizing different combinations of target or beam polarizations, after determining the acceptance effect, the polarization observables T and F can be obtained as

$$T = \frac{1}{h} \frac{2(Y^{\rightarrow}_{\sin\varphi} - Y^{\leftarrow}_{\sin\varphi})}{P^{\leftarrow}_T(Y^{\rightarrow} - Y^{\rightarrow}_{\cos 2\varphi}) + P^{\rightarrow}_T(Y^{\leftarrow} - Y^{\leftarrow}_{\cos 2\varphi})} \tag{3.26}$$

and

$$F = \frac{1}{h} \frac{2(Y^{\rightarrow +}_{\cos\varphi} - Y^{\rightarrow -}_{\cos\varphi} - Y^{\leftarrow +}_{\cos\varphi} + Y^{\leftarrow -}_{\cos\varphi})}{P_{\odot}P^{\leftarrow}_T(Y^{\rightarrow} + Y^{\rightarrow}_{\cos 2\varphi}) + P_{\odot}P^{\rightarrow}_T(Y^{\leftarrow} + Y^{\leftarrow}_{\cos 2\varphi})}. \tag{3.27}$$

Both of the expressions for the observables have the form of $\frac{u}{hv}$. The variance of $\frac{u}{hv}$ can be expressed as

$$Var\left(\frac{u}{hv}\right) = \frac{u^2}{h^2v^2}\left(\frac{\sigma_h^2}{h^2} + \frac{\sigma_u^2}{u^2} + \frac{\sigma_v^2}{v^2} - \frac{Cov(uv)}{uv}\right). \tag{3.28}$$

For the statistical uncertainty of the observable T this means

$$u = 2(Y^{\rightarrow}_{\sin\varphi} - Y^{\leftarrow}_{\sin\varphi}) \quad \text{and} \tag{3.29}$$

$$v = P_T^{\leftarrow}(Y^{\rightarrow} - Y^{\rightarrow}_{\cos 2\varphi}) + P_T^{\rightarrow}(Y^{\leftarrow} - Y^{\leftarrow}_{\cos 2\varphi}). \tag{3.30}$$

It follows then, that

$$\sigma_u^2 = \frac{2}{N^{\rightarrow}}(Y^{\rightarrow} - Y^{\rightarrow}_{\cos 2\varphi}) + \frac{2}{N^{\leftarrow}}(Y^{\leftarrow} - Y^{\leftarrow}_{\cos 2\varphi}), \tag{3.31}$$

$$\sigma_v^2 = \frac{P_T^{\leftarrow 2}}{2N^{\rightarrow}}(3Y^{\rightarrow} - 4Y^{\rightarrow}_{\cos 2\varphi} + Y^{\rightarrow}_{\cos 4\varphi}) + \frac{P_T^{\rightarrow 2}}{2N^{\leftarrow}}(3Y^{\leftarrow} - 4Y^{\leftarrow}_{\cos 2\varphi} + Y^{\leftarrow}_{\cos 4\varphi}), \tag{3.32}$$

and

$$Cov(uv) = \frac{P_T^{\leftarrow}}{N^{\rightarrow}}(3Y^{\rightarrow}_{\sin\varphi} - Y^{\rightarrow}_{\sin 3\varphi}) - \frac{P_T^{\rightarrow}}{N^{\leftarrow}}(3Y^{\leftarrow}_{\sin\varphi} - Y^{\leftarrow}_{\sin 3\varphi}). \tag{3.33}$$

For the statistical uncertainty of the observable F, we find

$$u = 2(Y^{\rightarrow +}_{\cos\varphi} - Y^{\rightarrow -}_{\cos\varphi} - Y^{\leftarrow +}_{\cos\varphi} + Y^{\leftarrow -}_{\cos\varphi}) \quad \text{and} \tag{3.34}$$

$$v = P_{\odot}P_T^{\leftarrow}(Y^{\rightarrow} + Y^{\rightarrow}_{\cos 2\varphi}) + P_{\odot}P_T^{\rightarrow}(Y^{\leftarrow} + Y^{\leftarrow}_{\cos 2\varphi}), \tag{3.35}$$

and consequently

$$\sigma_u^2 = \frac{2}{N^{\rightarrow}}(Y^{\rightarrow} + Y^{\rightarrow}_{\cos 2\varphi}) + \frac{2}{N^{\leftarrow}}(Y^{\leftarrow} + Y^{\leftarrow}_{\cos 2\varphi}), \tag{3.36}$$

$$\sigma_v^2 = \frac{P_{\odot}^2 P_T^{\leftarrow 2}}{2N^{\rightarrow}}(3Y^{\rightarrow} + 4Y^{\rightarrow}_{\cos 2\varphi} + Y^{\rightarrow}_{\cos 4\varphi}) + \frac{P_{\odot}^2 P_T^{\rightarrow 2}}{2N^{\leftarrow}}(3Y^{\leftarrow} + 4Y^{\leftarrow}_{\cos 2\varphi} + Y^{\leftarrow}_{\cos 4\varphi}), \tag{3.37}$$

$$\begin{aligned} Cov(uv) = {} & \frac{P_{\odot}P_T^{\leftarrow}}{N^{\rightarrow}}(3Y^{\rightarrow +}_{\cos\varphi} - 3Y^{\rightarrow -}_{\cos\varphi} + Y^{\rightarrow +}_{\cos 3\varphi} - Y^{\rightarrow -}_{\cos 3\varphi}) \\ & - \frac{P_{\odot}P_T^{\rightarrow}}{N^{\leftarrow}}(3Y^{\leftarrow +}_{\cos\varphi} - 3Y^{\leftarrow -}_{\cos\varphi} + Y^{\leftarrow +}_{\cos 3\varphi} - Y^{\leftarrow -}_{\cos 3\varphi}). \end{aligned} \tag{3.38}$$

It has been observed that the extracted observables depend on the data-range selection, Eq. (3.9). To estimate associated systematic effects, comparisons of the differences between observables from ranges of selection with $n = 1$, 2, and 3 were made. Figure 3.15 shows the distributions of those differences for analyses with $n = 1$ and 2 as red histograms as well as $n = 2$ and 3 as green histograms. Systematic shifts of the peaks are observed for both observables T (left panel) and F (right panel). The mean of gaussian fits to the differences acts as an indicator of the systematic effects and has been listed in Table 3.6. For the observables T and F, the systematic uncertainties based on the larger differences are 0.010 and 0.013, respectively.

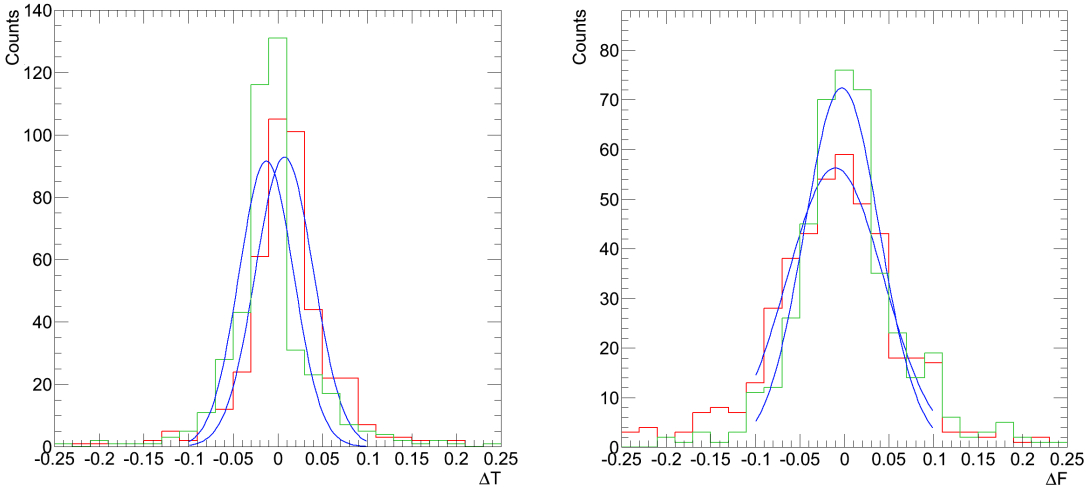

Figure 3.15 Distribution of the differences between observables under two consecutive data-range selections for observable T (left panel) and F (right panel). The distributions of differences between integration range $\pm 1\sigma_H$ and $\pm 2\sigma_H$ are drawn in red and the distributions of differences between integration range $\pm 2\sigma_H$ and $\pm 3\sigma_H$ are drawn in green. The gaussian fits to the distributions are drawn in blue. Systematic shifts between the peaks are observed in both distributions.

The average detector acceptance changed over the run time for the runs with circularly polarized photons used in the analysis. As discussed before, the average acceptance was assumed to remain constant between run groups in moment-method analysis. In the case of the observable F, this condition was automatically fulfilled

Table 3.6 Mean value of differences in extracted observables from various missing-mass-squared ranges. For the observables T and F, the systematic uncertainties based on the larger ones out of two sets of differences are 0.010 and 0.013, respectively.

Integration Range	ΔT	ΔF
Between $\pm 1\sigma_H$ and $\pm 2\sigma_H$	0.008	0.010
Between $\pm 2\sigma_H$ and $\pm 3\sigma_H$	0.013	0.003

as the beam helicity flipped rapidly to ensure the same average acceptance for both helicity states. In the case of the observable T, since the target polarization was flipped run group by run group, the acceptance was not guaranteed to remain the same for all run groups. In fact, in a further study we have determined the Fourier coefficients of the acceptance, Eq. (3.21), using carbon-target events. As these events are unpolarized, any non-zero value of b_1 indicates an instrumental asymmetry due to a limited detector acceptance, which would affect the extraction of observable T. The instrumental asymmetry could be due to changes of the average acceptance caused by detector problems or by effects associated with the different holding-field orientations. The study showed that the coefficient b_1/a_0 changed significantly between run groups 3 and 4, Fig. 3.16, but remained approximately constant otherwise. To account for that change in $A(\varphi)$, the whole data set has been divided into two parts, run group 1 to 3 and 4 to 5, to ensure the constancy of the acceptance in each part. Results of observable T were extracted from these two parts separately. The two results were found to be consistent. The final results were taken as the uncertainty-weighted average ot the two. Furthermore, for the remaining differences within each part, the Fourier coefficients indicate a 0.015 systematic uncertainty estimated as the standard deviation of the raw asymmetry in each of the two parts divided by the average target polarization and the dilution factors.

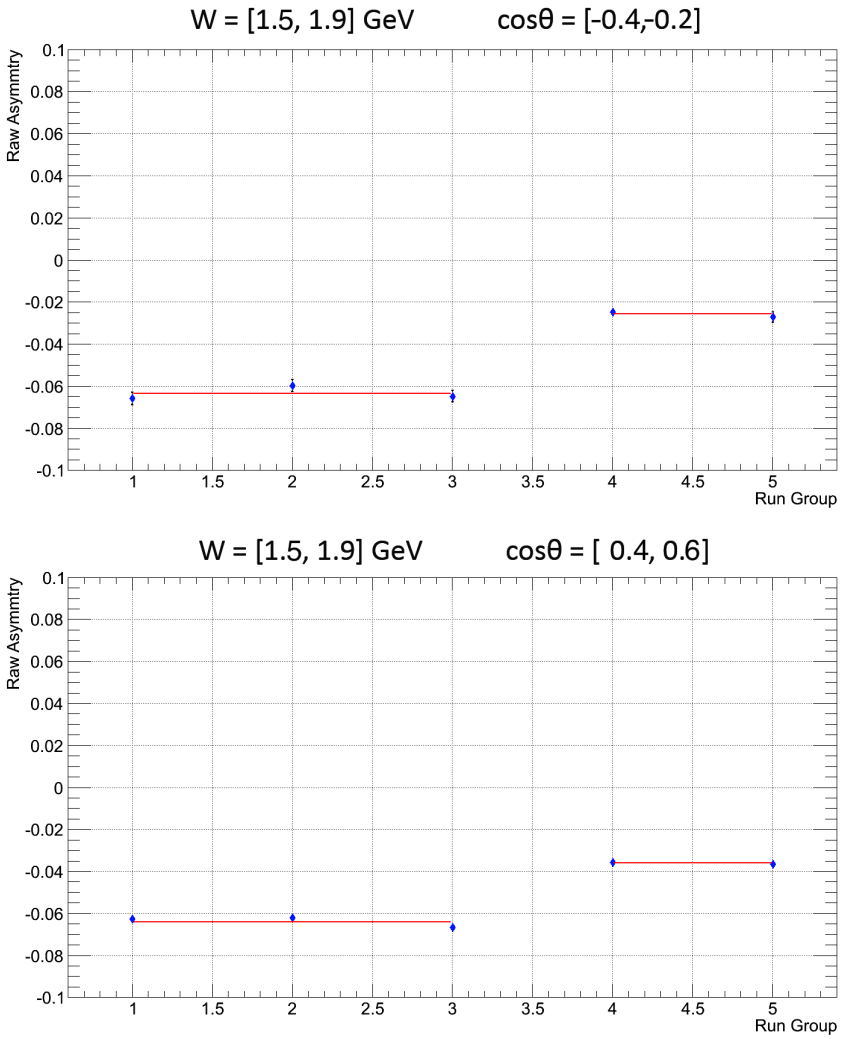

Figure 3.16 Examples of the coefficient b_1/a_0 for two different kinematic bins. The blue data points represent the coefficients b_1/a_0 for each run group. The red lines are horizontal fits of data points in two parts. A significant change of the coefficients has been found between run groups 3 and 4.

3.8 Target-Polarization Orientation

Using Eq. (3.2), the polarized cross section can be expressed as

$$\frac{d\sigma}{d\Omega} = \frac{d\sigma}{d\Omega}_{\text{unpol}} \left(1 + P_T T \sin(\varphi_0 - \varphi_\pi^{\text{lab}}) + P_T P_\odot F \cos(\varphi_0 - \varphi_\pi^{\text{lab}})\right) . \tag{3.39}$$

To ensure that the results are not affected by the acceptance changes among run groups, the helicity-dependent part of the polarized yield was utilized to calculate φ_0, based on the term $P_T P_\odot F \cos(\varphi_0 - \varphi_\pi^{\text{lab}})$. The integrated normalized polarized yield

can be expressed as

$$Y = \frac{1}{2\pi}\int_0^{2\pi} Y_{unpol} A(\varphi_\pi^{\rm lab}) \Big(1 + P_T T(\sin\varphi_0 \cos\varphi_\pi^{\rm lab} - \cos\varphi_0 \sin\varphi_\pi^{\rm lab}) + P_T P_\odot F(\cos\varphi_0 \cos\varphi_\pi^{\rm lab} + \sin\varphi_0 \sin\varphi_\pi^{\rm lab})\Big)\, d\varphi_\pi^{\rm lab}, \quad (3.40)$$

where $A(\varphi_\pi^{\rm lab})$ is the average acceptance in the lab frame. The $\sin m\varphi_\pi^{\rm lab}$ and the $\cos m\varphi_\pi^{\rm lab}$ moments can be expressed in a similar way as discussed in Sec. 3.6. After the cancellation of $A(\varphi_\pi^{\rm lab})$ and observables T and F by utilizing the $\sin m\varphi_\pi^{\rm lab}$ and the $\cos m\varphi_\pi^{\rm lab}$ moments and the integrated normalized polarized yields, the target orientation in the lab frame, φ_0, can be expressed as

$$\tan\varphi_0 = \frac{(P_T^{\rightarrow} Y^{\leftarrow}_{\sin 2\varphi_\pi^{\rm lab}} + P_T^{\leftarrow} Y^{\rightarrow}_{\sin 2\varphi_\pi^{\rm lab}})r - P_T^{\rightarrow}(Y^{\leftarrow} + Y^{\leftarrow}_{\cos 2\varphi_\pi^{\rm lab}})q - P_T^{\leftarrow}(Y^{\rightarrow} + Y^{\rightarrow}_{\cos 2\varphi_\pi^{\rm lab}})q}{(P_T^{\rightarrow} Y^{\leftarrow}_{\sin 2\varphi_\pi^{\rm lab}} + P_T^{\leftarrow} Y^{\rightarrow}_{\sin 2\varphi_\pi^{\rm lab}})q - P_T^{\rightarrow}(Y^{\leftarrow} - Y^{\leftarrow}_{\cos 2\varphi_\pi^{\rm lab}})r - P_T^{\leftarrow}(Y^{\rightarrow} - Y^{\rightarrow}_{\cos 2\varphi_\pi^{\rm lab}})r}, \quad (3.41)$$

where

$$q = Y^{\rightarrow +}_{\sin\varphi_\pi^{\rm lab}} - Y^{\rightarrow -}_{\sin\varphi_\pi^{\rm lab}} - Y^{\leftarrow +}_{\sin\varphi_\pi^{\rm lab}} + Y^{\leftarrow -}_{\sin\varphi_\pi^{\rm lab}} \quad \text{and} \quad (3.42)$$

$$r = Y^{\rightarrow +}_{\cos\varphi_\pi^{\rm lab}} - Y^{\rightarrow -}_{\cos\varphi_\pi^{\rm lab}} - Y^{\leftarrow +}_{\cos\varphi_\pi^{\rm lab}} + Y^{\leftarrow -}_{\cos\varphi_\pi^{\rm lab}}. \quad (3.43)$$

Equation (3.41) has two solutions for φ_0 between 0° and 360°: $116.3° \pm 1.4°$ and $296.3° \pm 1.4°$. Both values give in the analysis the same magnitudes of the polarization observables T and F, but opposite signs. A comparison of the results with the world data set shows that $\varphi_0 = 116.3° \pm 1.4°$ is the correct solution.

The uncertainty of φ_0, $\delta = 1.4°$, contributes as systematic uncertainty to the polarization observables T and F through

$$\sin(\varphi + \delta) = \sin\varphi\cos\delta + \cos\varphi\sin\delta \quad \text{and} \quad (3.44)$$

$$\cos(\varphi + \delta) = \cos\varphi\cos\delta - \sin\varphi\sin\delta. \quad (3.45)$$

The observable T enters as $T\sin\varphi$ in the polarized cross section and there is no helicity-independent observable connected to $\cos\varphi$. Similarly, the observable F enters

as $F\cos\varphi$ in the polarized cross section and there is no helicity-dependent observable connected to $\sin\varphi$. The effect of a non-zero δ is therefore in either case to dilute the true value of the observables in the reconstruction by a factor of $\cos\delta > 0.999$ that is negligible.

3.9 Systematic Uncertainties

The systematic uncertainties are mainly from beam and target polarizations and the background. Absolute and relative contributions to the systematic uncertainties are listed in Table 3.7.

Table 3.7 Systematic uncertainties for T and F

Item	$\sigma(T)$	$\sigma(F)$	Ref.
Beam-Charge asymmetry	—	0.2%	[43]
Degree of beam polarization	—	3%	3.1
Degree of target polarization	4%	4%	3.1
Target-polarization orientation φ_0	< 0.001	< 0.001	3.8
Accidental background	2%	2%	3.3
Proton misidentification	2%	2%	3.3
Background subtraction	± 0.013	± 0.010	3.7
Run-group acceptance changes	± 0.015	—	3.7
Total	$4.9\% \pm 0.019$	$5.7\% \pm 0.010$	

Chapter 4

Results

4.1 Observable T and F

The results for the polarization observables T and F are shown in Figs. 4.1 through 4.6. The results of this analysis agree with previous measurements in the overlapping energy range. The major difference between the results in this analysis and the results from previous measurements is the difference of the coverage of the energy. In this analysis, the upper limit of W is much larger, up to 2495 MeV, compare to W up to 1895 MeV from the most recent measurements.

The results are compared with solutions from SAID (MA27) [26], BnGa (2014-02) [27], and MAID (2007) [28]. The present SAID, BnGa, and MAID model predictions generally agree with the data in the energy range overlapped with previous measurements but significant deviations are observed, mostly in the range of W above 2100 MeV. This meets the expectation of this analysis which is to constrain the partial-wave analyses and also improved the completeness of the data from the pion-photoproduction experiments.

Table 4.1 summarizes the experimental results. There are 429 available bins, each of which is 30 MeV wide in W and 0.1 wide in $\cos\theta_\pi^{cm}$. The first and the second columns give the average center-of-mass energy W and pion angle $\cos\theta_\pi^{cm}$. The third and the forth columns give the results for the observable T and F including statistical and systematic uncertainties, respectively.

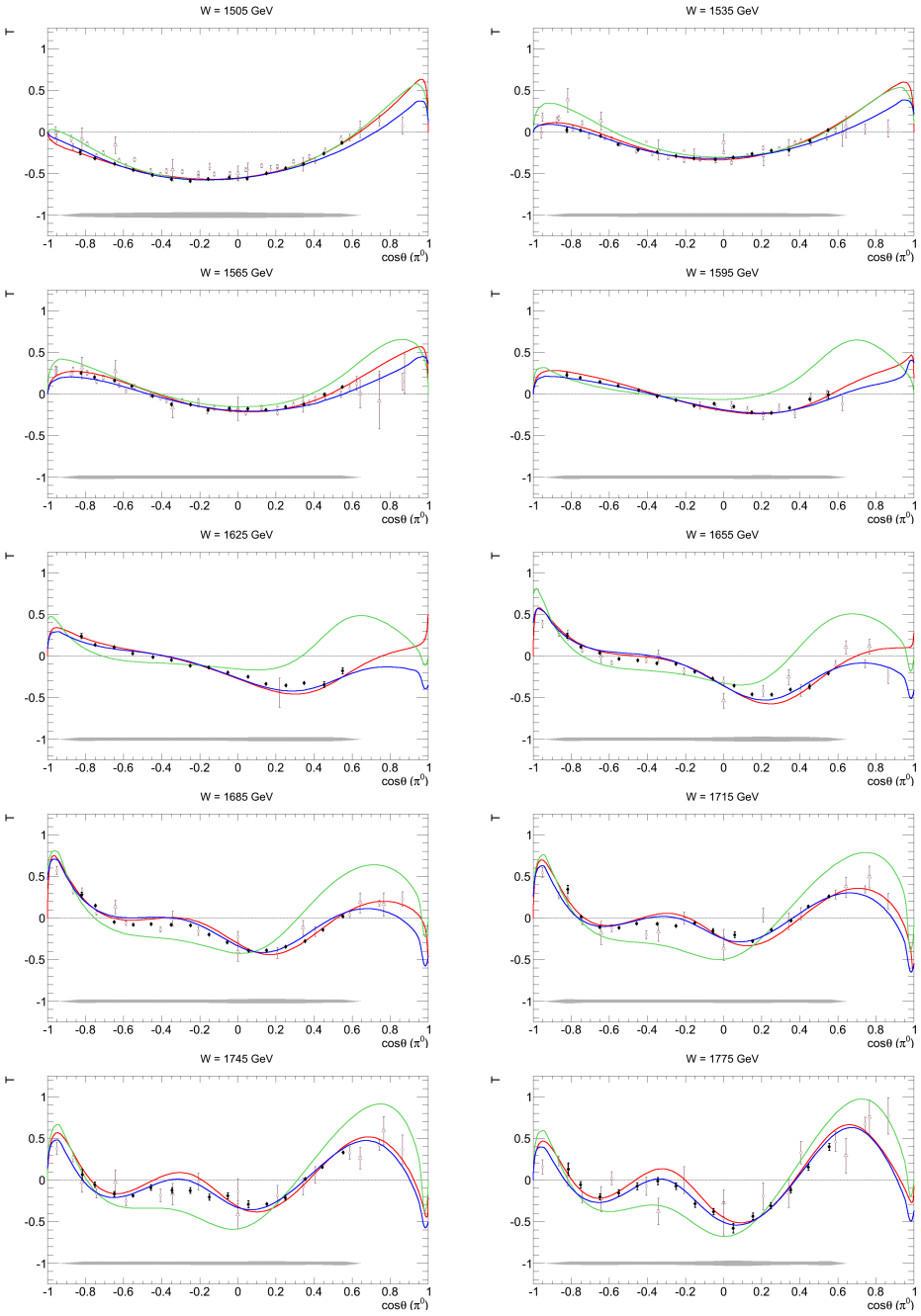

Figure 4.1 Polarization observable T. The results of this analysis are shown in black. The gray band indicates the size of the systematic uncertainties. The SAID (MA27) [26], BnGa (2014-02) [27], and MAID (2007) [28] model predictions are shown in red, blue, and green. Data from other experiments are also shown as circle (MAMI, Mainz [25]), square (CBELSA/TAPS, Bonn [24]), triangle (Institute for Nuclear Study, Tokyo [20, 19]), and star (Daresbury Laboratory [22, 21]).

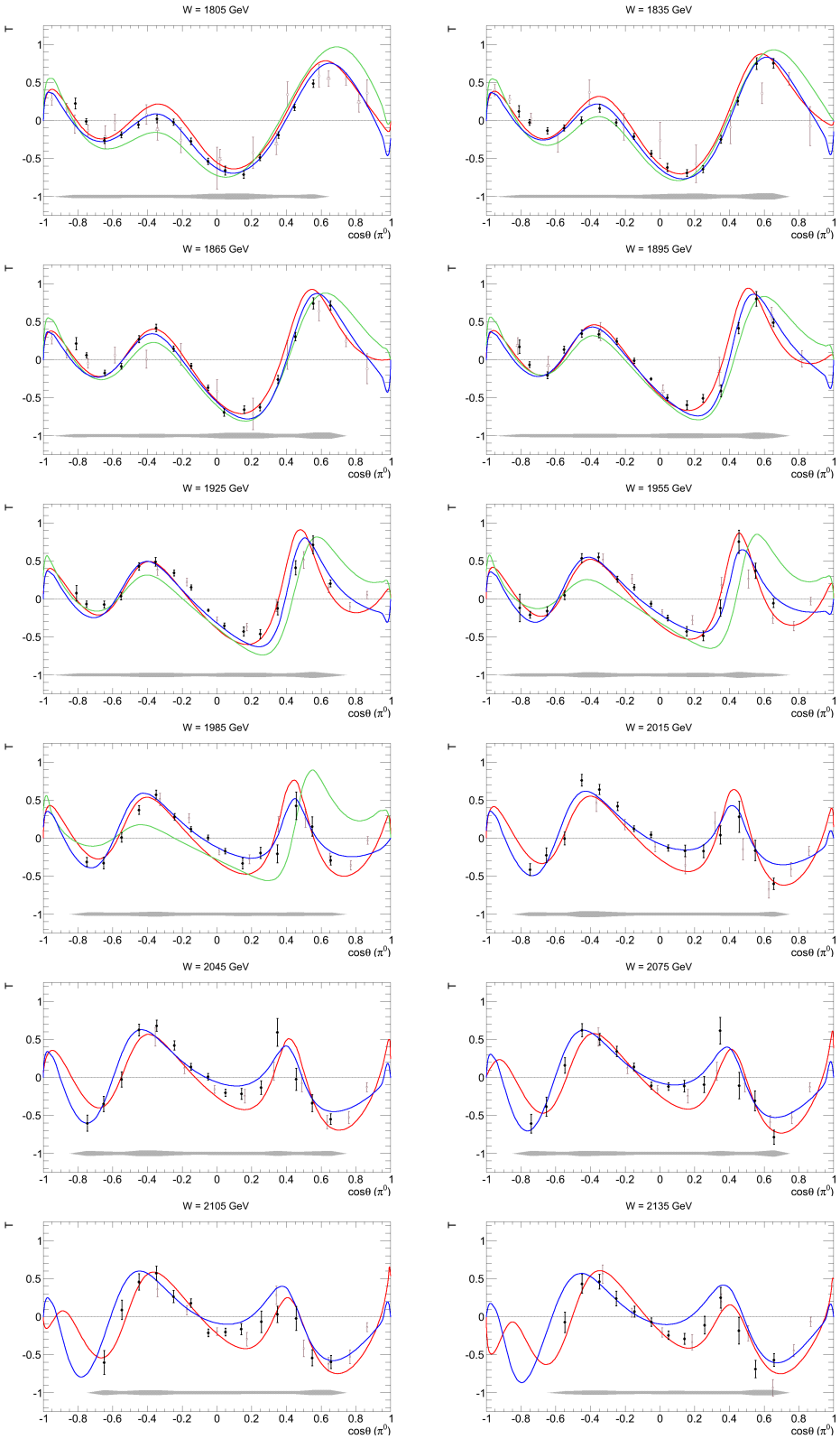

Figure 4.2 Polarization observable T (continued).

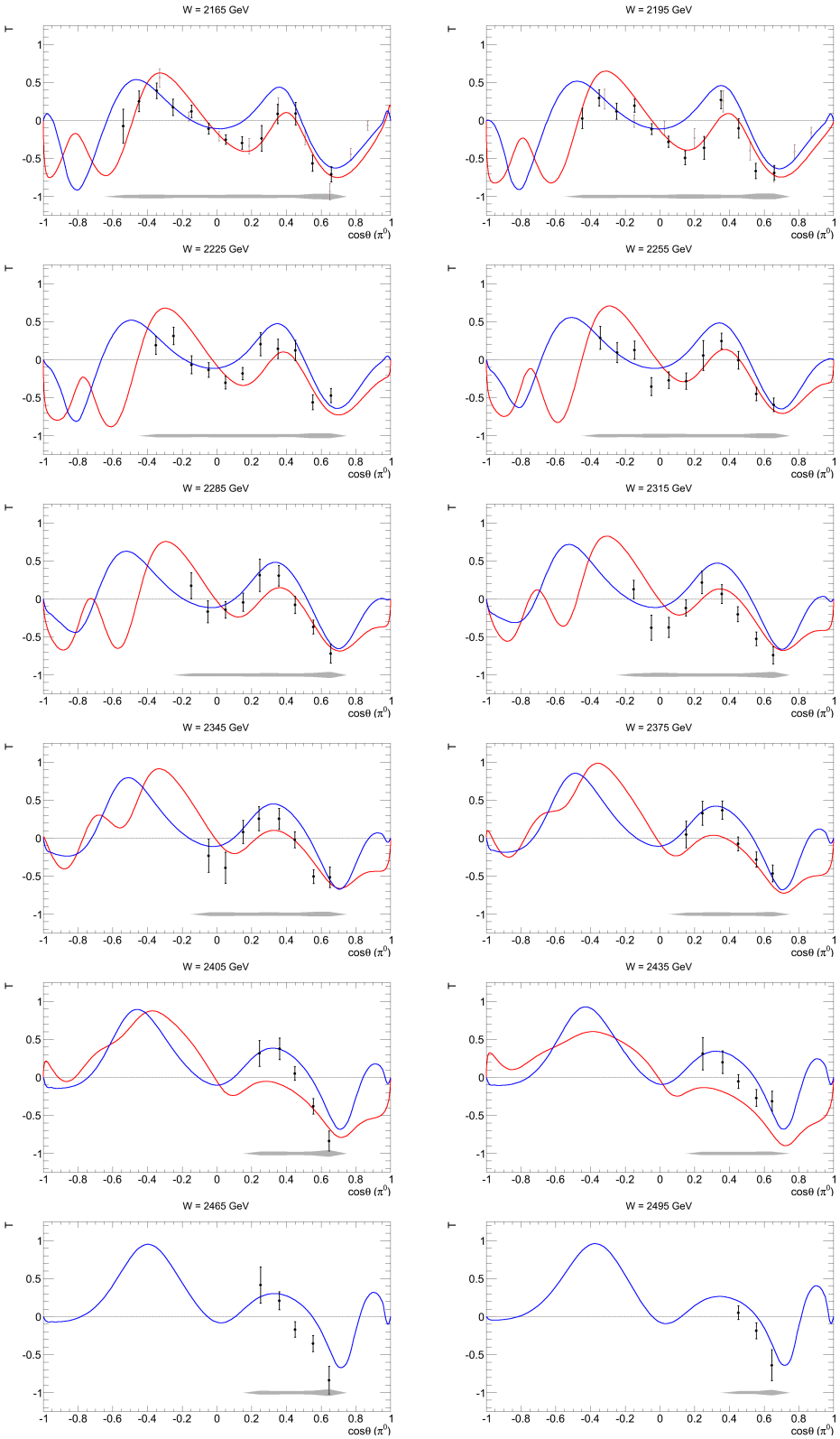

Figure 4.3 Polarization observable T (continued).

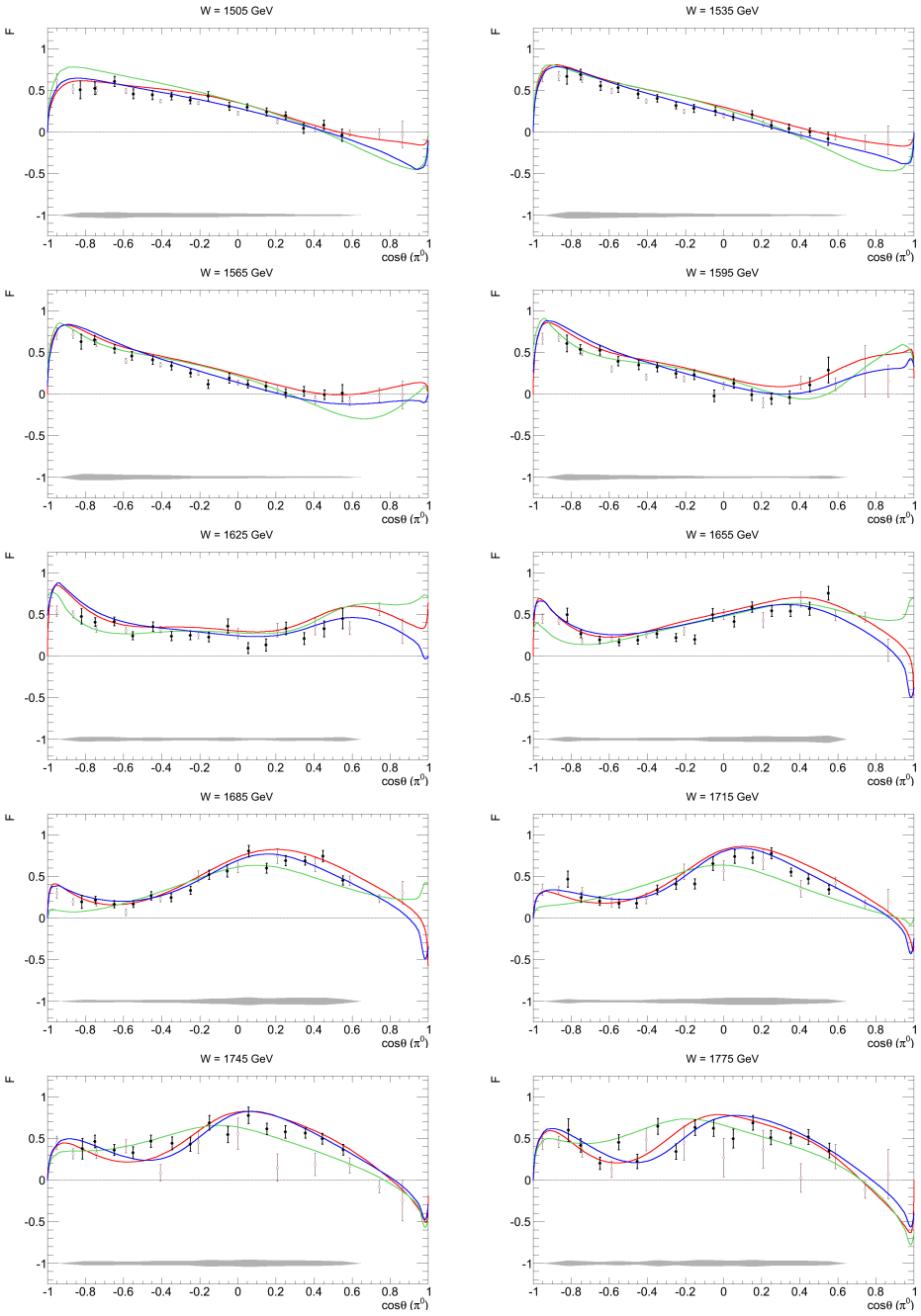

Figure 4.4 Polarization observable F. The results of this analysis are shown in black. The gray band indicates the size of the systematic uncertainties. The SAID (MA27) [26], BnGa (2014-02) [27], and MAID (2007) [28] model predictions are shown in red, blue, and green. Data from other experiments are also shown as circle (MAMI, Mainz [25]), square (CBELSA/TAPS, Bonn [24]), triangle (Institute for Nuclear Study, Tokyo [20, 19]), and star (Daresbury Laboratory [22, 21]).

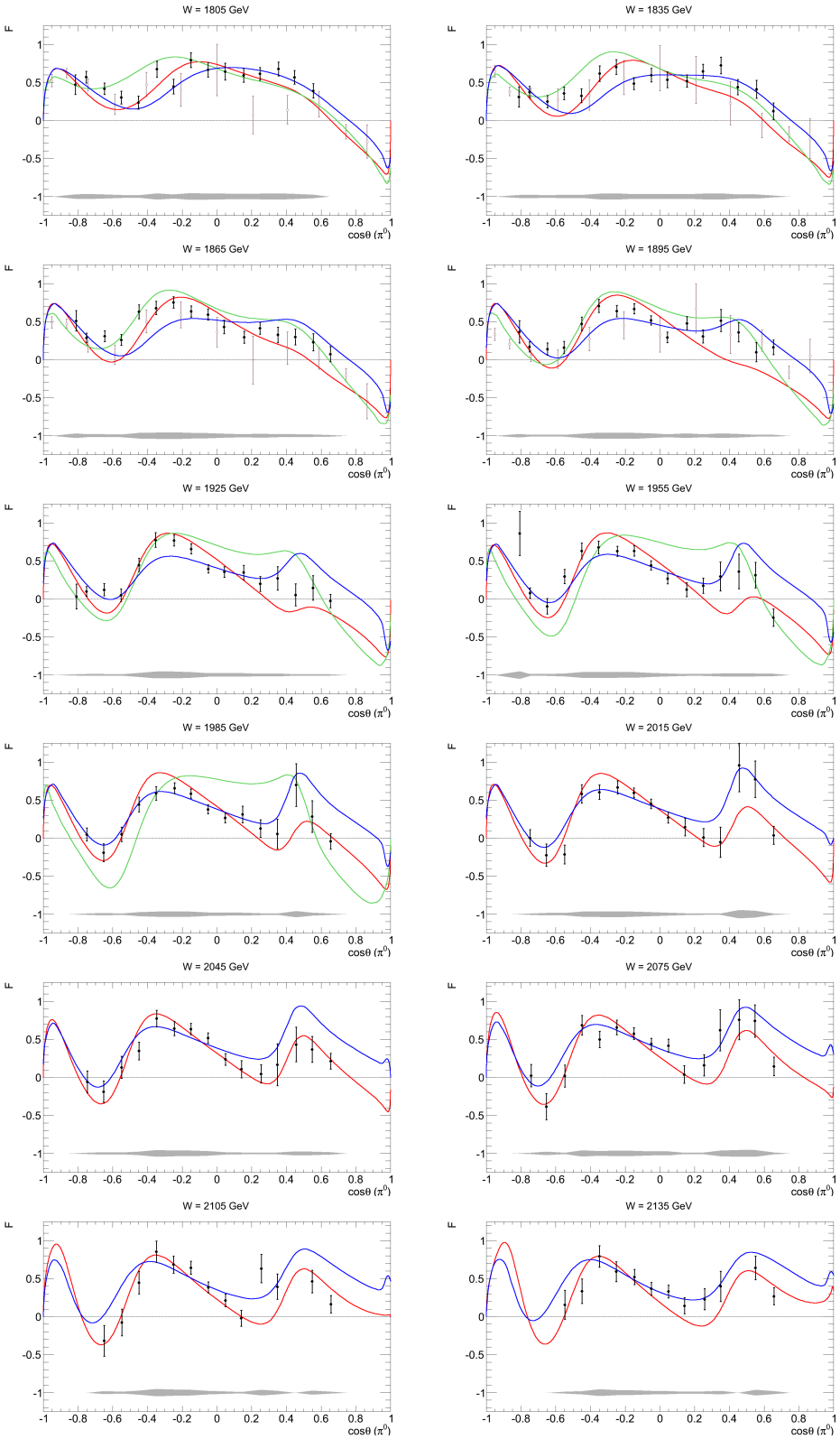

Figure 4.5 Polarization observable F (continued).

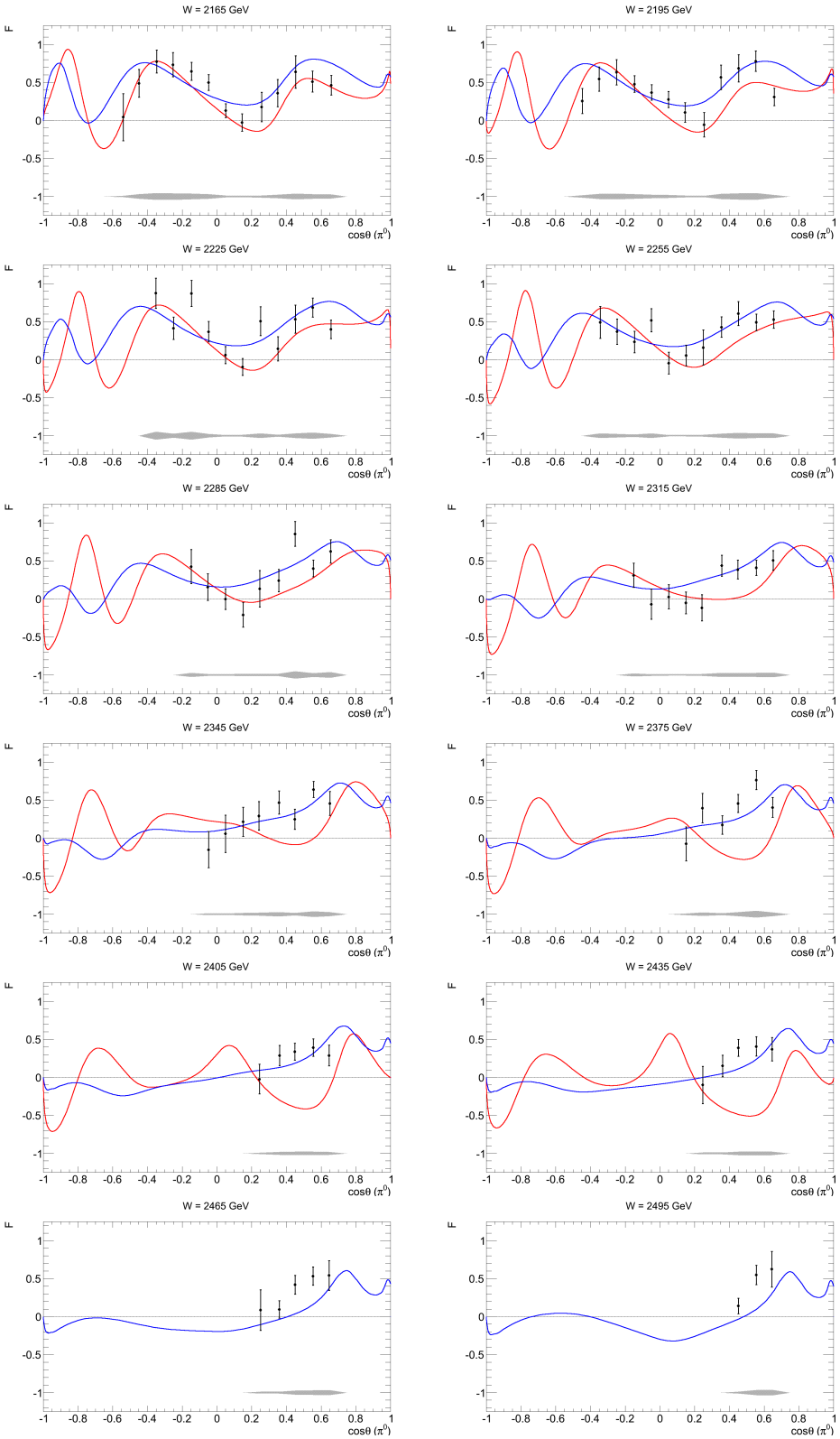

Figure 4.6 Polarization observable F (continued).

Table 4.1 Experimental results for each kinematic bin.

W (GeV)	$\cos\theta_\pi^{cm}$	T	F
1.504	−0.827	$-0.243 \pm 0.031 \pm 0.022$	$0.506 \pm 0.107 \pm 0.031$
1.505	−0.751	$-0.316 \pm 0.019 \pm 0.025$	$0.525 \pm 0.076 \pm 0.032$
1.504	−0.648	$-0.383 \pm 0.016 \pm 0.027$	$0.608 \pm 0.061 \pm 0.036$
1.504	−0.549	$-0.456 \pm 0.016 \pm 0.029$	$0.458 \pm 0.060 \pm 0.028$
1.504	−0.448	$-0.517 \pm 0.015 \pm 0.032$	$0.445 \pm 0.055 \pm 0.027$
1.504	−0.349	$-0.568 \pm 0.013 \pm 0.034$	$0.432 \pm 0.045 \pm 0.027$
1.504	−0.250	$-0.591 \pm 0.012 \pm 0.035$	$0.381 \pm 0.044 \pm 0.024$
1.504	−0.156	$-0.565 \pm 0.015 \pm 0.034$	$0.430 \pm 0.055 \pm 0.026$
1.504	−0.044	$-0.546 \pm 0.013 \pm 0.033$	$0.308 \pm 0.048 \pm 0.020$
1.504	0.049	$-0.559 \pm 0.012 \pm 0.033$	$0.298 \pm 0.043 \pm 0.020$
1.504	0.151	$-0.495 \pm 0.013 \pm 0.031$	$0.240 \pm 0.048 \pm 0.017$
1.504	0.252	$-0.436 \pm 0.012 \pm 0.029$	$0.198 \pm 0.042 \pm 0.015$
1.504	0.345	$-0.385 \pm 0.015 \pm 0.027$	$0.043 \pm 0.058 \pm 0.010$
1.504	0.452	$-0.261 \pm 0.014 \pm 0.023$	$0.086 \pm 0.054 \pm 0.011$
1.504	0.548	$-0.131 \pm 0.016 \pm 0.020$	$-0.039 \pm 0.073 \pm 0.010$
1.535	−0.824	$0.023 \pm 0.030 \pm 0.019$	$0.669 \pm 0.096 \pm 0.039$
1.536	−0.752	$0.020 \pm 0.018 \pm 0.019$	$0.689 \pm 0.064 \pm 0.041$
1.536	−0.647	$-0.048 \pm 0.015 \pm 0.019$	$0.554 \pm 0.054 \pm 0.033$
1.536	−0.554	$-0.148 \pm 0.015 \pm 0.020$	$0.531 \pm 0.055 \pm 0.032$
1.536	−0.448	$-0.212 \pm 0.014 \pm 0.022$	$0.458 \pm 0.051 \pm 0.028$
1.535	−0.349	$-0.243 \pm 0.012 \pm 0.022$	$0.404 \pm 0.044 \pm 0.025$
1.535	−0.249	$-0.289 \pm 0.011 \pm 0.024$	$0.318 \pm 0.040 \pm 0.021$
1.536	−0.157	$-0.318 \pm 0.013 \pm 0.025$	$0.283 \pm 0.049 \pm 0.019$
1.535	−0.043	$-0.327 \pm 0.014 \pm 0.025$	$0.252 \pm 0.052 \pm 0.018$
1.535	0.050	$-0.307 \pm 0.011 \pm 0.024$	$0.180 \pm 0.040 \pm 0.014$
1.535	0.150	$-0.265 \pm 0.013 \pm 0.023$	$0.210 \pm 0.048 \pm 0.016$
1.535	0.252	$-0.224 \pm 0.013 \pm 0.022$	$0.082 \pm 0.043 \pm 0.011$
1.536	0.344	$-0.215 \pm 0.015 \pm 0.022$	$0.040 \pm 0.053 \pm 0.010$
1.535	0.454	$-0.104 \pm 0.013 \pm 0.020$	$0.000 \pm 0.049 \pm 0.010$
1.536	0.549	$0.022 \pm 0.018 \pm 0.019$	$-0.081 \pm 0.079 \pm 0.011$
1.565	−0.822	$0.251 \pm 0.028 \pm 0.023$	$0.630 \pm 0.089 \pm 0.037$
1.565	−0.752	$0.204 \pm 0.018 \pm 0.021$	$0.650 \pm 0.056 \pm 0.038$
1.565	−0.647	$0.164 \pm 0.015 \pm 0.021$	$0.545 \pm 0.053 \pm 0.033$
1.565	−0.556	$0.095 \pm 0.015 \pm 0.020$	$0.458 \pm 0.052 \pm 0.028$
1.565	−0.447	$-0.024 \pm 0.016 \pm 0.019$	$0.409 \pm 0.053 \pm 0.025$
1.565	−0.349	$-0.123 \pm 0.014 \pm 0.020$	$0.339 \pm 0.050 \pm 0.022$
1.565	−0.249	$-0.127 \pm 0.013 \pm 0.020$	$0.251 \pm 0.044 \pm 0.017$
1.565	−0.155	$-0.193 \pm 0.014 \pm 0.021$	$0.118 \pm 0.051 \pm 0.012$
1.565	−0.045	$-0.173 \pm 0.017 \pm 0.021$	$0.191 \pm 0.059 \pm 0.015$

Table 4.2 Experimental results for each kinematic bin (continued).

W (GeV)	$\cos\theta_\pi^{cm}$	T	F
1.564	0.053	$-0.178 \pm 0.012 \pm 0.021$	$0.118 \pm 0.043 \pm 0.012$
1.565	0.148	$-0.193 \pm 0.015 \pm 0.021$	$0.092 \pm 0.055 \pm 0.011$
1.565	0.251	$-0.154 \pm 0.016 \pm 0.020$	$0.011 \pm 0.052 \pm 0.010$
1.565	0.347	$-0.125 \pm 0.017 \pm 0.020$	$0.032 \pm 0.058 \pm 0.010$
1.565	0.455	$-0.006 \pm 0.017 \pm 0.019$	$-0.010 \pm 0.058 \pm 0.010$
1.565	0.549	$0.084 \pm 0.025 \pm 0.019$	$0.011 \pm 0.102 \pm 0.010$
1.596	−0.823	$0.227 \pm 0.031 \pm 0.022$	$0.607 \pm 0.099 \pm 0.036$
1.596	−0.752	$0.196 \pm 0.019 \pm 0.021$	$0.537 \pm 0.055 \pm 0.032$
1.596	−0.649	$0.144 \pm 0.017 \pm 0.020$	$0.524 \pm 0.055 \pm 0.032$
1.596	−0.554	$0.098 \pm 0.018 \pm 0.020$	$0.393 \pm 0.055 \pm 0.025$
1.596	−0.445	$0.046 \pm 0.019 \pm 0.019$	$0.349 \pm 0.058 \pm 0.022$
1.596	−0.348	$-0.027 \pm 0.016 \pm 0.019$	$0.324 \pm 0.055 \pm 0.021$
1.595	−0.249	$-0.073 \pm 0.016 \pm 0.019$	$0.246 \pm 0.052 \pm 0.017$
1.596	−0.154	$-0.140 \pm 0.017 \pm 0.020$	$0.232 \pm 0.059 \pm 0.017$
1.595	−0.049	$-0.115 \pm 0.022 \pm 0.020$	$-0.022 \pm 0.069 \pm 0.010$
1.595	0.054	$-0.153 \pm 0.018 \pm 0.020$	$0.127 \pm 0.058 \pm 0.012$
1.596	0.148	$-0.219 \pm 0.021 \pm 0.022$	$-0.009 \pm 0.069 \pm 0.010$
1.595	0.252	$-0.227 \pm 0.023 \pm 0.022$	$-0.056 \pm 0.069 \pm 0.010$
1.596	0.348	$-0.167 \pm 0.025 \pm 0.021$	$-0.040 \pm 0.078 \pm 0.010$
1.595	0.454	$-0.064 \pm 0.028 \pm 0.019$	$0.109 \pm 0.087 \pm 0.012$
1.596	0.550	$-0.010 \pm 0.041 \pm 0.019$	$0.289 \pm 0.154 \pm 0.019$
1.625	−0.821	$0.239 \pm 0.030 \pm 0.022$	$0.476 \pm 0.091 \pm 0.029$
1.625	−0.750	$0.134 \pm 0.019 \pm 0.020$	$0.408 \pm 0.051 \pm 0.025$
1.625	−0.650	$0.107 \pm 0.017 \pm 0.020$	$0.416 \pm 0.052 \pm 0.026$
1.625	−0.551	$0.030 \pm 0.017 \pm 0.019$	$0.242 \pm 0.049 \pm 0.017$
1.625	−0.446	$-0.012 \pm 0.021 \pm 0.019$	$0.352 \pm 0.058 \pm 0.022$
1.625	−0.349	$-0.047 \pm 0.018 \pm 0.019$	$0.239 \pm 0.056 \pm 0.017$
1.625	−0.250	$-0.117 \pm 0.019 \pm 0.020$	$0.249 \pm 0.054 \pm 0.017$
1.625	−0.153	$-0.140 \pm 0.018 \pm 0.020$	$0.228 \pm 0.058 \pm 0.016$
1.625	−0.053	$-0.197 \pm 0.028 \pm 0.021$	$0.359 \pm 0.086 \pm 0.023$
1.624	0.054	$-0.247 \pm 0.022 \pm 0.023$	$0.096 \pm 0.063 \pm 0.011$
1.624	0.148	$-0.336 \pm 0.024 \pm 0.025$	$0.134 \pm 0.074 \pm 0.013$
1.624	0.252	$-0.353 \pm 0.026 \pm 0.026$	$0.332 \pm 0.076 \pm 0.021$
1.625	0.349	$-0.324 \pm 0.026 \pm 0.025$	$0.210 \pm 0.072 \pm 0.016$
1.624	0.454	$-0.344 \pm 0.034 \pm 0.025$	$0.326 \pm 0.096 \pm 0.021$
1.625	0.551	$-0.179 \pm 0.036 \pm 0.021$	$0.450 \pm 0.122 \pm 0.028$
1.655	−0.821	$0.245 \pm 0.030 \pm 0.022$	$0.496 \pm 0.081 \pm 0.030$
1.655	−0.749	$0.110 \pm 0.017 \pm 0.020$	$0.267 \pm 0.045 \pm 0.018$
1.655	−0.650	$0.038 \pm 0.016 \pm 0.019$	$0.194 \pm 0.044 \pm 0.015$

Table 4.3 Experimental results for each kinematic bin (continued).

W (GeV)	$\cos\theta_\pi^{cm}$	T	F
1.655	−0.549	$-0.032 \pm 0.015 \pm 0.019$	$0.166 \pm 0.041 \pm 0.014$
1.655	−0.451	$-0.051 \pm 0.020 \pm 0.019$	$0.192 \pm 0.051 \pm 0.015$
1.655	−0.350	$-0.089 \pm 0.017 \pm 0.019$	$0.267 \pm 0.048 \pm 0.018$
1.655	−0.250	$-0.094 \pm 0.018 \pm 0.020$	$0.221 \pm 0.049 \pm 0.016$
1.654	−0.152	$-0.187 \pm 0.018 \pm 0.021$	$0.198 \pm 0.054 \pm 0.015$
1.655	−0.057	$-0.270 \pm 0.026 \pm 0.023$	$0.495 \pm 0.077 \pm 0.030$
1.654	0.056	$-0.356 \pm 0.025 \pm 0.026$	$0.413 \pm 0.066 \pm 0.026$
1.655	0.149	$-0.462 \pm 0.022 \pm 0.030$	$0.587 \pm 0.063 \pm 0.035$
1.655	0.253	$-0.466 \pm 0.026 \pm 0.030$	$0.543 \pm 0.069 \pm 0.033$
1.655	0.351	$-0.404 \pm 0.024 \pm 0.027$	$0.538 \pm 0.065 \pm 0.032$
1.655	0.451	$-0.367 \pm 0.029 \pm 0.026$	$0.569 \pm 0.079 \pm 0.034$
1.655	0.551	$-0.210 \pm 0.025 \pm 0.022$	$0.753 \pm 0.082 \pm 0.044$
1.684	−0.821	$0.277 \pm 0.034 \pm 0.023$	$0.195 \pm 0.080 \pm 0.015$
1.684	−0.748	$0.148 \pm 0.018 \pm 0.020$	$0.216 \pm 0.045 \pm 0.016$
1.684	−0.650	$-0.047 \pm 0.017 \pm 0.019$	$0.167 \pm 0.043 \pm 0.014$
1.684	−0.548	$-0.079 \pm 0.016 \pm 0.019$	$0.168 \pm 0.041 \pm 0.014$
1.684	−0.455	$-0.073 \pm 0.021 \pm 0.019$	$0.266 \pm 0.049 \pm 0.018$
1.684	−0.350	$-0.082 \pm 0.019 \pm 0.019$	$0.244 \pm 0.048 \pm 0.017$
1.684	−0.249	$-0.086 \pm 0.019 \pm 0.019$	$0.333 \pm 0.049 \pm 0.021$
1.684	−0.152	$-0.197 \pm 0.020 \pm 0.021$	$0.520 \pm 0.055 \pm 0.031$
1.684	−0.056	$-0.293 \pm 0.026 \pm 0.024$	$0.566 \pm 0.074 \pm 0.034$
1.684	0.057	$-0.392 \pm 0.027 \pm 0.027$	$0.803 \pm 0.069 \pm 0.047$
1.684	0.151	$-0.390 \pm 0.022 \pm 0.027$	$0.599 \pm 0.060 \pm 0.036$
1.684	0.252	$-0.347 \pm 0.022 \pm 0.026$	$0.689 \pm 0.060 \pm 0.041$
1.685	0.353	$-0.279 \pm 0.020 \pm 0.023$	$0.687 \pm 0.052 \pm 0.040$
1.685	0.448	$-0.142 \pm 0.025 \pm 0.020$	$0.744 \pm 0.069 \pm 0.044$
1.685	0.552	$0.021 \pm 0.019 \pm 0.019$	$0.452 \pm 0.056 \pm 0.028$
1.713	−0.818	$0.346 \pm 0.047 \pm 0.025$	$0.467 \pm 0.097 \pm 0.028$
1.714	−0.748	$0.014 \pm 0.024 \pm 0.019$	$0.244 \pm 0.058 \pm 0.017$
1.714	−0.651	$-0.108 \pm 0.023 \pm 0.020$	$0.204 \pm 0.053 \pm 0.015$
1.713	−0.549	$-0.116 \pm 0.020 \pm 0.020$	$0.175 \pm 0.052 \pm 0.014$
1.714	−0.457	$-0.067 \pm 0.025 \pm 0.019$	$0.178 \pm 0.057 \pm 0.014$
1.713	−0.348	$-0.068 \pm 0.024 \pm 0.019$	$0.340 \pm 0.057 \pm 0.022$
1.714	−0.250	$-0.095 \pm 0.025 \pm 0.020$	$0.408 \pm 0.062 \pm 0.025$
1.714	−0.151	$-0.059 \pm 0.024 \pm 0.019$	$0.411 \pm 0.062 \pm 0.025$
1.714	−0.056	$-0.157 \pm 0.029 \pm 0.020$	$0.655 \pm 0.082 \pm 0.039$
1.714	0.058	$-0.202 \pm 0.034 \pm 0.021$	$0.739 \pm 0.081 \pm 0.043$
1.714	0.152	$-0.277 \pm 0.025 \pm 0.023$	$0.726 \pm 0.066 \pm 0.043$
1.714	0.251	$-0.143 \pm 0.024 \pm 0.020$	$0.777 \pm 0.066 \pm 0.045$

Table 4.4 Experimental results for each kinematic bin (continued).

W (GeV)	$\cos\theta_\pi^{cm}$	T	F
1.714	0.355	$-0.032 \pm 0.019 \pm 0.019$	$0.552 \pm 0.048 \pm 0.033$
1.714	0.445	$0.138 \pm 0.024 \pm 0.020$	$0.471 \pm 0.061 \pm 0.029$
1.714	0.553	$0.260 \pm 0.021 \pm 0.023$	$0.342 \pm 0.054 \pm 0.022$
1.744	−0.816	$0.066 \pm 0.065 \pm 0.019$	$0.377 \pm 0.125 \pm 0.024$
1.745	−0.751	$-0.055 \pm 0.032 \pm 0.019$	$0.464 \pm 0.075 \pm 0.028$
1.744	−0.649	$-0.168 \pm 0.030 \pm 0.021$	$0.362 \pm 0.066 \pm 0.023$
1.744	−0.550	$-0.189 \pm 0.029 \pm 0.021$	$0.329 \pm 0.069 \pm 0.021$
1.745	−0.456	$-0.091 \pm 0.033 \pm 0.020$	$0.466 \pm 0.073 \pm 0.028$
1.744	−0.346	$-0.124 \pm 0.034 \pm 0.020$	$0.442 \pm 0.077 \pm 0.027$
1.744	−0.249	$-0.126 \pm 0.034 \pm 0.020$	$0.430 \pm 0.083 \pm 0.026$
1.745	−0.150	$-0.206 \pm 0.036 \pm 0.022$	$0.687 \pm 0.087 \pm 0.040$
1.745	−0.053	$-0.188 \pm 0.036 \pm 0.021$	$0.547 \pm 0.097 \pm 0.033$
1.744	0.056	$-0.293 \pm 0.043 \pm 0.024$	$0.777 \pm 0.099 \pm 0.045$
1.745	0.153	$-0.288 \pm 0.028 \pm 0.024$	$0.614 \pm 0.067 \pm 0.036$
1.745	0.250	$-0.212 \pm 0.029 \pm 0.022$	$0.579 \pm 0.076 \pm 0.035$
1.744	0.354	$0.011 \pm 0.025 \pm 0.019$	$0.564 \pm 0.061 \pm 0.034$
1.745	0.444	$0.157 \pm 0.026 \pm 0.021$	$0.496 \pm 0.065 \pm 0.030$
1.744	0.554	$0.332 \pm 0.027 \pm 0.025$	$0.363 \pm 0.064 \pm 0.023$
1.775	−0.816	$0.132 \pm 0.073 \pm 0.020$	$0.601 \pm 0.137 \pm 0.036$
1.776	−0.752	$-0.057 \pm 0.037 \pm 0.019$	$0.416 \pm 0.081 \pm 0.026$
1.775	−0.649	$-0.203 \pm 0.036 \pm 0.021$	$0.202 \pm 0.074 \pm 0.015$
1.775	−0.551	$-0.156 \pm 0.039 \pm 0.020$	$0.454 \pm 0.092 \pm 0.028$
1.775	−0.454	$-0.075 \pm 0.041 \pm 0.019$	$0.223 \pm 0.086 \pm 0.016$
1.775	−0.345	$-0.012 \pm 0.044 \pm 0.019$	$0.647 \pm 0.095 \pm 0.038$
1.775	−0.250	$-0.073 \pm 0.040 \pm 0.019$	$0.343 \pm 0.094 \pm 0.022$
1.775	−0.150	$-0.285 \pm 0.041 \pm 0.024$	$0.631 \pm 0.095 \pm 0.037$
1.776	−0.053	$-0.380 \pm 0.039 \pm 0.027$	$0.623 \pm 0.098 \pm 0.037$
1.775	0.052	$-0.579 \pm 0.057 \pm 0.034$	$0.497 \pm 0.113 \pm 0.030$
1.775	0.155	$-0.435 \pm 0.040 \pm 0.029$	$0.688 \pm 0.087 \pm 0.040$
1.775	0.248	$-0.309 \pm 0.036 \pm 0.024$	$0.511 \pm 0.086 \pm 0.031$
1.775	0.354	$-0.122 \pm 0.032 \pm 0.020$	$0.507 \pm 0.070 \pm 0.031$
1.775	0.446	$0.155 \pm 0.038 \pm 0.020$	$0.519 \pm 0.089 \pm 0.031$
1.775	0.555	$0.399 \pm 0.041 \pm 0.027$	$0.354 \pm 0.088 \pm 0.023$
1.805	−0.815	$0.224 \pm 0.071 \pm 0.022$	$0.471 \pm 0.128 \pm 0.029$
1.805	−0.753	$-0.012 \pm 0.037 \pm 0.019$	$0.571 \pm 0.076 \pm 0.034$
1.805	−0.648	$-0.265 \pm 0.039 \pm 0.023$	$0.417 \pm 0.076 \pm 0.026$
1.805	−0.551	$-0.187 \pm 0.039 \pm 0.021$	$0.302 \pm 0.085 \pm 0.020$
1.805	−0.452	$-0.054 \pm 0.043 \pm 0.019$	$0.233 \pm 0.086 \pm 0.017$
1.805	−0.345	$0.020 \pm 0.051 \pm 0.019$	$0.674 \pm 0.105 \pm 0.040$

Table 4.5 Experimental results for each kinematic bin (continued).

W (GeV)	$\cos\theta_\pi^{cm}$	T	F
1.805	−0.250	$-0.022 \pm 0.043 \pm 0.019$	$0.447 \pm 0.097 \pm 0.027$
1.805	−0.149	$-0.274 \pm 0.044 \pm 0.023$	$0.793 \pm 0.097 \pm 0.046$
1.805	−0.051	$-0.538 \pm 0.043 \pm 0.032$	$0.669 \pm 0.097 \pm 0.039$
1.806	0.047	$-0.659 \pm 0.058 \pm 0.037$	$0.643 \pm 0.112 \pm 0.038$
1.805	0.155	$-0.712 \pm 0.049 \pm 0.040$	$0.594 \pm 0.091 \pm 0.035$
1.805	0.249	$-0.490 \pm 0.038 \pm 0.031$	$0.613 \pm 0.086 \pm 0.036$
1.805	0.355	$-0.191 \pm 0.042 \pm 0.021$	$0.678 \pm 0.091 \pm 0.040$
1.805	0.447	$0.172 \pm 0.040 \pm 0.021$	$0.568 \pm 0.091 \pm 0.034$
1.805	0.556	$0.485 \pm 0.049 \pm 0.030$	$0.390 \pm 0.096 \pm 0.024$
1.834	−0.813	$0.120 \pm 0.076 \pm 0.020$	$0.311 \pm 0.132 \pm 0.020$
1.835	−0.751	$-0.026 \pm 0.037 \pm 0.019$	$0.376 \pm 0.072 \pm 0.024$
1.835	−0.647	$-0.136 \pm 0.042 \pm 0.020$	$0.247 \pm 0.079 \pm 0.017$
1.835	−0.552	$-0.099 \pm 0.041 \pm 0.020$	$0.356 \pm 0.084 \pm 0.023$
1.835	−0.451	$0.004 \pm 0.045 \pm 0.019$	$0.326 \pm 0.090 \pm 0.021$
1.835	−0.347	$0.161 \pm 0.053 \pm 0.021$	$0.617 \pm 0.102 \pm 0.037$
1.835	−0.251	$-0.028 \pm 0.043 \pm 0.019$	$0.704 \pm 0.096 \pm 0.041$
1.835	−0.149	$-0.209 \pm 0.039 \pm 0.022$	$0.486 \pm 0.080 \pm 0.029$
1.835	−0.050	$-0.435 \pm 0.040 \pm 0.029$	$0.597 \pm 0.089 \pm 0.035$
1.835	0.043	$-0.619 \pm 0.053 \pm 0.036$	$0.536 \pm 0.104 \pm 0.032$
1.834	0.156	$-0.691 \pm 0.046 \pm 0.039$	$0.519 \pm 0.081 \pm 0.031$
1.835	0.249	$-0.640 \pm 0.046 \pm 0.037$	$0.648 \pm 0.092 \pm 0.038$
1.834	0.352	$-0.248 \pm 0.051 \pm 0.023$	$0.724 \pm 0.108 \pm 0.042$
1.834	0.448	$0.256 \pm 0.049 \pm 0.023$	$0.439 \pm 0.102 \pm 0.027$
1.834	0.557	$0.749 \pm 0.076 \pm 0.041$	$0.411 \pm 0.118 \pm 0.025$
1.835	0.653	$0.753 \pm 0.063 \pm 0.042$	$0.123 \pm 0.109 \pm 0.012$
1.865	−0.811	$0.212 \pm 0.081 \pm 0.022$	$0.512 \pm 0.134 \pm 0.031$
1.865	−0.752	$0.058 \pm 0.034 \pm 0.019$	$0.290 \pm 0.061 \pm 0.019$
1.865	−0.646	$-0.175 \pm 0.038 \pm 0.021$	$0.309 \pm 0.072 \pm 0.020$
1.865	−0.551	$-0.087 \pm 0.038 \pm 0.019$	$0.259 \pm 0.072 \pm 0.018$
1.865	−0.450	$0.272 \pm 0.046 \pm 0.023$	$0.632 \pm 0.091 \pm 0.037$
1.865	−0.350	$0.418 \pm 0.048 \pm 0.028$	$0.681 \pm 0.088 \pm 0.040$
1.865	−0.250	$0.145 \pm 0.036 \pm 0.020$	$0.755 \pm 0.076 \pm 0.044$
1.865	−0.147	$-0.082 \pm 0.034 \pm 0.019$	$0.635 \pm 0.072 \pm 0.038$
1.866	−0.051	$-0.368 \pm 0.034 \pm 0.026$	$0.594 \pm 0.072 \pm 0.035$
1.865	0.042	$-0.693 \pm 0.051 \pm 0.039$	$0.432 \pm 0.089 \pm 0.027$
1.865	0.157	$-0.657 \pm 0.051 \pm 0.037$	$0.296 \pm 0.079 \pm 0.020$
1.865	0.249	$-0.626 \pm 0.044 \pm 0.036$	$0.413 \pm 0.079 \pm 0.026$
1.865	0.351	$-0.258 \pm 0.054 \pm 0.023$	$0.328 \pm 0.102 \pm 0.021$
1.865	0.451	$0.304 \pm 0.057 \pm 0.024$	$0.300 \pm 0.105 \pm 0.020$

Table 4.6 Experimental results for each kinematic bin (continued).

W (GeV)	$\cos\theta_\pi^{cm}$	T	F
1.865	0.556	$0.742 \pm 0.075 \pm 0.041$	$0.230 \pm 0.113 \pm 0.017$
1.865	0.653	$0.713 \pm 0.061 \pm 0.040$	$0.073 \pm 0.100 \pm 0.011$
1.894	−0.810	$0.171 \pm 0.088 \pm 0.021$	$0.368 \pm 0.147 \pm 0.023$
1.895	−0.750	$-0.065 \pm 0.038 \pm 0.019$	$0.169 \pm 0.065 \pm 0.014$
1.895	−0.648	$-0.205 \pm 0.044 \pm 0.021$	$0.140 \pm 0.080 \pm 0.013$
1.895	−0.551	$0.134 \pm 0.045 \pm 0.020$	$0.161 \pm 0.080 \pm 0.014$
1.895	−0.450	$0.344 \pm 0.048 \pm 0.025$	$0.472 \pm 0.090 \pm 0.029$
1.895	−0.352	$0.336 \pm 0.048 \pm 0.025$	$0.708 \pm 0.087 \pm 0.042$
1.895	−0.248	$0.242 \pm 0.039 \pm 0.022$	$0.640 \pm 0.076 \pm 0.038$
1.895	−0.148	$-0.014 \pm 0.033 \pm 0.019$	$0.670 \pm 0.068 \pm 0.039$
1.895	−0.050	$-0.252 \pm 0.028 \pm 0.023$	$0.518 \pm 0.061 \pm 0.031$
1.895	0.043	$-0.499 \pm 0.037 \pm 0.031$	$0.293 \pm 0.069 \pm 0.019$
1.894	0.156	$-0.596 \pm 0.057 \pm 0.035$	$0.479 \pm 0.090 \pm 0.029$
1.895	0.248	$-0.508 \pm 0.050 \pm 0.031$	$0.306 \pm 0.087 \pm 0.020$
1.894	0.351	$-0.411 \pm 0.079 \pm 0.028$	$0.515 \pm 0.145 \pm 0.031$
1.895	0.453	$0.415 \pm 0.074 \pm 0.028$	$0.359 \pm 0.126 \pm 0.023$
1.895	0.555	$0.801 \pm 0.096 \pm 0.044$	$0.100 \pm 0.127 \pm 0.012$
1.895	0.654	$0.488 \pm 0.053 \pm 0.031$	$0.163 \pm 0.096 \pm 0.014$
1.924	−0.808	$0.076 \pm 0.103 \pm 0.019$	$0.032 \pm 0.162 \pm 0.010$
1.925	−0.751	$-0.065 \pm 0.039 \pm 0.019$	$0.098 \pm 0.063 \pm 0.011$
1.924	−0.649	$-0.074 \pm 0.047 \pm 0.019$	$0.121 \pm 0.081 \pm 0.012$
1.925	−0.551	$0.039 \pm 0.050 \pm 0.019$	$0.050 \pm 0.082 \pm 0.010$
1.925	−0.449	$0.427 \pm 0.048 \pm 0.028$	$0.448 \pm 0.087 \pm 0.027$
1.925	−0.353	$0.489 \pm 0.058 \pm 0.031$	$0.777 \pm 0.097 \pm 0.045$
1.925	−0.247	$0.342 \pm 0.038 \pm 0.025$	$0.769 \pm 0.071 \pm 0.045$
1.925	−0.148	$0.151 \pm 0.034 \pm 0.020$	$0.659 \pm 0.067 \pm 0.039$
1.925	−0.049	$-0.148 \pm 0.028 \pm 0.020$	$0.395 \pm 0.054 \pm 0.025$
1.925	0.044	$-0.354 \pm 0.037 \pm 0.026$	$0.356 \pm 0.070 \pm 0.023$
1.925	0.154	$-0.428 \pm 0.062 \pm 0.028$	$0.348 \pm 0.094 \pm 0.022$
1.925	0.250	$-0.461 \pm 0.059 \pm 0.030$	$0.198 \pm 0.099 \pm 0.015$
1.925	0.350	$-0.125 \pm 0.084 \pm 0.020$	$0.270 \pm 0.153 \pm 0.018$
1.925	0.454	$0.410 \pm 0.095 \pm 0.028$	$0.052 \pm 0.145 \pm 0.010$
1.924	0.553	$0.713 \pm 0.117 \pm 0.040$	$0.145 \pm 0.163 \pm 0.013$
1.925	0.653	$0.204 \pm 0.045 \pm 0.021$	$-0.028 \pm 0.088 \pm 0.010$
1.953	−0.807	$-0.118 \pm 0.182 \pm 0.020$	$0.862 \pm 0.291 \pm 0.050$
1.954	−0.748	$-0.208 \pm 0.045 \pm 0.022$	$0.076 \pm 0.068 \pm 0.011$
1.954	−0.650	$-0.161 \pm 0.060 \pm 0.021$	$-0.098 \pm 0.102 \pm 0.011$
1.954	−0.550	$0.047 \pm 0.057 \pm 0.019$	$0.295 \pm 0.093 \pm 0.020$
1.955	−0.450	$0.537 \pm 0.059 \pm 0.032$	$0.633 \pm 0.105 \pm 0.037$

Table 4.7 Experimental results for each kinematic bin (continued).

W (GeV)	$\cos\theta_\pi^{cm}$	T	F
1.955	−0.353	$0.549 \pm 0.055 \pm 0.033$	$0.678 \pm 0.085 \pm 0.040$
1.955	−0.245	$0.260 \pm 0.039 \pm 0.023$	$0.628 \pm 0.067 \pm 0.037$
1.955	−0.147	$0.153 \pm 0.036 \pm 0.020$	$0.633 \pm 0.069 \pm 0.037$
1.955	−0.051	$-0.063 \pm 0.032 \pm 0.019$	$0.442 \pm 0.060 \pm 0.027$
1.955	0.045	$-0.251 \pm 0.036 \pm 0.023$	$0.267 \pm 0.067 \pm 0.018$
1.954	0.154	$-0.427 \pm 0.063 \pm 0.028$	$0.122 \pm 0.091 \pm 0.012$
1.954	0.250	$-0.487 \pm 0.065 \pm 0.030$	$0.173 \pm 0.101 \pm 0.014$
1.954	0.348	$-0.120 \pm 0.108 \pm 0.020$	$0.295 \pm 0.189 \pm 0.020$
1.954	0.455	$0.753 \pm 0.151 \pm 0.042$	$0.362 \pm 0.227 \pm 0.023$
1.955	0.550	$0.372 \pm 0.101 \pm 0.026$	$0.314 \pm 0.167 \pm 0.020$
1.955	0.654	$-0.054 \pm 0.059 \pm 0.019$	$-0.247 \pm 0.115 \pm 0.017$
1.984	−0.749	$-0.312 \pm 0.058 \pm 0.024$	$0.050 \pm 0.086 \pm 0.010$
1.984	−0.653	$-0.328 \pm 0.075 \pm 0.025$	$-0.192 \pm 0.118 \pm 0.015$
1.984	−0.549	$0.009 \pm 0.060 \pm 0.019$	$0.051 \pm 0.095 \pm 0.010$
1.984	−0.449	$0.371 \pm 0.057 \pm 0.026$	$0.442 \pm 0.096 \pm 0.027$
1.984	−0.350	$0.573 \pm 0.059 \pm 0.034$	$0.590 \pm 0.089 \pm 0.035$
1.984	−0.244	$0.280 \pm 0.043 \pm 0.023$	$0.658 \pm 0.070 \pm 0.039$
1.984	−0.149	$0.119 \pm 0.034 \pm 0.020$	$0.587 \pm 0.061 \pm 0.035$
1.985	−0.051	$0.007 \pm 0.034 \pm 0.019$	$0.378 \pm 0.059 \pm 0.024$
1.985	0.047	$-0.171 \pm 0.036 \pm 0.021$	$0.268 \pm 0.066 \pm 0.018$
1.984	0.148	$-0.332 \pm 0.071 \pm 0.025$	$0.312 \pm 0.108 \pm 0.020$
1.984	0.251	$-0.194 \pm 0.074 \pm 0.021$	$0.127 \pm 0.114 \pm 0.012$
1.984	0.348	$-0.205 \pm 0.118 \pm 0.021$	$0.055 \pm 0.194 \pm 0.010$
1.984	0.456	$0.425 \pm 0.181 \pm 0.028$	$0.700 \pm 0.282 \pm 0.041$
1.984	0.549	$0.153 \pm 0.126 \pm 0.020$	$0.284 \pm 0.208 \pm 0.019$
1.984	0.655	$-0.293 \pm 0.059 \pm 0.024$	$-0.043 \pm 0.103 \pm 0.010$
2.015	−0.748	$-0.413 \pm 0.080 \pm 0.028$	$0.003 \pm 0.111 \pm 0.010$
2.015	−0.653	$-0.225 \pm 0.098 \pm 0.022$	$-0.223 \pm 0.147 \pm 0.016$
2.015	−0.548	$-0.004 \pm 0.085 \pm 0.019$	$-0.214 \pm 0.123 \pm 0.016$
2.015	−0.450	$0.763 \pm 0.076 \pm 0.042$	$0.582 \pm 0.122 \pm 0.035$
2.015	−0.349	$0.640 \pm 0.067 \pm 0.037$	$0.605 \pm 0.096 \pm 0.036$
2.015	−0.244	$0.420 \pm 0.055 \pm 0.028$	$0.667 \pm 0.085 \pm 0.039$
2.015	−0.150	$0.124 \pm 0.038 \pm 0.020$	$0.598 \pm 0.065 \pm 0.036$
2.015	−0.050	$0.045 \pm 0.037 \pm 0.019$	$0.452 \pm 0.063 \pm 0.028$
2.015	0.047	$-0.129 \pm 0.042 \pm 0.020$	$0.271 \pm 0.073 \pm 0.018$
2.015	0.145	$-0.168 \pm 0.075 \pm 0.021$	$0.145 \pm 0.116 \pm 0.013$
2.015	0.252	$-0.172 \pm 0.083 \pm 0.021$	$0.009 \pm 0.119 \pm 0.010$
2.015	0.348	$0.043 \pm 0.120 \pm 0.019$	$-0.053 \pm 0.198 \pm 0.010$
2.015	0.457	$0.281 \pm 0.203 \pm 0.023$	$0.958 \pm 0.347 \pm 0.056$

Table 4.8 Experimental results for each kinematic bin (continued).

W (GeV)	$\cos\theta_\pi^{cm}$	T	F
2.015	0.548	$-0.162 \pm 0.134 \pm 0.021$	$0.776 \pm 0.242 \pm 0.045$
2.015	0.656	$-0.601 \pm 0.076 \pm 0.035$	$0.037 \pm 0.117 \pm 0.010$
2.045	−0.747	$-0.604 \pm 0.106 \pm 0.035$	$-0.058 \pm 0.144 \pm 0.011$
2.045	−0.653	$-0.349 \pm 0.100 \pm 0.026$	$-0.189 \pm 0.139 \pm 0.015$
2.045	−0.548	$-0.027 \pm 0.100 \pm 0.019$	$0.132 \pm 0.144 \pm 0.013$
2.045	−0.449	$0.624 \pm 0.078 \pm 0.036$	$0.349 \pm 0.117 \pm 0.022$
2.045	−0.348	$0.680 \pm 0.073 \pm 0.038$	$0.775 \pm 0.109 \pm 0.045$
2.045	−0.244	$0.420 \pm 0.061 \pm 0.028$	$0.643 \pm 0.092 \pm 0.038$
2.045	−0.150	$0.138 \pm 0.045 \pm 0.020$	$0.635 \pm 0.074 \pm 0.038$
2.045	−0.050	$0.010 \pm 0.042 \pm 0.019$	$0.518 \pm 0.067 \pm 0.031$
2.045	0.050	$-0.202 \pm 0.047 \pm 0.021$	$0.237 \pm 0.078 \pm 0.017$
2.045	0.142	$-0.216 \pm 0.073 \pm 0.022$	$0.108 \pm 0.112 \pm 0.012$
2.045	0.254	$-0.136 \pm 0.090 \pm 0.020$	$0.046 \pm 0.121 \pm 0.010$
2.046	0.348	$0.593 \pm 0.184 \pm 0.035$	$0.167 \pm 0.277 \pm 0.014$
2.045	0.457	$-0.023 \pm 0.145 \pm 0.019$	$0.433 \pm 0.226 \pm 0.027$
2.046	0.549	$-0.339 \pm 0.111 \pm 0.025$	$0.368 \pm 0.170 \pm 0.023$
2.045	0.656	$-0.550 \pm 0.070 \pm 0.033$	$0.213 \pm 0.105 \pm 0.016$
2.072	−0.742	$-0.608 \pm 0.124 \pm 0.035$	$0.022 \pm 0.147 \pm 0.010$
2.074	−0.653	$-0.385 \pm 0.125 \pm 0.027$	$-0.386 \pm 0.173 \pm 0.024$
2.074	−0.547	$0.158 \pm 0.103 \pm 0.021$	$0.019 \pm 0.146 \pm 0.010$
2.074	−0.449	$0.622 \pm 0.086 \pm 0.036$	$0.687 \pm 0.130 \pm 0.040$
2.074	−0.348	$0.501 \pm 0.076 \pm 0.031$	$0.501 \pm 0.107 \pm 0.030$
2.074	−0.248	$0.343 \pm 0.068 \pm 0.025$	$0.658 \pm 0.098 \pm 0.039$
2.074	−0.149	$0.138 \pm 0.049 \pm 0.020$	$0.576 \pm 0.078 \pm 0.034$
2.074	−0.049	$-0.110 \pm 0.047 \pm 0.020$	$0.443 \pm 0.073 \pm 0.027$
2.074	0.049	$-0.120 \pm 0.050 \pm 0.020$	$0.418 \pm 0.085 \pm 0.026$
2.074	0.140	$-0.114 \pm 0.078 \pm 0.020$	$0.039 \pm 0.117 \pm 0.010$
2.074	0.255	$-0.095 \pm 0.106 \pm 0.020$	$0.160 \pm 0.140 \pm 0.014$
2.074	0.347	$0.613 \pm 0.175 \pm 0.036$	$0.620 \pm 0.272 \pm 0.037$
2.074	0.456	$-0.108 \pm 0.173 \pm 0.020$	$0.759 \pm 0.263 \pm 0.044$
2.074	0.548	$-0.308 \pm 0.130 \pm 0.024$	$0.743 \pm 0.213 \pm 0.044$
2.074	0.657	$-0.787 \pm 0.093 \pm 0.043$	$0.145 \pm 0.121 \pm 0.013$
2.104	−0.649	$-0.604 \pm 0.158 \pm 0.035$	$-0.318 \pm 0.202 \pm 0.021$
2.104	−0.547	$0.089 \pm 0.127 \pm 0.019$	$-0.077 \pm 0.177 \pm 0.011$
2.104	−0.448	$0.457 \pm 0.107 \pm 0.029$	$0.447 \pm 0.150 \pm 0.027$
2.104	−0.348	$0.573 \pm 0.093 \pm 0.034$	$0.855 \pm 0.140 \pm 0.050$
2.104	−0.249	$0.265 \pm 0.080 \pm 0.023$	$0.685 \pm 0.114 \pm 0.040$
2.104	−0.149	$0.177 \pm 0.056 \pm 0.021$	$0.643 \pm 0.084 \pm 0.038$
2.104	−0.049	$-0.213 \pm 0.049 \pm 0.022$	$0.386 \pm 0.071 \pm 0.024$

Table 4.9 Experimental results for each kinematic bin (continued).

W (GeV)	$\cos\theta_\pi^{cm}$	T	F
2.105	0.049	$-0.203 \pm 0.052 \pm 0.021$	$0.212 \pm 0.082 \pm 0.016$
2.105	0.140	$-0.163 \pm 0.074 \pm 0.021$	$-0.021 \pm 0.106 \pm 0.010$
2.104	0.257	$-0.068 \pm 0.140 \pm 0.019$	$0.633 \pm 0.186 \pm 0.037$
2.105	0.349	$0.032 \pm 0.107 \pm 0.019$	$0.394 \pm 0.168 \pm 0.025$
2.105	0.456	$-0.023 \pm 0.159 \pm 0.019$	$1.159 \pm 0.270 \pm 0.067$
2.105	0.549	$-0.542 \pm 0.106 \pm 0.033$	$0.462 \pm 0.149 \pm 0.028$
2.105	0.658	$-0.598 \pm 0.085 \pm 0.035$	$0.164 \pm 0.114 \pm 0.014$
2.134	−0.547	$-0.074 \pm 0.135 \pm 0.019$	$0.155 \pm 0.189 \pm 0.013$
2.134	−0.449	$0.433 \pm 0.123 \pm 0.028$	$0.335 \pm 0.160 \pm 0.022$
2.135	−0.349	$0.460 \pm 0.096 \pm 0.029$	$0.792 \pm 0.142 \pm 0.046$
2.135	−0.251	$0.238 \pm 0.096 \pm 0.022$	$0.591 \pm 0.129 \pm 0.035$
2.135	−0.147	$0.067 \pm 0.071 \pm 0.019$	$0.523 \pm 0.100 \pm 0.031$
2.135	−0.049	$-0.071 \pm 0.055 \pm 0.019$	$0.368 \pm 0.082 \pm 0.023$
2.135	0.049	$-0.244 \pm 0.056 \pm 0.022$	$0.330 \pm 0.085 \pm 0.021$
2.134	0.142	$-0.293 \pm 0.072 \pm 0.024$	$0.143 \pm 0.107 \pm 0.013$
2.134	0.257	$-0.112 \pm 0.116 \pm 0.020$	$0.229 \pm 0.139 \pm 0.016$
2.135	0.350	$0.251 \pm 0.136 \pm 0.023$	$0.398 \pm 0.198 \pm 0.025$
2.135	0.455	$-0.184 \pm 0.177 \pm 0.021$	$1.236 \pm 0.296 \pm 0.071$
2.135	0.551	$-0.690 \pm 0.115 \pm 0.039$	$0.642 \pm 0.155 \pm 0.038$
2.135	0.658	$-0.571 \pm 0.085 \pm 0.034$	$0.268 \pm 0.113 \pm 0.018$
2.165	−0.540	$-0.074 \pm 0.225 \pm 0.019$	$0.044 \pm 0.310 \pm 0.010$
2.165	−0.449	$0.252 \pm 0.135 \pm 0.023$	$0.490 \pm 0.183 \pm 0.030$
2.165	−0.347	$0.391 \pm 0.101 \pm 0.027$	$0.775 \pm 0.151 \pm 0.045$
2.166	−0.253	$0.175 \pm 0.107 \pm 0.021$	$0.735 \pm 0.158 \pm 0.043$
2.165	−0.147	$0.120 \pm 0.084 \pm 0.020$	$0.646 \pm 0.119 \pm 0.038$
2.166	−0.048	$-0.109 \pm 0.070 \pm 0.020$	$0.499 \pm 0.104 \pm 0.030$
2.165	0.051	$-0.251 \pm 0.062 \pm 0.023$	$0.129 \pm 0.091 \pm 0.012$
2.166	0.145	$-0.296 \pm 0.083 \pm 0.024$	$-0.026 \pm 0.115 \pm 0.010$
2.166	0.257	$-0.234 \pm 0.169 \pm 0.022$	$0.178 \pm 0.193 \pm 0.014$
2.166	0.351	$0.086 \pm 0.127 \pm 0.019$	$0.360 \pm 0.180 \pm 0.023$
2.166	0.454	$0.091 \pm 0.149 \pm 0.020$	$0.638 \pm 0.213 \pm 0.038$
2.166	0.551	$-0.563 \pm 0.105 \pm 0.033$	$0.512 \pm 0.139 \pm 0.031$
2.165	0.658	$-0.707 \pm 0.101 \pm 0.040$	$0.463 \pm 0.130 \pm 0.028$
2.195	−0.447	$0.027 \pm 0.134 \pm 0.019$	$0.256 \pm 0.164 \pm 0.018$
2.195	−0.350	$0.297 \pm 0.106 \pm 0.024$	$0.545 \pm 0.159 \pm 0.033$
2.195	−0.250	$0.121 \pm 0.106 \pm 0.020$	$0.635 \pm 0.166 \pm 0.038$
2.195	−0.146	$0.195 \pm 0.085 \pm 0.021$	$0.480 \pm 0.109 \pm 0.029$
2.195	−0.048	$-0.114 \pm 0.072 \pm 0.020$	$0.368 \pm 0.102 \pm 0.023$
2.195	0.049	$-0.280 \pm 0.073 \pm 0.023$	$0.276 \pm 0.105 \pm 0.019$

Table 4.10 Experimental results for each kinematic bin (continued).

W (GeV)	$\cos\theta_\pi^{cm}$	T	F
2.196	0.146	$-0.491 \pm 0.091 \pm 0.031$	$0.106 \pm 0.128 \pm 0.012$
2.195	0.254	$-0.360 \pm 0.150 \pm 0.026$	$-0.055 \pm 0.160 \pm 0.010$
2.195	0.351	$0.272 \pm 0.117 \pm 0.023$	$0.569 \pm 0.162 \pm 0.034$
2.196	0.453	$-0.103 \pm 0.127 \pm 0.020$	$0.687 \pm 0.180 \pm 0.040$
2.195	0.553	$-0.665 \pm 0.100 \pm 0.038$	$0.781 \pm 0.134 \pm 0.046$
2.195	0.658	$-0.691 \pm 0.093 \pm 0.039$	$0.311 \pm 0.115 \pm 0.020$
2.225	−0.352	$0.190 \pm 0.120 \pm 0.021$	$0.875 \pm 0.200 \pm 0.051$
2.225	−0.250	$0.313 \pm 0.114 \pm 0.024$	$0.414 \pm 0.146 \pm 0.026$
2.225	−0.146	$-0.065 \pm 0.118 \pm 0.019$	$0.871 \pm 0.172 \pm 0.051$
2.225	−0.048	$-0.134 \pm 0.096 \pm 0.020$	$0.369 \pm 0.134 \pm 0.023$
2.225	0.049	$-0.302 \pm 0.084 \pm 0.024$	$0.061 \pm 0.113 \pm 0.011$
2.225	0.147	$-0.182 \pm 0.081 \pm 0.021$	$-0.094 \pm 0.111 \pm 0.011$
2.225	0.252	$0.205 \pm 0.152 \pm 0.021$	$0.507 \pm 0.189 \pm 0.031$
2.225	0.352	$0.144 \pm 0.128 \pm 0.020$	$0.144 \pm 0.159 \pm 0.013$
2.225	0.452	$0.123 \pm 0.135 \pm 0.020$	$0.534 \pm 0.185 \pm 0.032$
2.225	0.552	$-0.559 \pm 0.099 \pm 0.033$	$0.687 \pm 0.126 \pm 0.040$
2.225	0.657	$-0.471 \pm 0.095 \pm 0.030$	$0.400 \pm 0.121 \pm 0.025$
2.255	−0.344	$0.289 \pm 0.152 \pm 0.024$	$0.491 \pm 0.209 \pm 0.030$
2.255	−0.247	$0.094 \pm 0.131 \pm 0.020$	$0.369 \pm 0.168 \pm 0.023$
2.255	−0.146	$0.128 \pm 0.118 \pm 0.020$	$0.234 \pm 0.142 \pm 0.017$
2.255	−0.049	$-0.355 \pm 0.118 \pm 0.026$	$0.519 \pm 0.152 \pm 0.031$
2.255	0.051	$-0.269 \pm 0.109 \pm 0.023$	$-0.045 \pm 0.143 \pm 0.010$
2.255	0.151	$-0.282 \pm 0.107 \pm 0.023$	$0.055 \pm 0.137 \pm 0.010$
2.256	0.250	$0.056 \pm 0.196 \pm 0.019$	$0.161 \pm 0.232 \pm 0.014$
2.256	0.355	$0.245 \pm 0.104 \pm 0.022$	$0.429 \pm 0.134 \pm 0.026$
2.256	0.452	$-0.006 \pm 0.117 \pm 0.019$	$0.608 \pm 0.158 \pm 0.036$
2.256	0.555	$-0.451 \pm 0.087 \pm 0.029$	$0.492 \pm 0.109 \pm 0.030$
2.255	0.656	$-0.594 \pm 0.089 \pm 0.035$	$0.529 \pm 0.113 \pm 0.032$
2.284	−0.149	$0.175 \pm 0.170 \pm 0.021$	$0.426 \pm 0.224 \pm 0.026$
2.285	−0.052	$-0.168 \pm 0.144 \pm 0.021$	$0.157 \pm 0.177 \pm 0.013$
2.284	0.049	$-0.142 \pm 0.110 \pm 0.020$	$-0.003 \pm 0.136 \pm 0.010$
2.284	0.151	$-0.043 \pm 0.120 \pm 0.019$	$-0.209 \pm 0.162 \pm 0.016$
2.285	0.246	$0.312 \pm 0.213 \pm 0.024$	$0.136 \pm 0.240 \pm 0.013$
2.284	0.357	$0.305 \pm 0.134 \pm 0.024$	$0.242 \pm 0.147 \pm 0.017$
2.285	0.450	$-0.078 \pm 0.113 \pm 0.019$	$0.856 \pm 0.162 \pm 0.050$
2.284	0.556	$-0.368 \pm 0.091 \pm 0.026$	$0.401 \pm 0.108 \pm 0.025$
2.285	0.655	$-0.719 \pm 0.126 \pm 0.040$	$0.624 \pm 0.154 \pm 0.037$
2.315	−0.151	$0.127 \pm 0.120 \pm 0.020$	$0.311 \pm 0.159 \pm 0.020$
2.314	−0.049	$-0.379 \pm 0.164 \pm 0.027$	$-0.070 \pm 0.199 \pm 0.011$

Table 4.11 Experimental results for each kinematic bin (continued).

W (GeV)	$\cos\theta_\pi^{cm}$	T	F
2.315	0.051	$-0.375 \pm 0.133 \pm 0.026$	$0.029 \pm 0.161 \pm 0.010$
2.315	0.149	$-0.118 \pm 0.105 \pm 0.020$	$-0.051 \pm 0.144 \pm 0.010$
2.315	0.242	$0.218 \pm 0.148 \pm 0.022$	$-0.116 \pm 0.170 \pm 0.012$
2.315	0.357	$0.065 \pm 0.123 \pm 0.019$	$0.438 \pm 0.137 \pm 0.027$
2.315	0.449	$-0.202 \pm 0.098 \pm 0.021$	$0.386 \pm 0.123 \pm 0.024$
2.315	0.555	$-0.524 \pm 0.090 \pm 0.032$	$0.411 \pm 0.102 \pm 0.025$
2.315	0.652	$-0.741 \pm 0.113 \pm 0.041$	$0.506 \pm 0.129 \pm 0.031$
2.344	−0.047	$-0.232 \pm 0.218 \pm 0.022$	$-0.151 \pm 0.239 \pm 0.013$
2.344	0.050	$-0.389 \pm 0.205 \pm 0.027$	$0.059 \pm 0.245 \pm 0.011$
2.344	0.151	$0.082 \pm 0.151 \pm 0.019$	$0.217 \pm 0.192 \pm 0.016$
2.345	0.242	$0.256 \pm 0.158 \pm 0.023$	$0.293 \pm 0.188 \pm 0.019$
2.345	0.358	$0.256 \pm 0.138 \pm 0.023$	$0.469 \pm 0.153 \pm 0.029$
2.345	0.449	$-0.020 \pm 0.106 \pm 0.019$	$0.250 \pm 0.133 \pm 0.017$
2.344	0.556	$-0.504 \pm 0.091 \pm 0.031$	$0.641 \pm 0.106 \pm 0.038$
2.345	0.651	$-0.515 \pm 0.136 \pm 0.032$	$0.456 \pm 0.158 \pm 0.028$
2.374	0.152	$0.047 \pm 0.176 \pm 0.019$	$-0.075 \pm 0.223 \pm 0.011$
2.374	0.245	$0.329 \pm 0.158 \pm 0.025$	$0.397 \pm 0.193 \pm 0.025$
2.374	0.360	$0.369 \pm 0.119 \pm 0.026$	$0.173 \pm 0.122 \pm 0.014$
2.374	0.450	$-0.074 \pm 0.091 \pm 0.019$	$0.457 \pm 0.119 \pm 0.028$
2.374	0.555	$-0.282 \pm 0.101 \pm 0.023$	$0.765 \pm 0.126 \pm 0.045$
2.374	0.649	$-0.465 \pm 0.111 \pm 0.030$	$0.405 \pm 0.131 \pm 0.025$
2.405	0.246	$0.315 \pm 0.169 \pm 0.024$	$-0.022 \pm 0.196 \pm 0.010$
2.405	0.362	$0.378 \pm 0.141 \pm 0.027$	$0.289 \pm 0.134 \pm 0.019$
2.406	0.449	$0.051 \pm 0.089 \pm 0.019$	$0.339 \pm 0.111 \pm 0.022$
2.405	0.556	$-0.380 \pm 0.102 \pm 0.027$	$0.391 \pm 0.115 \pm 0.024$
2.405	0.647	$-0.838 \pm 0.132 \pm 0.045$	$0.289 \pm 0.138 \pm 0.019$
2.435	0.246	$0.312 \pm 0.212 \pm 0.024$	$-0.100 \pm 0.245 \pm 0.012$
2.434	0.361	$0.200 \pm 0.149 \pm 0.021$	$0.151 \pm 0.142 \pm 0.013$
2.434	0.451	$-0.054 \pm 0.092 \pm 0.019$	$0.390 \pm 0.111 \pm 0.024$
2.435	0.555	$-0.271 \pm 0.112 \pm 0.023$	$0.408 \pm 0.126 \pm 0.025$
2.435	0.646	$-0.312 \pm 0.130 \pm 0.024$	$0.371 \pm 0.153 \pm 0.023$
2.465	0.251	$0.416 \pm 0.237 \pm 0.028$	$0.086 \pm 0.267 \pm 0.011$
2.465	0.360	$0.210 \pm 0.119 \pm 0.022$	$0.095 \pm 0.113 \pm 0.011$
2.465	0.450	$-0.169 \pm 0.103 \pm 0.021$	$0.421 \pm 0.123 \pm 0.026$
2.465	0.554	$-0.354 \pm 0.105 \pm 0.026$	$0.533 \pm 0.120 \pm 0.032$
2.465	0.646	$-0.838 \pm 0.182 \pm 0.045$	$0.542 \pm 0.196 \pm 0.032$
2.495	0.452	$0.053 \pm 0.089 \pm 0.019$	$0.141 \pm 0.102 \pm 0.013$
2.496	0.555	$-0.186 \pm 0.107 \pm 0.021$	$0.549 \pm 0.128 \pm 0.033$
2.496	0.645	$-0.639 \pm 0.204 \pm 0.037$	$0.624 \pm 0.235 \pm 0.037$

4.2 Outlook

Partial-wave analyses of the present results have been started. Recently, the SAID group made some preliminary fits to the present new data [52]. Figure. 4.7 shows the new F and T data in light blue. The upper two panels show the observables F and T for a photon energy of $E_\gamma = 1695$ MeV and the lower two panels show the results for 2313 MeV. The data are compared with SAID fits to all previous data (red dashed curve) and with new SAID fits that include the present data (green solid curve). The new fits clearly improve the description of the data, especially at the highest energy. The new SAID result seems to mainly be from a fine-tuning of the existing waves. The data mostly helped constrain small multipoles. No new resonances are allowed in the SAID results.

Previous results from the dynamical coupled-channel approach of the Jülich-Bonn group are shown in Fig. 4.8 for the polarization observable F [53]. The present results are shown as open circles and have not yet been included in these model predictions. The blue curves are based on results from Ref. [54] that included new polarization data in $\pi^0 p$ from ELSA. The red and cyan curves show results that additionally include $K^+\Lambda$ photoproduction data. The red curves show results that does include a $N(1900)3/2^+$ resonance; the cyan results do not include that resonance. The results with a $N(1900)3/2^+$ resonance describe the present CLAS data slightly better than those without.

In addition to the comparison with the existing fits, Deborah Rönchen also made new fits [53] for the results of this analysis. The difference between the new fits (blue) which the results of this analysis are included and the old fits (red) which the results of this analysis are not included is significantly large for the W above 2100 MeV as shown in Fig. 4.9.

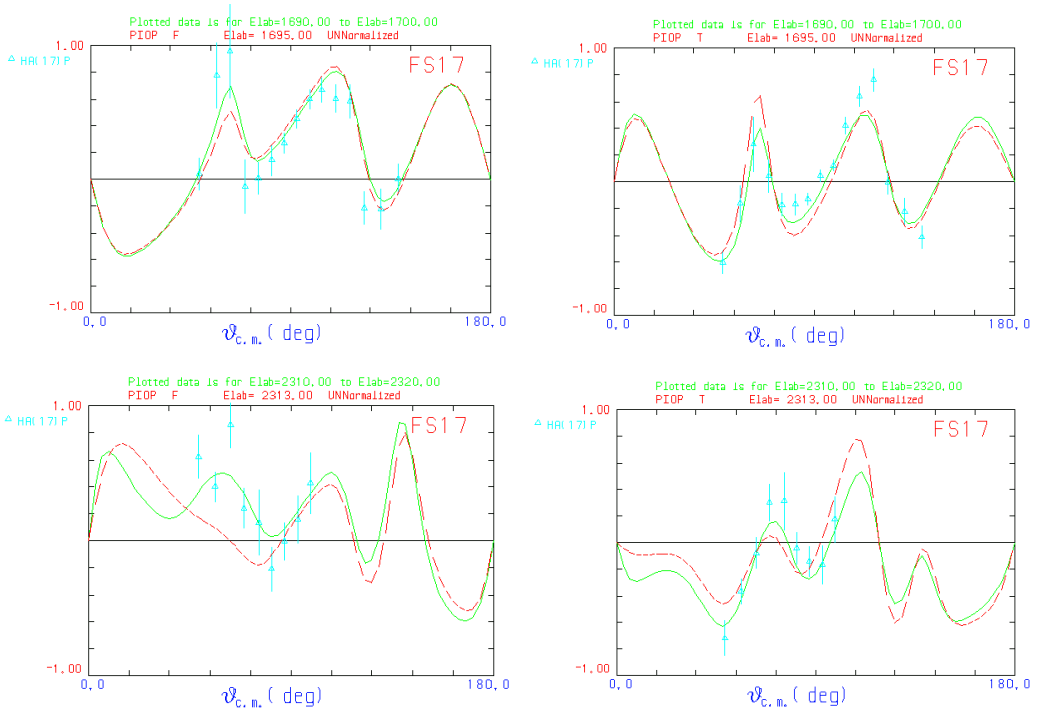

Figure 4.7 Examples of the preliminary fits made by SAID [52]. The red curves are predictions from a comparison to all previous data and the green curves are from the comparison including the new F and T points which are displayed in light blue.

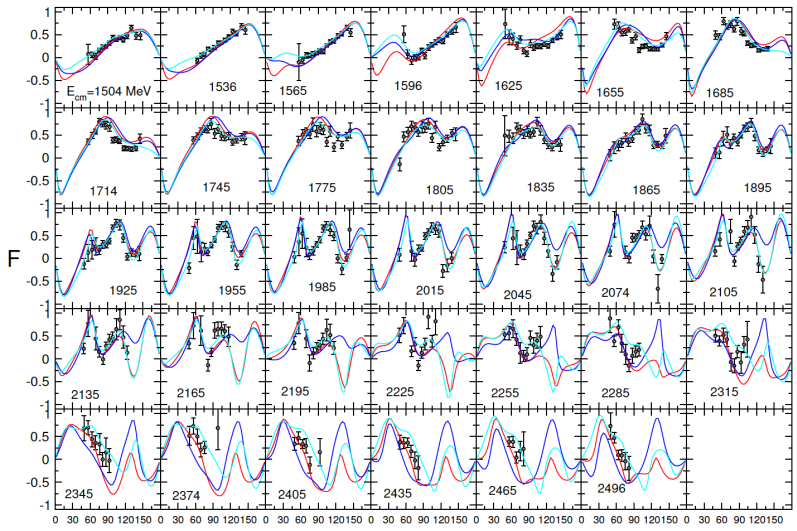

Figure 4.8 Present data of the observable F compared to previous results from the dynamical coupled-channel approach of the Jülich-Bonn group [53]. The blue curves are based on results from Ref. [54], the red and cyan curves show newer results with (red) or without (cyan) a $N(1900)3/2^+$ resonance.

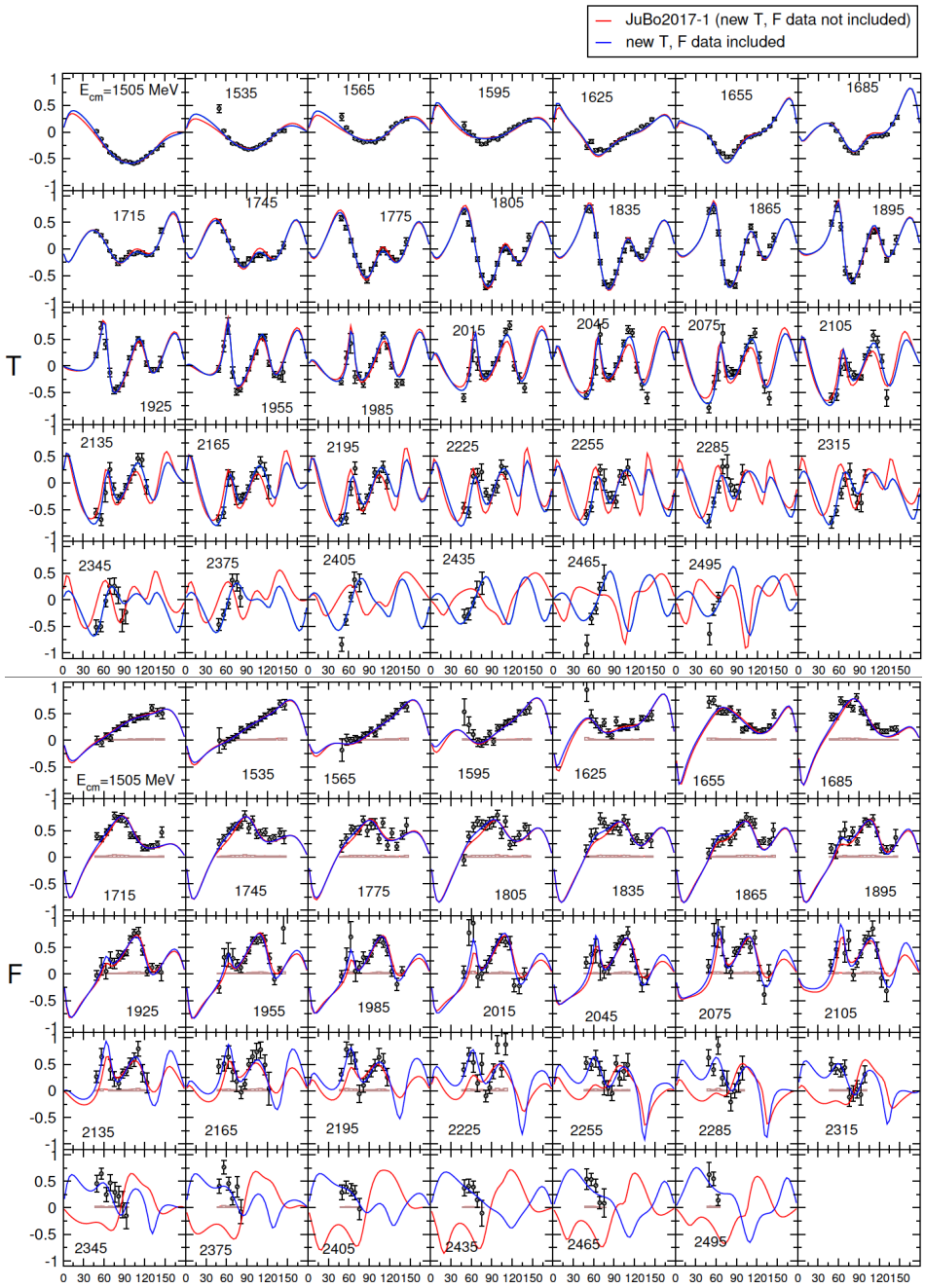

Figure 4.9 New fits for the results of this analysis from Deborah Rönchen [53]. The new fits which the results of this analysis are included are drawn in blue and the old fits which the results of this analysis are not included are drawn in red.

The present SAID, BnGa, and MAID model predictions generally agree with the data in the energy range that overlaps with previous measurements but also show marked differences in the range of W above 2100 MeV. The results at low W agree with the existing results. For the rest of the data where no existing data has currently seen published, partial-wave analyses are still needed. The partial-wave analyses from other groups are still in-progress and are expected to be done soon.

Although the expection of this analysis which is to constrain the partial-wave analyses and also improved the completeness of the data from the pion-photoproduction experiments has been met, there are still a lot to be done beyond the scope of this analysis. The data of higher energies is still needed to extend or verify the existing baryon spectrum. Different observables are also needed since the complex amplitudes that determine the pion-photoproduction reaction require eight observables to make a complete partial-wave analysis but the existing data consists mainly unpolarized cross section and single-polarization observables. Thus, the data of different observables, especially in the energy range that was not included in previous measurement, becomes useful for the partial-wave analysis to fulfill the completeness in the determination of the pion-photoproduction reaction. The future data will constrain further partial-wave analyses and improve the extraction of proton resonance properties as polarization observables provide important constraints to reveal the dynamics and relevant degrees-of-freedom within hadrons.

Chapter 5

Conclusion

The study of the excited baryon resonances reveals the strong interaction in the domain of quark confinement and provides complementary information on the structure of the nucleon. Polarization observables are sensitive to small amplitudes and phase differences and provide important constraints to reveal the dynamics and relevant degrees-of-freedom within hadrons. Double-polarization observables with a polarized target are needed as they carry additional information about the complex amplitudes which does not exist in the unpolarized cross section and single-polarization observables.

Polarization observables T and F in the $\gamma p \to \pi^0 p$ reaction have been extracted for the center-of-mass energy from 1.5 to 2.5 GeV in the FROST experiment with the CLAS detector at JLab. The results of observables T and F in this analysis agree with previous measurements in the overlapping energy range but have a much larger coverage at higher energies. The present SAID, BnGa, MAID, and JüBo model predictions generally agree with the data in the energy range where previous measurements exist but significant deviations are observed in higher energies. The data of double-polarization observables, especially in the energy range that was not included in previous measurement, becomes useful for the partial-wave analysis to fulfill the completeness in the determination of the pion-photoproduction reaction and study the pion photoproduction of this reaction channel in a much larger energy range. The data will constrain further partial-wave analyses and improve the extraction of proton-resonance properties as polarization observables provide important constraints

to reveal the dynamics and relevant degrees-of-freedom within hadrons.

Bibliography

[1] C. Patrignani *et al.*, "Review of particle physics," *Chin. Phys. C*, vol. 40, p. 10001, 2016.

[2] K. T. Mahanthappa and E. C. G. Sudarshan, "SU(6)⊗O(3) structure of strongly interacting particles," *Phys. Rev. Lett.*, vol. 14, pp. 163–166, Feb 1965.

[3] V. Crede and W. Roberts, "Progress toward understanding baryon resonances," *Rept. Prog. Phys.*, vol. 76, p. 076301, 2013.

[4] B. Krusche and S. Schadmand, "Study of Non-Strange Baryon Resonances with Meson Photoproduction," *Prog.Part.Nucl.Phys.*, vol. 51, pp. 399–485, 2003.

[5] M. Gell-Mann, "A schematic model of baryons and mesons," *Physics Letters*, vol. 8, no. 3, pp. 214 – 215, 1964.

[6] N. Isgur and G. Karl, "P-wave baryons in the quark model," *Phys. Rev. D*, vol. 18, pp. 4187–4205, Dec 1978.

[7] N. Isgur and J. Paton, "Flux-tube model for hadrons in QCD," *Phys. Rev. D*, vol. 31, pp. 2910–2929, Jun 1985.

[8] S. Capstick and W. Roberts, "Quark models of baryon masses and decays," *Prog.Part.Nucl.Phys.*, vol. 45, pp. S241 – S331, 2000.

[9] D. B. Lichtenberg, L. J. Tassie, and P. J. Keleman, "Quark-diquark model of baryons and SU(6)," *Phys. Rev.*, vol. 167, pp. 1535–1542, Mar 1968.

[10] Z. Fodor and C. Hoelbling, "Light hadron masses from lattice QCD," *Rev. Mod. Phys.*, vol. 84, pp. 449–495, Apr 2012.

[11] F. Lee, S. Dong, T. Draper, I. Horvath, K. Liu, N. Mathur, and J. Zhang, "Excited baryons from bayesian priors and overlap fermions," *Nucl.Phys.Proc.Suppl.*, vol. 119, pp. 296 – 298, 2003.

[12] S. Durr *et al.*, "Ab-initio determination of light hadron masses," *Science*, vol. 322, pp. 1224 – 1227, 2008.

[13] R. G. Edwards *et al.*, "Excited state baryon spectroscopy from lattice QCD," *Physics Letters D*, vol. 84, p. 074508, 2011.

[14] U. Löring, B. Metsch, and H. Petry, "The light-baryon spectrum in a relativistic quark model with instanton-induced quark forces," *Eur. Phys. J.*, vol. A10, p. 395, 2001.

[15] A. V. Anisovich, V. Burkert, J. Hartmann, E. Klempt, V. A. Nikonov, E. Pasyuk, A. V. Sarantsev, S. Strauch, and U. Thoma, "Evidence for $\Delta(2200)7/2^-$ from photoproduction and consequence for chiral-symmetry restoration at high mass," *Phys. Lett.*, vol. B766, pp. 357–361, 2017.

[16] S. Strauch *et al.*, "First measurement of the polarization observable E in the $\vec{p}(\vec{\gamma},\pi^+)n$ reaction up to 2.25 GeV," *Physics Letters B*, vol. 750, pp. 53 – 58, 2015.

[17] N. Walford, "The Search for Missing Resonances in $\gamma p \to K^+ + \Lambda$ and $K^+ + \Sigma^0$ Using Circularly Polarized Photons on a Transversely Polarized Frozen Spin Target." 2014.

[18] I. S. Barker, A. Donnachie, and J. K. Storrow, "Complete Experiments in Pseudoscalar Photoproduction," *Nucl. Phys.*, vol. B95, p. 347, 1975.

[19] M. Fukushima *et al.*, "Measurement of polarized target asymmetry on $\gamma p \to \pi^0 p$ below 1 GeV," *Nucl. Phys. B*, vol. 136, p. 189, 1978.

[20] P. Feller *et al.*, "The measurement of polarized target asymmetry in $\gamma p \to \pi^0 p$ between 0.4 and 1.0 GeV around 100 deg," *Nucl. Phys. B*, vol. 110, p. 397, 1976.

[21] P. Bussey *et al.*, "Polarisation parameters in neutral pion photoproduction," *Nucl. Phys. B*, vol. 154, p. 492, 1979.

[22] P. Booth *et al.*, "Polarized Target Asymmetry in pi0 Photoproduction Between 0.4-GeV and 1.0-GeV Around 100-Degrees," *Nucl. Phys. B*, vol. 121, p. 45, 1977.

[23] D. Besset, B. Favier, L. Greeniaus, R. Hess, C. Lechanoine, D. Rapin, and D. Werren, "A set of efficient estimators for polarization measurements," *Nuclear Instruments and Methods*, vol. 166, no. 3, pp. 515 – 520, 1979.

[24] J. Hartmann *et al.*, "The N(1520) 3/2- helicity amplitudes from an energy-independent multipole analysis based on new polarization data on photoproduction of neutral pions," *Phys. Rev. Lett.*, vol. 113, p. 062001, 2014.

[25] J. R. M. Annand *et al.*, "T and F asymmetries in π^0 photoproduction on the proton," *Phys. Rev. C*, vol. 93, p. 055209, May 2016.

[26] P. T. Mattione *et al.*, "Differential Cross Section Measurements for γn $\rightarrow \pi^-$p Above the First Nucleon Resonance Region." 2017.

[27] A. V. Anisovich, A. Sarantsev, O. Bartholomy, E. Klempt, V. A. Nikonov, and U. Thoma, "Photoproduction of baryons decaying into nπ and nη," *The European Physical Journal A - Hadrons and Nuclei*, vol. 25, no. 3, pp. 427–439, 2005.

[28] D. Drechsel, S. S. Kamalov, and L. Tiator, "Unitary isobar model –MAID2007," *Eur. Phys. J.*, vol. A34, pp. 69–97, 2007.

[29] D. Rönchen, M. Döring, H. Haberzettl, J. Haidenbauer, U. G. Meißner, and K. Nakayama, "Eta photoproduction in a combined analysis of pion- and photon-induced reactions," *Eur. Phys. J.*, vol. A51, no. 6, p. 70, 2015.

[30] Jefferson Lab Experiment E03-105, "Pion Photoproduction from a Polarized Target", N. Benmouna, W. Briscoe, G. O'Rielly, I. Strakovsky, S. Strauch, spokespersons.

[31] C. W. Leemann, D. R. Douglas, and G. A. Krafft, "The Continuous Electron Beam Accelerator Facility: CEBAF at the Jefferson Laboratory," *Annual Review of Nuclear and Particle Science*, vol. 51, p. 413, 2001.

[32] "About Jefferson Lab." www.jlab.org/about-jefferson-lab, Jul 2017.

[33] V. D. Burkert, "The JLab 12GeV Upgrade and the Initial Science Program," *Proc.Int.Sch.Phys.Fermi*, vol. 180, pp. 303 – 332, 2012.

[34] D. Sober *et al.*, "The bremsstrahlung tagged photon beam in Hall B at JLab," *Nucl. Instrum. Meth. A*, vol. 440, pp. 263–284, 2000.

[35] C. Keith, J. Brock, C. Carlin, S. Comer, D. Kashy, J. McAndrew, D. Meekins, E. Pasyuk, J. Pierce, and M. Seely, "The Jefferson Lab frozen spin target," *Nucl. Instrum. Meth. A*, vol. 684, no. 0, pp. 27 – 35, 2012.

[36] B. A. Mecking *et al.*, "The CEBAF Large Acceptance Spectrometer (CLAS)," *Nucl. Instrum. Meth.*, vol. A503, pp. 513–553, 2003.

[37] W. Gohn *et al.*, "Beam-spin asymmetries from semi-inclusive pion electroproduction," *Phys. Rev. D*, vol. 89, p. 072011, Apr 2014.

[38] J. O'Meara *et al.*, "A Superconducting Toroidal Magnet for the CEBAF Large Acceptance Spectrometer," *IEEE Trans. Mag.*, vol. 25, p. 1902, 1989.

[39] M. Mestayer, D. Carman, B. Asavapibhop, F. Barbosa, P. Bonneau, *et al.*, "The CLAS drift chamber system," *Nucl.Instrum.Meth.*, vol. A449, pp. 81–111, 2000.

[40] E. Smith, T. Carstens, J. Distelbrink, M. Eckhause, H. Egiian, *et al.*, "The time-of-flight system for CLAS," *Nucl.Instrum.Meth.*, vol. A432, pp. 265–298, 1999.

[41] Y. Sharabian *et al.*, "A new highly segmented start counter for the CLAS detector," *Nucl. Instrum. Meth.*, vol. A556, pp. 246–258, 2006.

[42] H. Olsen and L. C. Maximon, "Photon and Electron Polarization in High-Energy Bremsstrahlung and Pair Production with Screening," *Phys. Rev.*, vol. 114, pp. 887–904, 1959.

[43] "Circular Beam Polarization." clasweb.jlab.org/rungroups/g9/wiki/index.php/-Circular_Beam_Polarization, Jul 2017.

[44] Jefferson Lab Experiment E05-008, "The QWeak Experiment: A Search for Physics at the TeV Scale via a Measurement of the Proton's Weak Charge", R.D. Carlini, D. Bowman, M. Finn, S. Page, S. Kowalski, spokespersons.

[45] Y. Mao, "Determination of the target polarization for g9b from NMR measurements." www.jlab.org/Hall-B/secure/g9/yuqing/CLAS_note.pdf.

[46] "G9b pass1v1 cooked files." clasweb.jlab.org/rungroups/g9/wiki/index.php/G9-b_pass1v1_cooked_files, Jul 2017.

[47] E. Pasyuk, "Energy-loss corrections for charged particles in CLAS." CLAS-NOTE 2007–16.

[48] S. Strauch, "Polarization Observable E in the $\vec{p}(\vec{\gamma},\pi^+)n$ Reaction." CLAS-ANALYSIS 2014–101.

[49] M. Dugger, P. Roy, and N. Walford, "Momentum corrections for π^+ and protons in g9b data." CLAS-ANALYSIS 2013–011.

[50] J. W. Fowler, "Maximum-likelihood fits to histograms for improved parameter estimation," 2013.

[51] F. James and M. Winkler, "Minuit 2, CERN.".

[52] R. Workman, "private communication." 2017.

[53] D. Rönchen, "private communication." 2016.

[54] A. V. Anisovich *et al.*, "The impact of new polarization data from Bonn, Mainz and Jefferson Laboratory on $\gamma p \to \pi N$ multipoles," *Eur. Phys. J.*, vol. A52, no. 9, p. 284, 2016.